

Halide Scintillators

Cover: photograph of a 1" $\text{LaCl}_3:\text{Ce}^{3+}$ scintillation detector by Saint-Gobain Crystals and Detectors - France



The research described in this thesis was performed at the Radiation Technology Group of the interfaculty Reactor Institute, Delft University of Technology, Mekelweg 15, 2629JB Delft

This research was financially supported by the Dutch Technology Foundation (STW)

Halide Scintillators

PROEFSCHRIFT

ter verkrijging van de graad van doctor
aan de Technische Universiteit Delft
op gezag van de Rector Magnificus prof. dr. ir. J.T. Fokkema,
voorzitter van het College voor Promoties,
in het openbaar te verdedigen

op vrijdag 6 juni 2003 om 13.30 uur

door

EDGAR VALENTIJN DIEUWER VAN LOEF

doctorandus in de scheikunde,
geboren te Tiel

Dit proefschrift is goedgekeurd door de promotor:
Prof. dr. ir. C.W.E. van Eijk
Toegevoegd promotor: Dr. P. Dorenbos

Samenstelling promotiecommissie:

Rector Magnificus,	voorzitter
Prof. dr. ir. C.W.E. van Eijk,	Technische Universiteit Delft, promotor
Dr. P. Dorenbos,	Technische Universiteit Delft, toegevoegd promotor
Prof. dr. J.J. van Loef	Technische Universiteit Delft
Prof. dr. A. van Veen	Rijksuniversiteit Groningen
Prof. dr. A. Meijerink	Universiteit Utrecht
Prof. dr. J. Schoonman	Technische Universiteit Delft
Dr. J.D. Valentine	Lawrence Livermore National Laboratory, U.S.A.

Published and distributed by: DUP Science

DUP Science is an imprint of
Delft University Press
P.O. Box 98
2600 MG Delft
The Netherlands
Telephone: +31 15 2785678
Fax: +31 15 2781661
E-mail: info@Library.TUdelft.NL

ISBN 90-407-2414-8

Copyright © 2003 by E.V.D. van Loef

All rights reserved. No part of this material protected by copyright notice may be reproduced or utilised in any form or by any means, electronic or mechanical, including photocopying, recording or by any information storage and retrieval system, without the permission from the publisher: Delft University Press.

Printed in the Netherlands

“We think too small, like the frog at the bottom of the well.
He thinks the sky is only as big as the top of the well.
If he surfaced, he would have an entirely different view.”

Mao Tse-Tung

Contents

1. Introduction	1
1.1 Radiation	1
1.2 Radiation detection	1
1.3 Scintillators	2
2. Experimental Techniques	5
2.1 Introduction	5
2.2 X-ray excited optical luminescence	5
2.3 Vacuum Ultraviolet (VUV) excited life time measurements	7
2.4 VUV excitation and emission spectroscopy	7
2.5 Time-resolved excitation and emission spectroscopy	7
2.6 Pulse height measurements	9
2.7 Scintillation decay time	11
2.8 Time resolution measurements	12
 PART A. SCINTILLATORS FOR APPLICATIONS	
3. Medical Imaging	17
3.1 Introduction	17
3.2 Modalities	17
3.3 New inorganic scintillators	19
4. High-energy-resolution Scintillators: $\text{LaCl}_3:\text{Ce}^{3+}$ and $\text{LaBr}_3:\text{Ce}^{3+}$	23
4.1 Introduction	23
4.2 Characteristics	
4.3 Conclusions	33

PART B. SCINTILLATION MECHANISM

5. Scintillation	37
5.1 Introduction	37
5.2 The scintillation process	37
5.3 Defects	40
5.4 Energy transport	43
5.5 Luminescence	47
5.6 Summary	48
6. Scintillation mechanism in $\text{LaCl}_3:\text{Ce}^{3+}$ & $\text{LaBr}_3:\text{Ce}^{3+}$	51
6.1 Introduction	51
6.2 Results	51
6.3 Discussion	63
6.4 Conclusions	64
7. The Elpasolites – $\text{Cs}_2\text{LiYX}_6:\text{Ce}^{3+}$ (X = Cl, Br)	67
7.1 Introduction	67
7.2 Material	68
7.3 Results	68
7.4 Discussion	77
7.5 Conclusions	80
8. The lutetium halides – $\text{LuX}_3:\text{Ce}^{3+}$ (X = Cl, Br)	83
8.1 Introduction	83
8.2 Material	83
8.3 Results	83
8.4 Discussion	90
8.5 Conclusions	92
9. The ternary halides – $\text{K}_2\text{LaX}_5:\text{Ce}^{3+}$ (X = Cl, Br, I)	93
9.1 Introduction	93
9.2 Material	93
9.3 Results	94
9.4 Discussion	104
9.5 Conclusions	107

Conclusions	109
Summary	111
Samenvatting	115
Dankwoord / Acknowledgments	119
Curriculum Vitae	121
Publications and patents	123

1. Introduction

1.1 Radiation

It was on a dark November evening in 1895 that the German physicist Wilhelm C. Röntgen noticed a weak light shimmering on a little bench nearby while experimenting with a blackened cathode-ray tube. Highly excited, Roentgen lit a match, and, to his great surprise, discovered that the source of the mysterious light was a little barium platinocyanide screen lying on the bench. Röntgen concluded that the cathode-ray tube had to emit some new kind of radiation of an unknown type. To reflect his bewilderment, he called the new radiation 'X-rays.'

Only one year later, Becquerel discovered other types of ionising radiation when he observed that a uranium-containing compound was able to blacken a photographic plate, which was well covered by black paper and aluminium foil. When Becquerel announced his discovery of the new rays, it was Rutherford who proved that the new rays discovered by Becquerel were actually composed of three different forms of radiation. By carefully studying the absorption of the rays, he found that one component, which he called the 'alpha rays,' could be absorbed by a sheet of writing paper, or a few centimetres of air. In fact, Becquerel had not detected these alphas, because the box containing the film absorbed them. A second component, the 'beta rays,' Rutherford found to be one hundred times more penetrating. A third type of Becquerel rays were christened 'gamma rays' by Villard in 1900. These rays could penetrate several feet of concrete, but were essentially akin to X-rays but with much shorter wavelength.

Inextricably bound up with the discovery of X-rays and other types of ionising radiation is scintillator research. In fact, the compound Röntgen inadvertently used in order to detect the X-ray radiation was a scintillator (from 'scintilla,' which is Latin for spark). But also the uranium-containing compound Becquerel employed to demonstrate the existence of alpha, beta and gamma rays was a scintillating material. Soon, not only ionising radiation was subject of investigation, but also the scintillating material itself had become an area of research.

1.2 Radiation detection

In order to be able to detect radiation (X-rays, gamma rays) efficiently, one needs to understand the basic interaction mechanisms between the radiation and the detector. In principle, when X-rays or gamma rays pass a material, there is a certain probability that they have interaction and are absorbed. In the range of a few kiloelectronvolt (keV) to several megaelectronvolt (MeV), photoelectric effect, Compton scattering, and pair production are the dominant processes by which the X-rays or gamma rays are absorbed.

In the case of photoelectric effect, the total energy of the X-ray or gamma ray (photon) is transferred to a bound electron of the atom (mostly a K- or L-shell electron). The kinetic energy gain of the electron is simply the energy of the incident

radiation minus the binding energy of the electron. Compton scattering is the effect where a photon partially transfers its energy to a weakly bound electron. As a result, the energy of the incident photon is distributed among the Compton electron and the secondary photon. The latter may escape the material and only the electron contributes to the signal. The conversion of a photon into an electron and a positron is called pair production. This effect is only present for photon energies larger than 1.02 MeV.

After absorption of the X-rays or gamma rays, the created high energy primary electrons lose their energy by collisions with other electrons in the material, generating secondary electron and holes. This avalanche of secondaries continues until the energy of the electrons is no longer sufficient to further ionise the material. The excess energy is then lost by thermalisation. These ionisations consist of mainly electrons and holes that may be separated by an electric field and collected at electrodes. This method is mainly applied in gas and semiconductor based detectors that are most suitable for the detection of X-rays, low energy gamma rays and charged particles. For higher energy X-ray and gamma rays, scintillators are the more obvious choice.

1.3 Scintillators

The principle of radiation detection based on scintillators is the detection of ionising radiation by observing the scintillation light produced: when the electron and holes, created after absorption of radiation, recombine (or transfer their energy to a luminescent centre), the light is detected by a photomultiplier tube, a photodiode, or another light detector. The light detector in turn converts the light into an electric pulse. The intensity of the pulse is a measure for the absorbed energy.

The initial impetus to scintillator research was given by Edison, who discovered the well-known calcium tungstate scintillator after a comprehensive study of thousands of compounds. However, it was Hofstadter [1,2] just after the second World War who demonstrated that sodium iodide doped with thallium produced an exceptionally large scintillation light output. Since then, numerous other scintillating materials have been discovered, many with unique properties and applicability. Nowadays, inorganic scintillators are widely used for the detection of radiation in research, medical diagnostics and industry. Yet, for many applications a scintillator that meets all the requirements is not available. Especially for new digital diagnostic systems and real-time imaging applications, new inorganic scintillator materials are needed that have both a high light yield and a fast response. This is one of the reasons for continuous scintillator research and development. But also from a scientific point of view, scintillation materials are of great interest.

Up until recently, scintillator research has largely been a field of trial and error. Phenomenological models coupled to requirements such as high density, stability in air and ease of crystal growth were the main points of departure which led to the discovery of most of the scintillators used nowadays. In general, attention was focused on the characterisation of the scintillation properties, and theoretical work on scintillators is scarce. Only few studies present a more detailed investigation of the scintillation mechanism. Nevertheless, many inorganic materials were found to be efficient scintillators with a high light yield and good energy resolution. Unfortunately, the question why these materials showed such excellent scintillation

properties remained open, due to the lack of in-depth knowledge about the scintillation mechanism.

The investigations described in this thesis are therefore directed to address these two subjects in scintillator research. That is: (i) the search for new inorganic scintillators for gamma ray detection and (ii) the systematic research of the scintillation mechanisms in scintillator materials.

The thesis is organised as follows: In part A, chapter 3 a general introduction to X-rays in medicine and a review of medical applications and the most commonly used scintillators in that field are presented. The basic scintillator requirements for some medical imaging applications are reviewed and the properties of some new inorganic scintillator materials are presented. The choice of the studied compounds is motivated. Two new high-energy-resolution scintillators, $\text{LaCl}_3:\text{Ce}^{3+}$ and $\text{LaBr}_3:\text{Ce}^{3+}$ are presented in Chapter 4. It is shown that they have a high light yield, excellent energy resolution and timing properties. For applications where a good energy resolution is required, $\text{LaCl}_3:\text{Ce}^{3+}$ and $\text{LaBr}_3:\text{Ce}^{3+}$ are very promising scintillators and in many respects better than NaI:Tl .

Part B of this thesis deals with the concepts of scintillation, the process that leads to the formation of electrons and holes and, in particular, the scintillation mechanism. Chapter 5 gives a general introduction to scintillation. In the next four chapters, the scintillation mechanism is described in detail for four different types of compounds. The elpasolites with structural formula $\text{Cs}_2\text{LiYX}_6:\text{Ce}^{3+}$ ($\text{X} = \text{Cl}, \text{Br}$) are treated in Chapter 6, the properties and mechanism of the lutetium halides, $\text{LuX}_3:\text{Ce}^{3+}$ ($\text{X} = \text{F}, \text{Cl}, \text{Br}$) are discussed in Chapter 7, the scintillation mechanism in $\text{LaCl}_3:\text{Ce}^{3+}$ and $\text{LaBr}_3:\text{Ce}^{3+}$ is discussed in Chapter 8 and Chapter 9 deals with the ternary halides $\text{K}_2\text{LaX}_5:\text{Ce}^{3+}$ ($\text{X} = \text{Cl}, \text{Br}, \text{I}$). Finally, conclusions are drawn in chapter 10. First the experimental techniques used to study the compounds are discussed Chapter 2.

References

¹ R. Hofstadter, Phys. Rev. 74 (1948) 100.

² R. Hofstadter, Phys. Rev. 75 (1948) 796.

2. Experimental Techniques

2.1 Introduction

In this chapter, the techniques used to study the scintillating materials are described. The procedure followed to chart the properties of these crystals was in many cases the same. First, an impression of the optical characteristics of the scintillating material was obtained by performing X-ray excited optical luminescence spectroscopy, vacuum ultraviolet (VUV) excitation and emission measurements, and time resolved excitation and emission measurements using synchrotron radiation. Then, experiments using gamma ray radiation were carried out. These concern pulse height spectra giving information on light yield and scintillation decay time measurements. Information on the lifetime of the excited state of defects was obtained by selective excitation with a hydrogen flash lamp.

2.2 X-ray excited optical luminescence

Figure 1 depicts schematically the set-up used for X-ray excited optical luminescence spectroscopy. The X-ray excited optical luminescence spectra were recorded in reflection mode using an X-ray tube with a Cu-anode (XR). The maximum power dissipation of the tube is 2 kW, but typically, the anode was operated at 35 kV and 25 mA. The sample under study is mounted in the sample holder (S1). The emission from the sample is dispersed by an Acton Research Company (ARC) VM-504 monochromator (M) and detected by a Hamamatsu R943-02 photomultiplier tube (PMT) (P2) or an EMI 9426 PMT (P1). The ARC VM-504 monochromator is of the Czerny-Turner configuration. It has a 0.39-meter focal length, featuring triple indexable plane gratings (1200 grooves/mm, blazed at 150 nm, 300 nm, and 750 nm, respectively) and two movable diverter mirrors. Both the sample chamber and the monochromator are operated under vacuum. The wavelength accuracy of about ~ 1 nm. All spectra presented in the thesis were corrected for the wavelength dependence of the photodetector quantum efficiency as well as monochromator transmission.

Temperature dependent X-ray excited optical luminescence measurements were performed between 80 and 400 K using a Cryospec model 20A Joule-Thomson Miniature Refrigerator operated with 99.999% purity nitrogen gas at 120 bar. The temperature resolution is typically 5 K. The temperature measurements, in absolute terms, are limited by experimental factors such as the thermal coupling between the control stage and the sample.

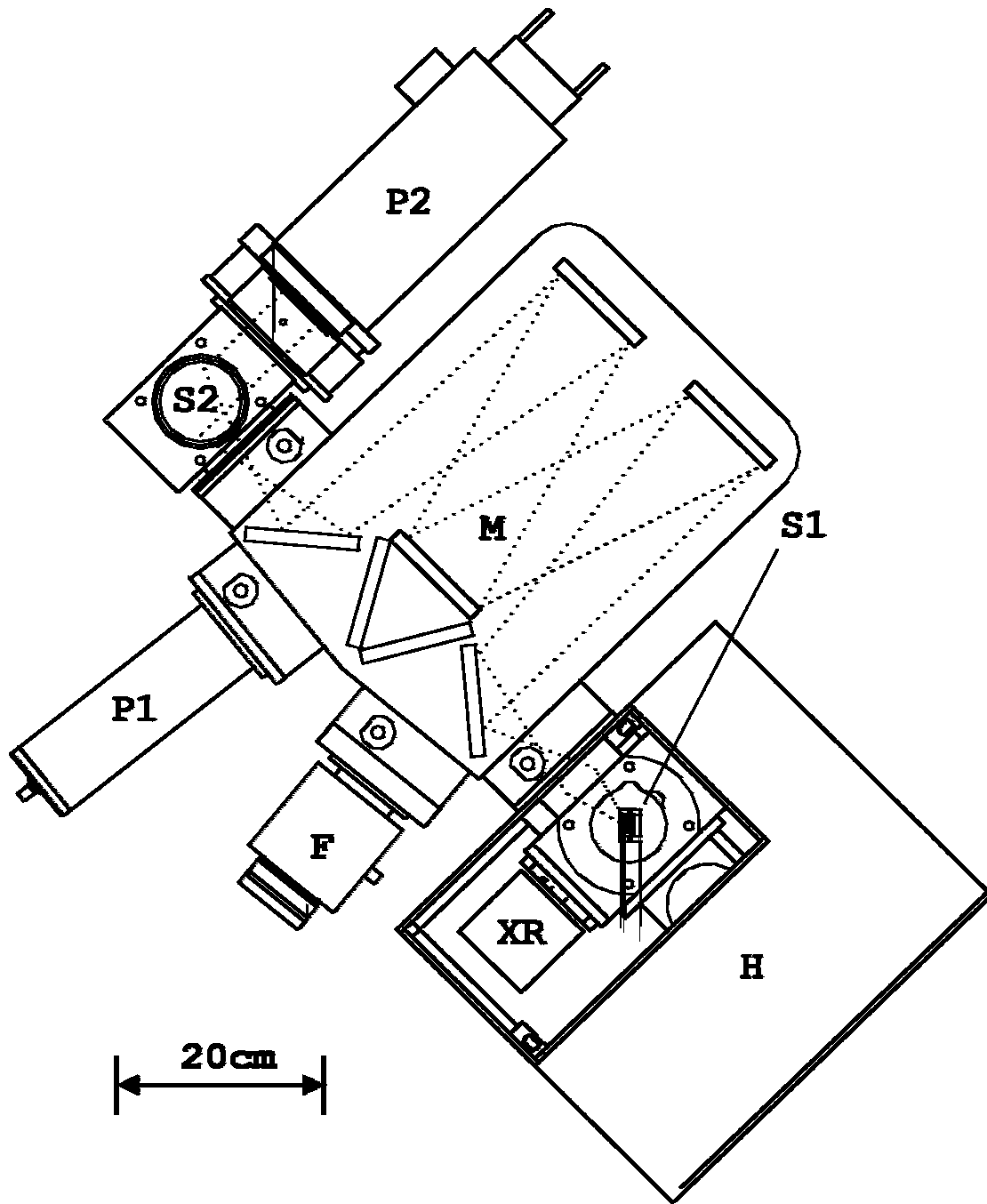


Figure 1: Schematic representation of the set-up used for X-ray excited optical luminescence spectroscopy, with XR = X-ray tube, H = housing, S1 = sample chamber 1, S2 = sample chamber 2/ mirror, F = IBH Consultants Ltd. 5000F hydrogen coaxial flashlamp M = monochromator, P1 = EMI 9426 PMT, and P2 = Hamamatsu R943-02 PMT.

2.3 Vacuum Ultraviolet (VUV) excited life time measurements

VUV excited lifetime spectra were recorded using an IBH Consultants Ltd. hydrogen coaxial flashlamp model 5000F (pulse FWHM ~ 1 ns), see Figure 1 (F). The luminescence is dispersed through an ARC VM504 monochromator (blazed at 300 nm, 1200 grooves/mm) (M). The sample (S2) is excited by the light dispersed through the monochromator and the emission from the crystal is measured in reflection at 90 degrees angle using a quartz lens and a cooled Hamamatsu R943-02 photomultiplier tube (cooling housing model TE-104 from Products for Research) (P2) in combination with interference filters and/or cut-off filters.

2.4 VUV excitation and emission spectroscopy

Excitation and emission spectra, between 150 and 300 nm, and 250 and 600 nm, respectively, were recorded using a Vacuum Ultraviolet (VUV) set-up, see Figure 2. It consists of an ARC type DS-775 deuterium discharge lamp (L), an excitation monochromator (ARC, model VM502 with 1200 grooves/mm blazed at 250 nm with Al/MgF₂ coating for high reflectivity in the VUV region) (M1), MgF₂ windows, a focussing unit (F), a sample chamber with MgF₂ lenses (S), and an emission monochromator (Macan 910 with 1200 grooves/mm blazed at 350 nm) (M2) with a Philips XP2254/B PMT (P2). The sample holder as well as the excitation monochromator is operated at vacuum. All spectra presented in the thesis were corrected for the wavelength dependence of the photodetector quantum efficiency as well as monochromator transmission, using sodium salicylate as a reference.

2.5 Time-resolved excitation and emission spectroscopy

High resolution, time-resolved excitation and emission spectra were recorded using synchrotron radiation at the SuperLumi experimental set-up of the Synchrotron Strahlungslabor (HASYLAB) at the Deutsches Elektronen Synchrotron (DESY) in Hamburg, Germany. A schematic representation of the SuperLumi experimental set-up is shown in Figure 3.

The entrance optics of the SuperLumi experimental set-up consists of two mirrors for separate vertical and horizontal focusing. The first, cylindrical mirror is located at a distance of 4.3 m from the source and accepts 50 mrad of the horizontal divergence. The second, plane elliptic mirror focuses the 2.2 mrad vertical divergence to 0.1 mm at the entrance slit of the monochromator. Both mirrors can be aligned by remote control. The excitation monochromator (PM) is a 2 m normal incidence monochromator (McPearson Company) equipped with two gratings that can be interchanged in situ (1200 grooves/mm, blazed at 150 nm and 300 nm, respectively). One can choose between three different, fixed entrance slits, 0.03 mm, 0.1 mm and 0.5 mm in width. With appropriate exit slits, this corresponds to a resolution of 0.02 nm, 0.05 nm and 0.23 nm respectively. The monochromator has two exit arms which can be used alternately by moving a plane mirror into the light path.

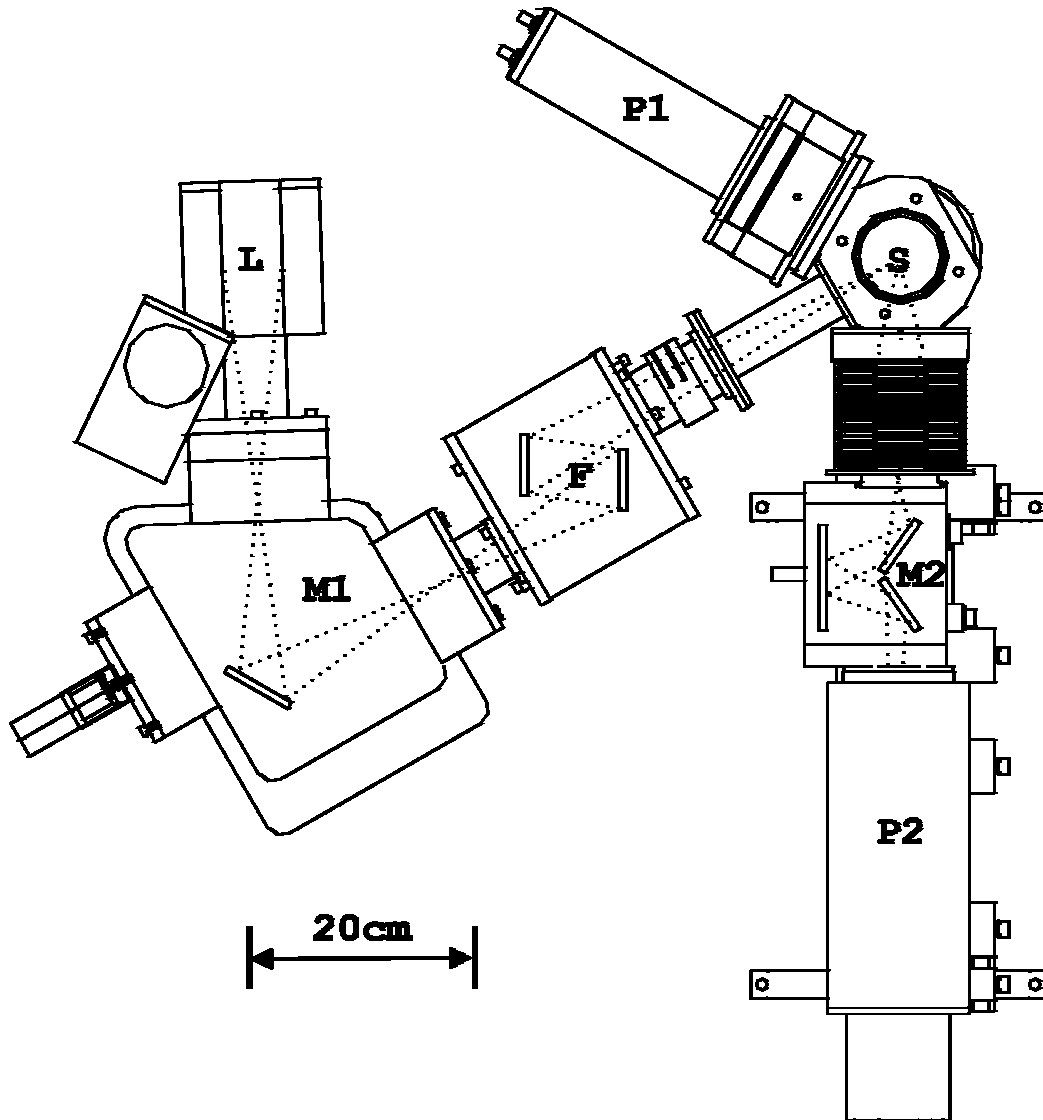


Figure 2: Schematic representation of the vacuum ultraviolet set-up, with L = ARC type DS-775 deuterium discharge lamp, M1 = excitation monochromator (ARC, model VM502 with 1200 grooves/mm blazed at 250 nm with Al/MgF₂ coating for high reflectivity in the VUV region), M2 = emission monochromator (Macan 910 with 1200 grooves/mm blazed at 350 nm), F = focussing unit, S = sample chamber with MgF₂ lenses, P1 = EMI PMT and P2 = Philips XP2254/B PMT.

The synchrotron is operated in the multibunch regime (5 bunches) with almost 200 ns distance between successive bunches. An elaborate description of both the SuperLumi set-up and the synchrotron operation characteristics can be found in [1]. Emission spectra were recorded using single photon counting techniques. Photons were counted within a time window of approximately 10 ns at the start of the synchrotron luminescence pulse. Another time window of the order of 100 - 200 ns was used at the end of the pulse to discriminate between fast and slow luminescence components. Also the integral count rate was recorded.

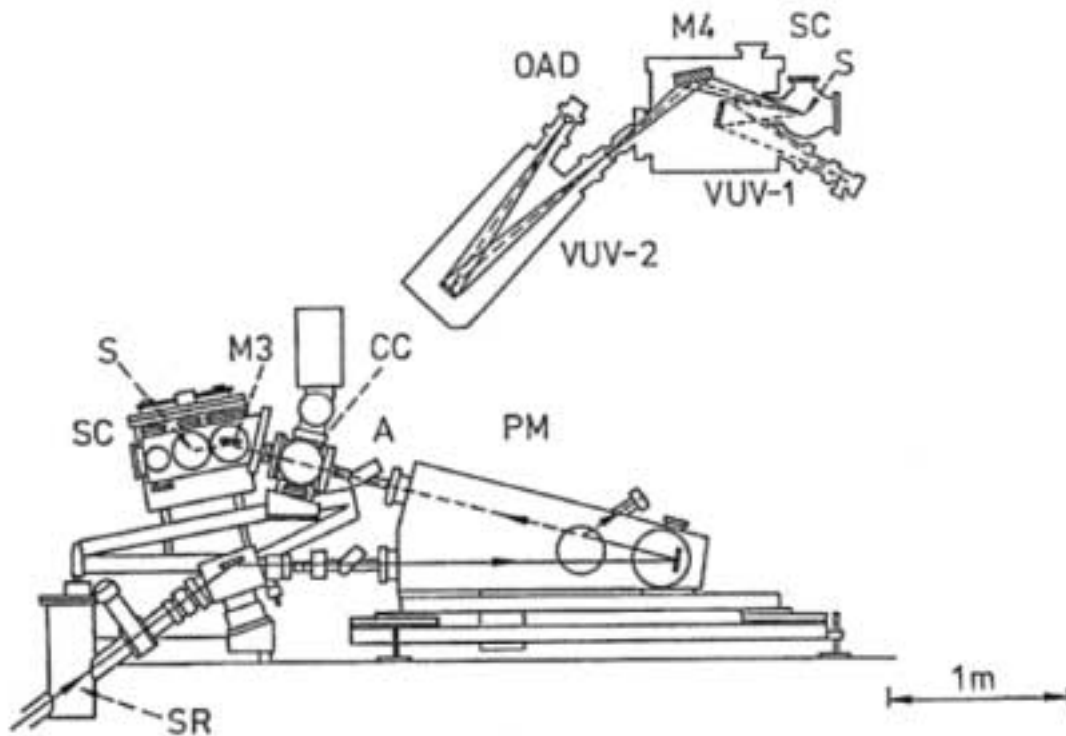


Figure 3: Schematic representation from [1] of the SuperLumi experimental set-up at DESY, Hamburg, with SR = synchrotron radiation, PM = primary monochromator, A = exit arm, CC = chopper chamber, S = sample, SC = sample chamber, M3-M4 = mirrors, OAD = position-sensitive detector and VUV-1/2 = emission monochromators.

2.6 Pulse height measurements

Pulse height measurements are generally performed to obtain information on the light yield of the scintillating material under ionising radiation [2]. A typical set-up for recording pulse height spectra is shown schematically in Figure 4. First, the crystal is optically coupled to the window of the PMT with silicon-based grease (Viscasil 60,000 cSt, General Electric). To collect as much light as possible, it is wrapped in several layers of 0.1mm thick UV reflecting Teflon tape. Gamma rays and/or X-rays emanating from a radioactive source excite the crystal. In most cases a ^{137}Cs source is used. The scintillation light is detected by a Hamamatsu R1791 PMT (P). The output signal is integrated with a home-made pre-amplifier of the charge-sensitive type (A1), having an RC-time of 50 μs . Next, the signal is amplified once again and filtered using Gaussian shaping by an Ortec 572/672 spectroscopic amplifier (A2). Shaping times of 0.5 to 10 μs are available. Here, 'shaping time' is defined as the time during which the output of the preamplifier is being integrated and shaped into a Gaussian pulse. Finally, the analogue signal is converted to a digital pulse by a conventional ADC unit (ADC). That way, the signal can be stored and processed by a computerised data handling system (PC).

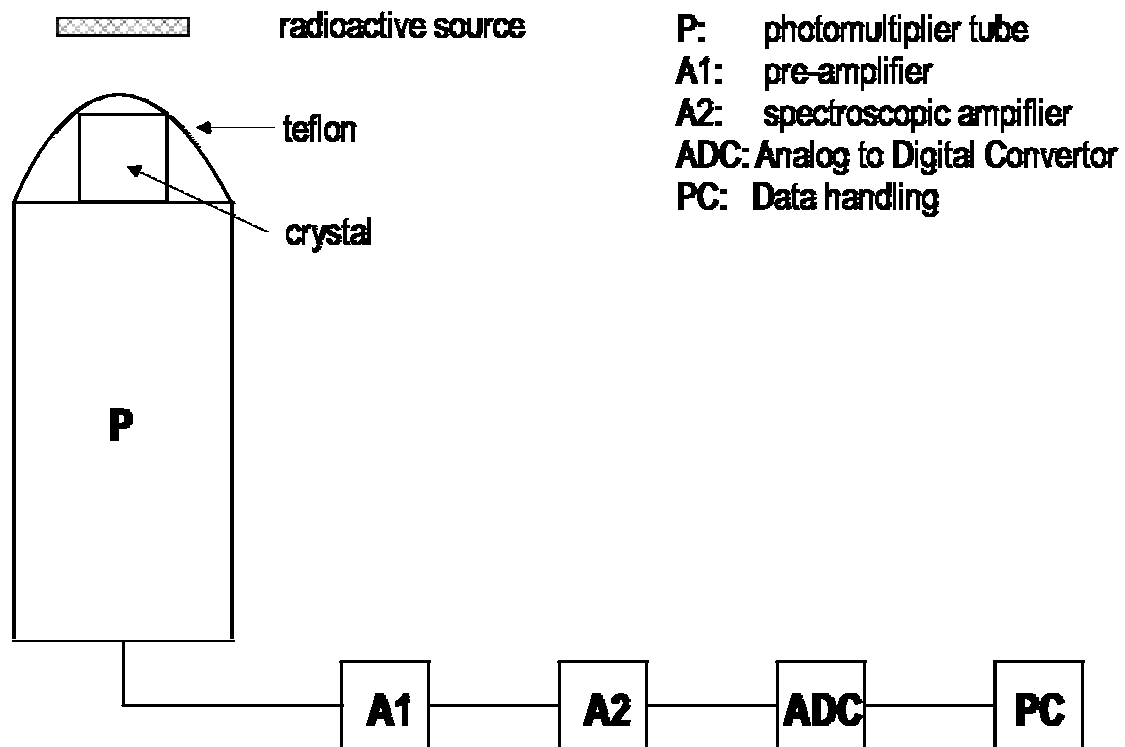


Figure 4: Block scheme of the experimental set-up used for recording pulse-height spectra.

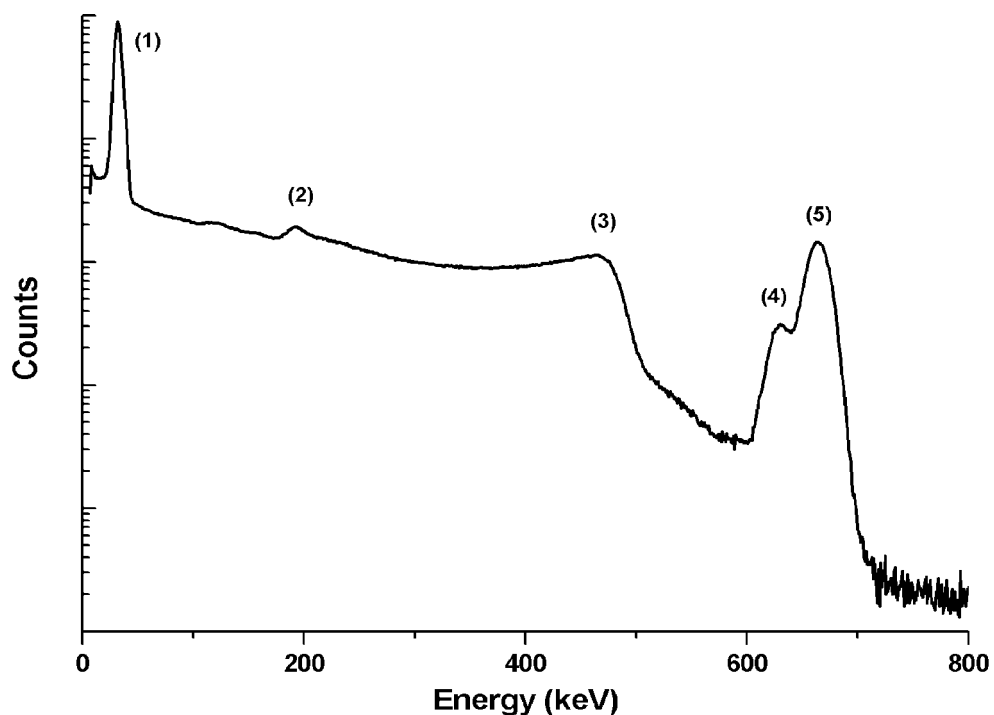


Figure 5: Pulse height spectrum of γ -rays and X-rays from a ^{137}Cs source recorded with a $\text{LaCl}_3:\text{Ce}^{3+}$ crystal.

An example of a pulse height spectrum is given in Figure 5 for gamma rays of a ^{137}Cs source measured with a $\text{LaCl}_3:\text{Ce}^{3+}$ crystal. In the pulse height spectrum, several peaks can be observed. The rightmost peak (5) is created by scintillation events in which the total energy of the gamma-ray photon is absorbed by the scintillator. This

peak is called the photopeak or the full energy peak. At somewhat lower energy a small peak (4) can be observed as a shoulder of the photopeak. It is due escape of X-rays (in this case of lanthanum) the scintillation crystal after absorbing the gamma ray photon. If a gamma ray photon interacts with the scintillating material by means of the Compton Effect, the scattered photon may easily escape from the crystal and only the recoil electron is absorbed. These events give rise to the Compton continuum from the Compton edge (3) down to zero energy. The peak at (2) is the backscatter peak. It arises from scattering of the gamma rays from casing of the crystal, the PMT and materials outside the system, back into the scintillation crystal. Ba X-rays also emitted in ^{137}Cs decay cause the leftmost peak at (1).

Scintillation yields expressed in photoelectrons per MeV of absorbed γ -ray energy (phe/MeV) can be calculated by comparing the peak position of the photopeak to that of the single electron spectrum [3]. In order to transform the number of photoelectrons per MeV into an absolute light yield expressed as the number of photons per MeV of absorbed γ -ray energy (ph/MeV) the overall detection efficiency of the PMT has to be known. The detection efficiency $\eta_D(\lambda)$ is given by:

$$\eta_D(\lambda) = \eta_Q(\lambda)\eta_C\eta_L \quad (1)$$

where $\eta_Q(\lambda)$ is the quantum efficiency of the PMT, η_C is the charge collection efficiency of the photoelectrons emanating from the photocathode and η_L is the light collection efficiency which represents the fraction of the light emitted by the crystal reaching the photocathode.

The quantum efficiency $\eta_Q(\lambda)$ of the R1791 Hamamatsu photomultiplier tube was provided by the manufacturer of the tube. The charge collection efficiency η_C was estimated to be 0.95 ± 0.05 [4]. The light collection efficiency η_L was estimated by us at 0.95 ± 0.05 . The number of photons per MeV of absorbed γ -ray energy N_{ph} is calculated by multiplying the number of photoelectrons per MeV of absorbed γ -ray by the average quantum efficiency of the PMT:

$$N_{phe} = N_{ph} \frac{\int I_{Xray}(\lambda)\eta_D(\lambda)d\lambda}{\int I_{Xray}(\lambda)d\lambda} \quad (2)$$

where $I_{Xray}(\lambda)$ is the intensity distribution of the x-ray excited emission spectrum of the crystal.

2.7 Scintillation decay time

Scintillation decay time spectra at time scales up to 200 μs were recorded by the multi-hit method described by W.W. Moses [5] with XP2020Q PMTs, LeCroy 934 Constant Fraction Discriminators (CFDs) and a LeCroy 4208 Time to Digital Converter (TDC). A schematic of the experimental set-up is shown in Figure 6.

Two measurement configurations were used. In the first method, called the “conventional method” in this thesis, the sample under study is mounted on the “start” PMT and is excited by gamma rays from a ^{137}Cs source. If a gamma ray is absorbed in the crystal, the generated scintillation pulse is detected by the “start” PMT and - if the scintillation intensity is sufficiently high - converted into a “start” timing. The “stops”

are derived from the detection of single photons detected by the “stop” PMT. In turn, they are converted into “stop” timing pulses. The time between “start” and “stop” timing pulses is then digitised. After recording a large number of scintillation events, the number of single photons detected per scintillation event in a time interval $t, t + dt$ (where dt is the TDC time resolution) is plotted as a function of t . As such, the time distribution equals the shape of the scintillation pulse.

For scintillating materials that have a relatively low light yield, the “coincidence method” is employed. In this case, only a small number of photoelectrons are generated in the “start” PMT. This will give rise to a worsening of the signal to noise ratio and leads to a jitter in the starting moment. To prevent this jitter, a BaF₂ crystal is mounted on the “start” PMT instead of the crystal under study. The latter is positioned between the “start” PMT and the slit. A ²²Na source is placed between these two crystals. This source produces a positron, which recombines with an electron under the emission of two collinearly emitted 511 keV photons. One of the 511 keV photons is detected by the BaF₂ crystal leading to a high intensity fast scintillation pulse that is detected by the “start” PMT. The other 511 keV photon excites the crystal under study and the scintillation photons emitted are detected by the “stop” PMT.

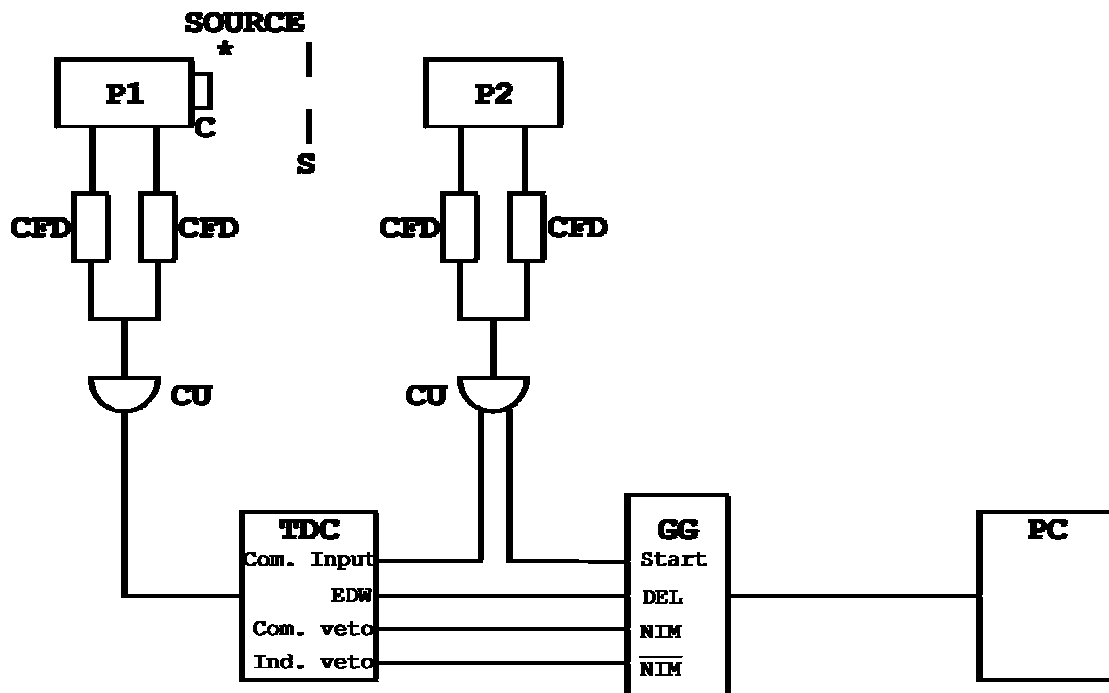


Figure 6: Schematic representation of the experimental set-up used to record scintillation decay time spectra, with P1 = “start” PMT (Philips XP2020Q), P2 = “stop” PMT (Philips XP2020Q), C = scintillation crystal, S = slit, CFD = Constant Fraction Discriminator (LeCroy 934), CU = Coincidence unit (LeCroy 465), TDC = Time to Digital Converter (LeCroy 4208), GG = Gate generator (LeCroy 222) and PC = data handling.

2.8 Time resolution measurements

Time resolution measurements were recorded with the set-up of the coincidence method (see previous paragraph) using XP2020Q PMTs, a ⁶⁰Co source and constant-fraction time with an energy threshold set at $E \geq 800$ keV. A $\varnothing 2.5 \times 0.8$ cm³ fast

scintillating BaF₂ crystal was coupled to the “start” PMT. The sample under study is mounted on the “stop” PMT and the ⁶⁰Co source is placed near the stop tube between the two crystals. The ⁶⁰Co source emits a gamma of 1.173 MeV and a gamma of 1.332 MeV in coincidence. The time differences between the moments of detection of the coincident gamma ray quanta in the two crystals are accumulated in the time-resolution spectrum. Only events from gamma-ray quanta with energy larger than about 800 keV were accepted. The time resolution is defined as the width of the time resolution peak at half maximum.

References

¹ G. Zimmerer, Nucl. Instr. Meth. A 308 (1991) 178.

² G.F. Knoll, “Radiation Detection and Measurement,” 3rd edition, J. Wiley & Sons, New York, U.S.A., 2000, ch. 4 and 18.

³ P. Dorenbos, J.T.M. de Haas, R. Visser, C.W.E. van Eijk, R.W. Hollander, IEEE Trans. Nucl. Sci. 40 (1993) 424.

⁴ “Photomultiplier Tube, Principle to Application, Hamamatsu Photonics K.K., Data Process Laboratory K.K., 1994, ch. 3.

⁵ W.W. Moses, “A method to Increase optical timing spectra measurement rates using a multi-hit TDC”, Life Sciences Division, Lawrence Berkeley Laboratory, University of California, Berkeley, California.

Part A

SCINTILLATORS FOR APPLICATIONS

3. Medical Imaging

3.1 Introduction

With the advent of X-rays also came the frivolous experiments. Demonstrations of the power of the rays were being held at colleges, in high schools, and in public venues. Radiograph of hands, feet and other human limbs were made and line drawings of the radiographs were being sold as souvenirs. Also the medical profession acknowledged the extraordinary potential of the new rays, and not long after their actual discovery, surgeons used the X-rays to examine the bones of living people [1,2].

At the same time the diagnostic powers of X-rays were being investigated, some experimenters investigated the application of the rays to disease. By the end of 1896, several researchers had noted the palliative effects of the rays on painful cancers. Others found remarkable results in the treatment of lesions and skin problems, while others investigated the possible bactericidal action of the rays. However, the unrestrained use of the X-ray for display and amusement soon appeared to be less harmless than people originally thought. Among the reported problems associated with X-rays were redness, numbness, epilation, infection, and severe pain. It was not until the beginning of the 20th century that medical observers took seriously the notion that the rays could prove fatal. Only slowly, action was taken to minimise the accidental exposure to X-rays and think about protection and safety. Over time, the X-rays proved to be a fruitful medical diagnostics tool, provided that precautionary safety measures were taken to minimise the exposure of people. But also the gamma rays discovered by Becquerel turned out to be useful in the treatment of diseases and in medical imaging. Nowadays, several medical apparatus are being used in hospitals, either based on the X-rays of Roentgen or the gamma rays of Becquerel.

In this chapter several medical imaging applications and the most commonly used scintillators in that field are reviewed. The basic scintillator requirements for some medical imaging applications are summarised and the properties of some new inorganic scintillator materials are presented. The choice of the studied compounds is motivated.

3.2 Modalities

Traditionally, inorganic scintillators have played an important role in the detection and visualisation of radiation. In medical diagnostic imaging modalities using X-rays or gamma rays, inorganic scintillators are ubiquitous. The most common techniques applied include radiography, fluoroscopy, scintigraphy, X-ray Computed Tomography (CT), and Positron Emission Tomography. Here we will address only CT and radionuclide imaging modalities briefly. For a more elaborate review on modalities and the use of scintillators see [3].

3.2.1 Computed Tomography

Radiographic procedures require the production of an X-ray beam into which the anatomy being evaluated is placed. The fraction of the X-rays that is not absorbed by the body is then used to expose a detector. This is in many cases a film. In CT, the body is consecutively irradiated from a large number of directions. Thus, a 3-D picture of a part of the body can be reconstructed. In X-ray CT, energies in the range up to ~ 140 keV are used and consequently, an inorganic scintillator is the most obvious choice as detector medium.

The basic scintillator requirements for CT are, in order of decreasing importance, low afterglow, high stability, high density and effective Z for efficient X-ray detection, and high luminous efficiency [4]. The most popular scintillators for CT are CdWO_4 , $\text{Bi}_4\text{Ge}_3\text{O}_{12}$ (BGO), $(\text{Y,Gd})_2\text{O}_3:\text{Eu,Pr}$, and $\text{Gd}_2\text{O}_2\text{S}:\text{Pr,Ce,F}$. These scintillators have relatively high densities and effective Z^\dagger , required for efficient radiation detection, but are relatively slow. See Table I.

3.2.2 Radionuclide Imaging & Positron Emission Tomography

Scintigraphic or radionuclide medical procedures are a diagnostic service that uses isotopes to image organs and study their function. Therefore, pharmaceuticals labelled with radioactive isotopes (radiopharmaceuticals) are introduced into the body. The gamma radiation emitted by the isotope is used for simple projections (scintigraphy) or single photon emission computed tomography (SPECT). In contrast, positron emission tomography (PET) is based on the collinear emission of two 511 keV photons from the decay of a positron-emitting pharmaceutical to obtain an image.

In the case of scintigraphy or SPECT, a gamma camera is used to detect the radiation. The most commonly used detector for SPECT is the Anger camera, which is named after its inventor. The scintillator requirements for SPECT are, in the order of decreasing importance, high luminous efficiency, high density, and short decay time, and a proportional energy response [5]. Of the present scintillators, sodium iodide doped with thallium, NaI:Tl is used most, because of its high light yield and reasonable fast decay time.

Table I. Overview of some scintillators for medical imaging applications.

Scintillator	Density (g/cm^3)	Attenuation Coefficient (cm^{-1} @ 511 keV)	Light yield (ph/MeV)	λ (nm)	τ (ns)	Ref.
CdWO_4	7.90	0.886	19,700	495	$\sim 10^4$	[5,6]
$\text{Bi}_4\text{Ge}_3\text{O}_{12}$	7.13	0.964	8,900	480	300	[6-8]
$(\text{Y,Gd})_2\text{O}_3:\text{Eu,Pr}$	5.9	0.503 - 0.637	19,000	610	$\sim 10^6$	[5,9]
$\text{Gd}_2\text{O}_2\text{S}:\text{Pr,Ce,F}$	7.34	0.786	40,000	510	$\sim 10^3$	[9]
NaI:Tl	3.67	0.343	40,000	415	230	[6, 10]
$\text{Gd}_2\text{SiO}_5:\text{Ce}$	6.71	0.704	7,000	430	300	[11,12]
$\text{Lu}_2\text{SiO}_5:\text{Ce}$	7.4	0.869	30,000	420	40	[13,14]
$\text{LuAlO}_3:\text{Ce}$	8.34	0.956	11,400	365	~ 17	[15,16]
$\text{LuPO}_4:\text{Ce}$	6.53	0.735	17,200	360	25	[17]

[†] The definition of “effective Z ” is given in chapter 5, section 2.

Positron emission tomography (PET) requires the simultaneous detection of the two positron annihilation quanta with high efficiency. Therefore, one needs a scintillator that has a short attenuation length for 511 keV radiation, a short decay time, and a high luminous efficiency. BGO is the most used scintillator because of its good detection efficiency and large probability of photoelectric effect (40%) for 511 keV quanta. Nevertheless, other scintillators have also been applied, depending on cost and availability. Examples are NaI:Tl for a “poor men’s” PET system employing two gamma cameras, but also $\text{Gd}_2\text{SiO}_5\text{:Ce}$ (GSO) and $\text{Lu}_2\text{SiO}_5\text{:Ce}$ (LSO) have been employed. The latter two have reasonable density and scintillation decay time. In recent years, more and more lutetium-based compounds have emerged in the field of dense, high Z materials that could be applied in PET systems. Examples are $\text{LuAlO}_3\text{:Ce}$ (LuAP) and $\text{LuPO}_4\text{:Ce}$ (LuPO). See also Table I.

3.3 New inorganic scintillators

As was shown before, the radiation detector requirements for various diagnostic methods differ considerably and are not always met by commercially available scintillators. Ideally, a scintillator should have a high light yield (for good energy and position resolution), a fast response time (for good time resolution), high density and atomic number Z for efficient X-ray and gamma ray detection. Obviously, there are many other criteria such as transparency of the material to its own emission, ease of crystal growth, stability in air, and the matching of the scintillation wavelength spectrum with the sensitivity curve of the light detectors. However, there is no material that meets all these criteria and the choice of a particular scintillator is often a compromise among these and other factors. That is why there is continuous scintillator R&D. Other reasons for the development of new scintillators with specific properties may be found in non-medical applications like oil well logging and X-ray astronomy. Here, stability against extreme temperatures and good energy resolution prevail over cost and density.

In the search for new and efficient scintillators, most efforts have been directed to cerium-doped crystals. As is known for a long time, trivalent cerium emits fast scintillation (15 ~ 60 ns) in the 300-600 nm wavelength region. In many cases, the light output is high. To make a selection of cerium-doped crystals that stand a chance to become attractive, new inorganic scintillators, cerium-doped oxides seem to be the most obvious compounds to study in the sense that, in general, oxide crystals can be found of high density and high Z , and they are stable under normal atmospheric conditions and relatively easy to grow. Rarely are studies reported devoted to cerium-activated halide compounds. That is probably due to the hygroscopic nature of most of these materials. Nevertheless, the hygroscopicity needs not to be of great concern when the material seems to have very good scintillation properties. An example is NaI:Tl, mentioned earlier.

If the demands for radiation detection mainly comprise sufficient attenuation power, as well as good timing properties, a scintillator with a high density, effective Z , and a short scintillation decay time is required. In the family of cerium-activated halide compounds, both CeF_3 [18,19] and $\text{LuF}_3\text{:Ce}$ [20] meet these requirements. These are dense and fast scintillators, but they have a low light yield. In recent years more and more studies have been devoted to chloride and bromide based scintillators. An example is CeCl_3 [21]. This scintillator shows a relatively high light yield with a fairly short decay time. Its density however, is rather low.

Scintillators with both a high light yield and good energy resolution are $K_2LaCl_5:Ce$ [22,23] and $RbGd_2Br_7:Ce$ [24,25]. The latter compound shows a scintillation light output close to the theoretical maximum and an unequalled energy resolution of about 4%. Unfortunately, K_2LaCl_5 presents a rather long decay component and both K_2LaCl_5 and $RbGd_2Br_7$ contain radioactive isotopes, i.e. ^{40}K and ^{87}Rb . The properties of the scintillators mentioned above are gathered in Table II.

Recently, the scintillation properties of $LaCl_3:Ce$ 0.57% were published by Guillot-Noël et al. [26]. Unfortunately, both timing resolution and energy resolution of this compound left much to be desired. Nevertheless, it was thought that the scintillation properties and especially the scintillation decay could be improved by increasing the cerium concentration. In the next chapter we present the specifications relevant for detector applications of two new inorganic scintillators, $LaCl_3:Ce$ and $LaBr_3:Ce$. It is shown that they combine a high light yield, excellent energy resolution and fast timing properties. For applications where a good energy resolution is required, $LaCl_3:Ce$ and $LaBr_3:Ce$ seem to be very promising scintillators and competitive with $NaI:Tl$.

Table II. Properties of halide scintillators.

Scintillator	ρ (g/cm ³)	Z_{eff}	Light yield (ph/MeV)	Resolution (%, @662keV)	λ (nm)	τ (ns)
CeF ₃	6.16	53.3	4,400	-	330	28
LuF ₃ :Ce	8.3	66.2	8,000	-	310	28
CeCl ₃	3.9	50.4	28,000	-	360	25 (70%)
K_2LaCl_5 :10% Ce	2.89	44.1	30,000	5.1	380	80 (10%)
$Rb_2Gd_2Br_7$:10% Ce	4.79	50.6	56,000	3.8	420	43 (56%)

References

- ¹ R.L. Eisenberg, M. L. Powell, "Radiology: An Illustrated History", Mosby Year Book, St. Louis, U.S.A., 1991.
- ² O. Glasser, "Wilhelm Conrad Röntgen and the early history of the Röntgen rays", Norman publishing, San Francisco, 1993.
- ³ C.W.E. van Eijk, Phys. Med. Biol. 47 (2002) R85.
- ⁴ W.W. Moses. "Scintillator Requirements for Medical Imaging," Proceedings of the international conference on Inorganic Scintillators and their applications, August 16-20, 1999, Moscow, Russia, p. 11.
- ⁵ I. Holl, E. Lorenz, G. Margeras, IEEE Trans. Nucl. Sci. 35 (1998) 105.
- ⁶ D.R. Kinloch, W. Novak, P. Raby, I. Toepke, IEEE Trans. Nucl. Sci. 41 (1994) 752.
- ⁷ O.H. Nestor, C.Y. Huang, IEEE Trans. Nucl. Sci. NS-22 (1975) 68.
- ⁸ M. Moszynski, C. gresset, J. Vacher, R. Odru, Nucl. Instr. Meth. 188 (1981) 403.
- ⁹ B.C. Grabmaier, W. Rossner, T. Berthold, "Phosphors in x-ray computed tomography and for the γ -ray anger-camera," Proceedings of the international conference on Inorganic Scintillators and their applications, August 28 – September 1, 1995, Delft University Press, Delft, The Netherlands, p. 29.
- ¹⁰ M. Moszynski, M. Kapusta, J. Zalipska, M. Balcerzyk, D. Wolski, M. Szawlowski, W. Klamra, IEEE Trans. Nucl. Sci. 46 (1999) 880.
- ¹¹ K. Takagi, T. Fukazawa, Appl. Phys. Lett. 42 (1983) 43.
- ¹² H. Ishibashi, K. Shimizu, K. Susa, S. Kubota, IEEE Trans. Nucl. Sci. 36 (1989) 170.
- ¹³ C.L. Melcher, J.S. Schweitzer, Nucl. Instr. Meth. Phys. Res. A 314 (1992) 212.
- ¹⁴ C.L. Melcher, J.S. Schweitzer, IEEE Trans. Nucl. Sci. 39 (1992) 502.
- ¹⁵ W.W. Moses, S.E. Derenzo, A. Fyodorov, M. Korzhik, A. Gektin, B. Minkov, V. Aslanov, IEEE Trans. Nucl. Sci. 42 (1995) 275.

-
- ¹⁶ M. Moszynski, D. Wolski, T. Ludziejewski, M. Kapusta, A. Lempicki, C. Brecher, D. Wiesniewski, A.J. Wojtowicz, Nucl. Instr. Meth. Phys. Res. A 385 (1997) 123.
- ¹⁷ A. Lempicki, E. Berman, A.J. Wojtowicz, M. Balcerzyk, IEEE Trans. Nucl. Sci. 40 (1993) 384.
- ¹⁸ D.F. Anderson, IEEE Trans. Nucl. Sci. 36 (1989) 137.
- ¹⁹ W.W. Moses, S.E. Derenzo, IEEE Trans. Nucl. Sci. 36 (1989) 173.
- ²⁰ B. Moine, C. Dujardin, H. Lautesse, C. Pedrini, C.M. Combes, A. Belsky, P. Martin, J.Y. Gesland, Mat. Sci. Forum 239-241 (1997) 245.
- ²¹ S.E. Derenzo, W.W. Moses, in "Heavy scintillators for Scientific and Industrial Applications", Proceedings of the "Crystal 2000" International Workshop, Edition Frontières, Gif-sur-Yvette, France, 1993, p. 125.
- ²² J.C. van't Spijker, P. Dorenbos, J.T.M. de Haas, C.W.E. van Eijk, H.U. Güdel, K. Krämer, Rad. Meas. 24(4) (1995) 379.
- ²³ J.C. van't Spijker, P. Dorenbos, C.W.E. van Eijk, K. Krämer, H.U. Güdel, J. Lumin. 85 (1999) 1.
- ²⁴ P. Dorenbos, J.C. van't Spijker, O.W.V. Frijns, C.W.E. van Eijk, K. Krämer, H.U. Güdel, A. Ellens, Nucl. Instr. Meth. Phys. Res. B 132 (1997) 728.
- ²⁵ O. Guillot-Noël, J.C. van't Spijker, J.T.M. de Haas, P. Dorenbos, C.W.E. van Eijk, K.W. Krämer, H.U. Güdel, IEEE Trans. Nucl. Sci. 46 (1999) 1274.
- ²⁶ O. Guillot-Noël, J.T.M. de Haas, P. Dorenbos, C.W.E. van Eijk, K. Krämer, H.U. Güdel, J. Lumin. 85 (1999) 21.

4. High-energy-resolution Scintillators:

LaCl₃:Ce³⁺ and LaBr₃:Ce³⁺

4.1 Introduction

The possibility to discriminate between gamma rays with slightly different energies by means of a scintillation detector is of great importance for e.g. X-ray astronomy, medical imaging and gamma-ray spectroscopy in general. This quality is characterised by the energy resolution defined as full width half maximum (FWHM) over peak position. A typical energy resolution for 662 keV gamma rays absorbed in a NaI:Tl detector is ~6%. At 5.9 keV, a value of ~ 45% is common. Since long, the alkali halides NaI and CsI activated by small amounts of thallium - and CsI also with sodium - have been the scintillators of choice, because these materials can be made in large single crystals, show efficient gamma-ray attenuation, are efficient light producers and have reasonable energy resolution. NaI:Tl was discovered in 1948 by Hofstadter [1,2] while CsI:Tl [3] and CsI:Na [4,5] came along in the mid-1960s.

In this chapter we report on the optical and scintillation properties of LaCl₃ and LaBr₃ crystals doped with different Ce³⁺ concentrations. Previously in the work by Guillot-Noël et al. [6], a LaCl₃ sample doped with 0.57% Ce³⁺ was studied. At this concentration there appears to be a competition between slow host related self-trapped-exciton (STE) emission and fast Ce³⁺ emission. In order to favour the fast Ce³⁺ emission it was decided to further increase the Ce concentration. It is shown that these crystals show unequalled good energy resolutions down to 3% for the 662 keV gamma of ¹³⁷Cs, in combination with a high light yield and good timing properties.

4.2 Characteristics

4.2.1 Material

LaCl₃:Ce³⁺ and LaBr₃:Ce³⁺ were grown from LaCl₃/Br₃ and CeCl₃/Br₃ by the Bridgman technique. Starting materials were prepared from La₂O₃ (Heraeus, 99.999%), CeO₂ (Heraeus, 99.999%), NH₄Cl/Br (Merck, reinst), and HCl/Br (Merck, pro-analysis) by the ammonium halide method [7,8]. For both LaCl₃:Ce³⁺ and LaBr₃:Ce³⁺, it is assumed that Ce³⁺ randomly substitutes for La³⁺. This assumption seems reasonable since both ions are trivalent and have similar ionic radii. LaCl₃ and LaBr₃ crystallise in the UCl₃ type structure, space group *P63/m* [9]. Based on structure and lattice parameters, LaCl₃ and LaBr₃ have a calculated density of 3.86 g/cm³ and 5.29 g/cm³, respectively. The lattice is not layered and does not cleave easily. LaCl₃ and LaBr₃ melt at about 859 and 783 °C, respectively. The effective Z for LaCl₃ and LaBr₃ is 49.5 and 46.9, respectively, which is comparable to NaI with respect to high-energy radiation detection efficiency. LaCl₃ and LaBr₃ are hygroscopic like NaI or RbGd₂Br₇, but react differently to moisture and air. LaCl₃ seems to develop a white protective layer on the crystal surface, whereas LaBr₃ is

oxidised within minutes and forms a whitish powder. It is therefore essential that these crystals are sealed into a glass or quartz container to prevent hydration and oxidation of the crystal surface.

4.2.2 Luminescence & Light detection

The luminescence of $\text{LaCl}_3:\text{Ce}^{3+}$ and $\text{LaBr}_3:\text{Ce}^{3+}$ under X-ray and gamma ray excitation is due to the parity allowed (fast) $5d \rightarrow 4f$ transition of Ce^{3+} . The emission maximum is observed at 330 and 358 nm for the chloride and the bromide, respectively. For good scintillator performance, it is important that the emission spectra are well matched to the quantum efficiency curve of the light detector. In general, quantum efficiency is defined as the probability that one photon produces one photoelectron, which is a function of the wavelength. As is shown in Figure 1, the emission spectra of both $\text{LaCl}_3:\text{Ce}^{3+}$ and $\text{LaBr}_3:\text{Ce}^{3+}$ are well matched to the quantum efficiency curves of a UV-photomultiplier tube (PMT) as well as a UV-enhanced large area avalanche photodiode (LAAPD).

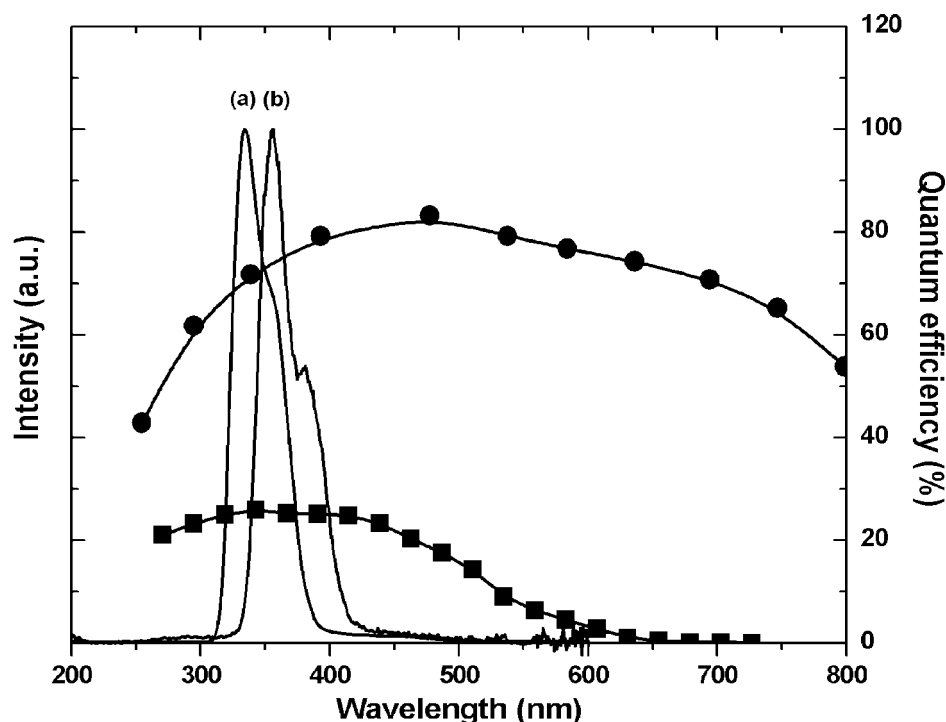


Fig.1 X-ray excited optical luminescence spectra of (a) $\text{LaCl}_3:10\% \text{Ce}^{3+}$ and (b) $\text{LaBr}_3:0.5\% \text{Ce}^{3+}$. The quantum efficiency curves of a Hamamatsu R1791 PMT (■) and an UV-enhanced LAAPD (●) from Advanced Photonix are shown as well.

4.2.3 Light yield & Non-proportional response

Light yields of $\text{LaCl}_3:\text{Ce}^{3+}$ and $\text{LaBr}_3:\text{Ce}^{3+}$ derived from pulse height spectra under ^{137}Cs 662 keV gamma-ray excitation, expressed in photons per megaelectronvolt (MeV) of absorbed gamma-ray energy, are compiled in Table I. All light yields of Table I are obtained with crystals in quartz ampoules.

Table I. Light yields derived from pulse height spectra recorded with different shaping times and the energy resolution R of LaCl_3 and LaBr_3 doped with different Ce concentrations at 662 keV.

Host	[Ce] (%)	Light Yield (10^3 ph/MeV)			Energy resolution R (%)
		0.5 μs	3 μs	10 μs	
LaCl_3	-	-	-	34 ± 1	4.7 ± 0.2
LaCl_3	0.57	17 ± 2	34 ± 4	40 ± 4	7.0 ± 0.5
LaCl_3	2	-	44 ± 4	49 ± 5	3.5 ± 0.1
LaCl_3	4	37 ± 4	47 ± 5	49 ± 5	3.5 ± 0.1
LaCl_3	10	45 ± 5	49 ± 5	49 ± 5	3.3 ± 0.1
LaCl_3	30	42 ± 4	43 ± 5	43 ± 4	3.3 ± 0.1
CeCl_3	-	44 ± 4	46 ± 5	46 ± 5	4.5 ± 0.5
LaBr_3	-	-	-	17 ± 2	14 ± 2
LaBr_3	0.5	61 ± 6	61 ± 6	61 ± 6	2.8 ± 0.2
LaBr_3	2	48 ± 5	48 ± 5	48 ± 5	3.8 ± 0.4
LaBr_3	4	48 ± 5	48 ± 5	48 ± 5	3.5 ± 0.4
LaBr_3	10	45 ± 5	45 ± 5	45 ± 5	3.9 ± 0.4

Figure 2 shows the pulse height spectra of radiation from a ^{55}Fe source, a ^{241}Am source, and a ^{137}Cs source, respectively, obtained with a Hamamatsu R1791 photomultiplier tube (PMT) with a relatively large LaCl_3 :10% Ce^{3+} crystal ($\text{Ø} 8 \times 5 \text{ mm}^2$). Pulse height spectra for a LaBr_3 :0.5% Ce^{3+} ($\text{Ø} 3 \times 3 \text{ mm}^2$) crystal are shown in Figure 3. For LaCl_3 doped with different Ce^{3+} concentrations and pure CeCl_3 , we measured light yields in the order of 34000 to 49000 ph/MeV of absorbed γ -ray energy. A lower absolute light yield for LaCl_3 :10% Ce^{3+} was obtained employing a ^{55}Fe source: 39000 ± 1000 ph/MeV at 6 keV. The absolute light yield of powder samples of pure CeCl_3 has been reported before by S.E. Derenzo et al. [10]. However, they reported a lower light yield of 28,000 ph/MeV under X-ray excitation. The absolute light yield for LaBr_3 :0.5% Ce^{3+} is 61000 ± 5000 photons per MeV of absorbed gamma ray energy at 662 keV. The energy resolution R [full width at half maximum (FWHM) over peak position] of the 662 keV full absorption peak is $3.3 \pm 0.3\%$ and $2.8 \pm 0.1\%$ for LaCl_3 :10% Ce^{3+} and LaBr_3 :0.5% Ce^{3+} , respectively. These energy resolutions are the best ever-reported in literature for scintillator detectors.

When we consider the high light yields of both LaCl_3 : Ce^{3+} and LaBr_3 : Ce^{3+} , it is desirable that they are independent of energy. Deviations, which are known as non-proportionality (or non-linearity) in the scintillation response, may result in difficulties in the determination of the energy and energy resolution of the detected radiation. In principle, non-proportionality can be characterised as a function of either photon or electron energy. While the scintillation response as function of photon energy (photon response) is in general easier to measure and more useful as an indication of scintillator quality to the customer, the scintillation response as function of electron energy (electron response) is more fundamental.

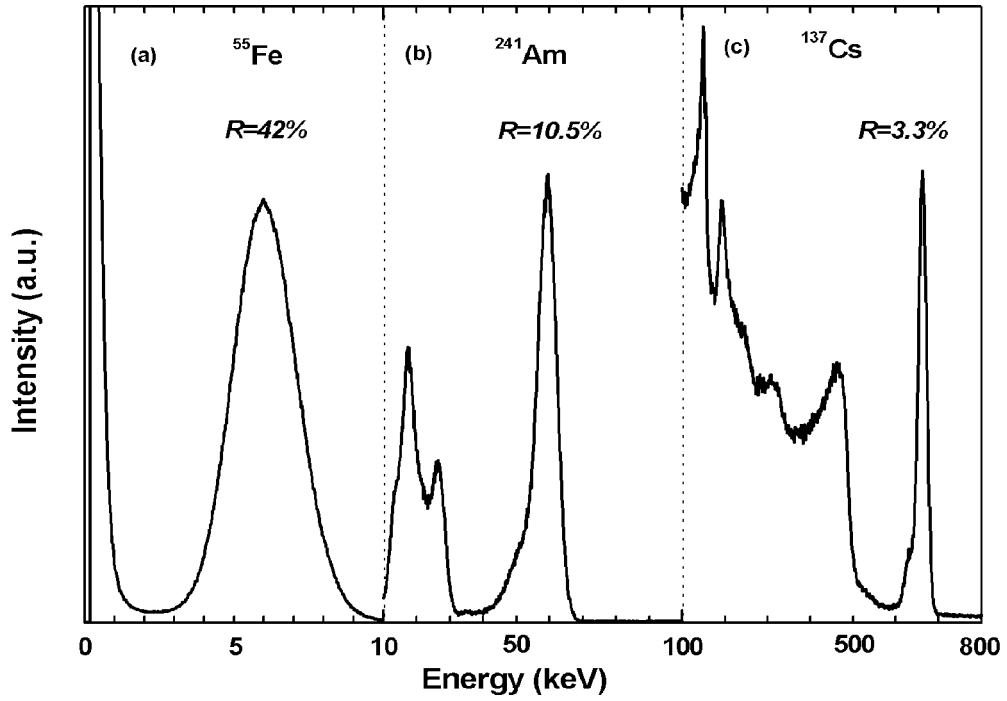


Fig. 2. Energy resolutions obtained with a crystal of $\text{LaCl}_3:10\% \text{Ce}^{3+}$ for X/ γ -rays from (a) ^{55}Fe , (b) ^{241}Am , and (c) ^{137}Cs sources.

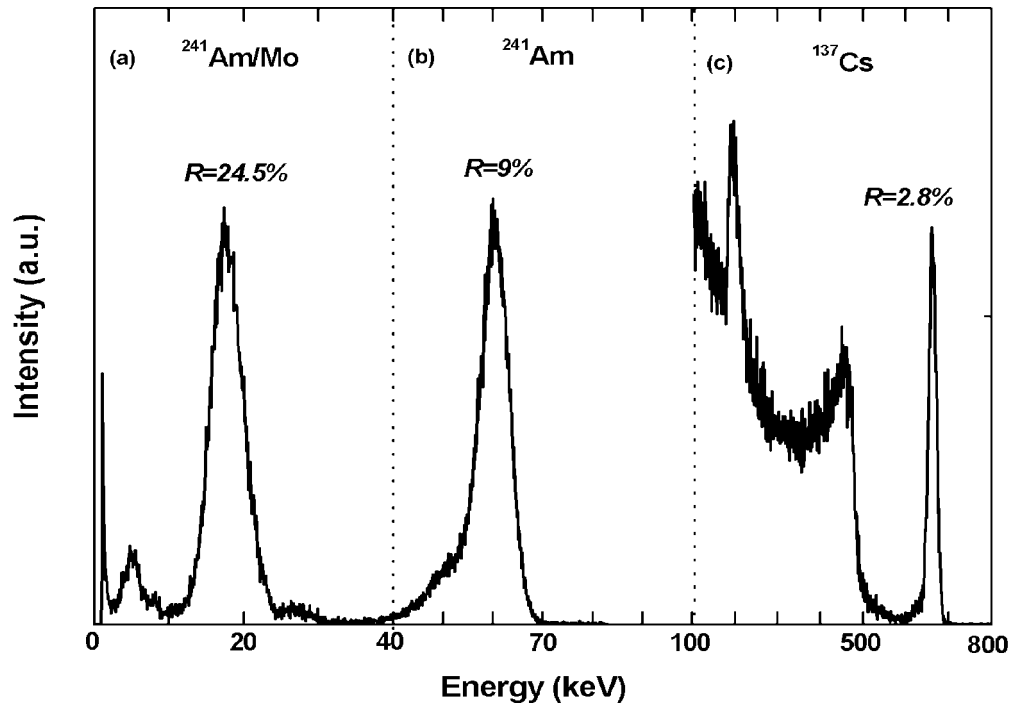


Fig. 3. Energy resolutions obtained with a crystal of $\text{LaBr}_3:0.5\% \text{Ce}^{3+}$ for X/ γ -rays from (a) $^{241}\text{Am/Mo}$, (b) ^{241}Am , and (c) ^{137}Cs sources.

A technique for measuring the electron response of scintillators is the so-called Compton Coincidence Technique (CCT) [11,12]. In short, this method is used to measure the light yield generated in a scintillator when a Compton scattered electron is absorbed. The Compton scattered gamma ray is detected in a secondary detector, such that the energy of the scattered gamma ray and thus the energy of the Compton electron is known. When the scatter angle is varied, the energy of the Compton electron changes as well. Accordingly, the electron response for that particular scintillator is obtained. Next, the measured electron response was used to calculate the photon response. The calculated photon response can then be compared with the measured photon response data.

The electron response of $\text{LaCl}_3:10\% \text{Ce}^{3+}$ is shown in Figure 4. The relative light yield as function of electron energy increases from 7 to 30 keV by about 10%. Above 30 keV, the electron response levels, i.e., it is flat within 5%. Here, relative light yield is defined as the light yield relative to that at 445 keV. Accurate CCT measurements below 7 keV electron energy could not be achieved due to interfering PMT thermal noise.

The calculation of the photon response involves the convolution of the energy distribution of electrons obtained as a result of full-energy gamma-ray absorption events in a scintillator with the measured electron response. The energy distribution of electrons can be defined as $\Psi_{\gamma,e}$ which gives the number of electrons of energy e when the full-energy of a gamma ray of energy γ is deposited in a scintillator. If Monte Carlo simulations are used to determine the energy distribution of electrons, each absorbed gamma in the scintillator will result in one or more electrons with discrete energies. In this case, $\Psi_{\gamma,e}$ will be discrete as well. The discrete energy distribution of electrons $\Psi_{\gamma,i}$ together with the measured electron response $L_{e,i}$ enables the calculation of the photon response by using Monte Carlo simulations according to

$$L_{\gamma} = \frac{1}{N} \sum_{n=1}^N \sum_{i=1}^k \Psi_{\gamma,i} L_{e,i} \quad (1)$$

where k is the number of electron energies that are produced for each full-energy gamma-ray absorption event, where k may vary from event to event. Monte Carlo N Particle Transport Code (MCNP4C) [13] was used to sample the energy distribution of electrons, with N of the order of 10^5 events. All interactions (Compton scatter and photoelectric absorption for $1 \text{ keV} < E_{\gamma} \leq 1000 \text{ keV}$) for each simulated photon were recorded. Since each event is terminated by a photoelectric absorption, a cascade of X-rays and Auger electrons is also produced. The cascade sequence associated with the K, L, and M shells of the lanthanum, and to a lesser degree chlorine, was also simulated with MCNP4C.

The calculated photon response based on (1) requires a knowledge of the electron response at discrete energies ranging from the lowest energy Auger electron from the cascade sequence to the largest photon energy (typically 1 MeV). Consequently, both low and high-energy extrapolations of the measured electron response, as well as a smooth fit of the data are required. These extrapolations are shown in Figure 4 as well. The $\text{LaCl}_3:10\% \text{Ce}^{3+}$ photon response calculated by (1) using the measured electron response is shown in Figure 5. Measured photon response data is shown as well. There is good agreement between the calculated and measured photon response. We estimate that the variation in the light yield is only 2-5% in the range between 20 keV and 1.274 MeV.

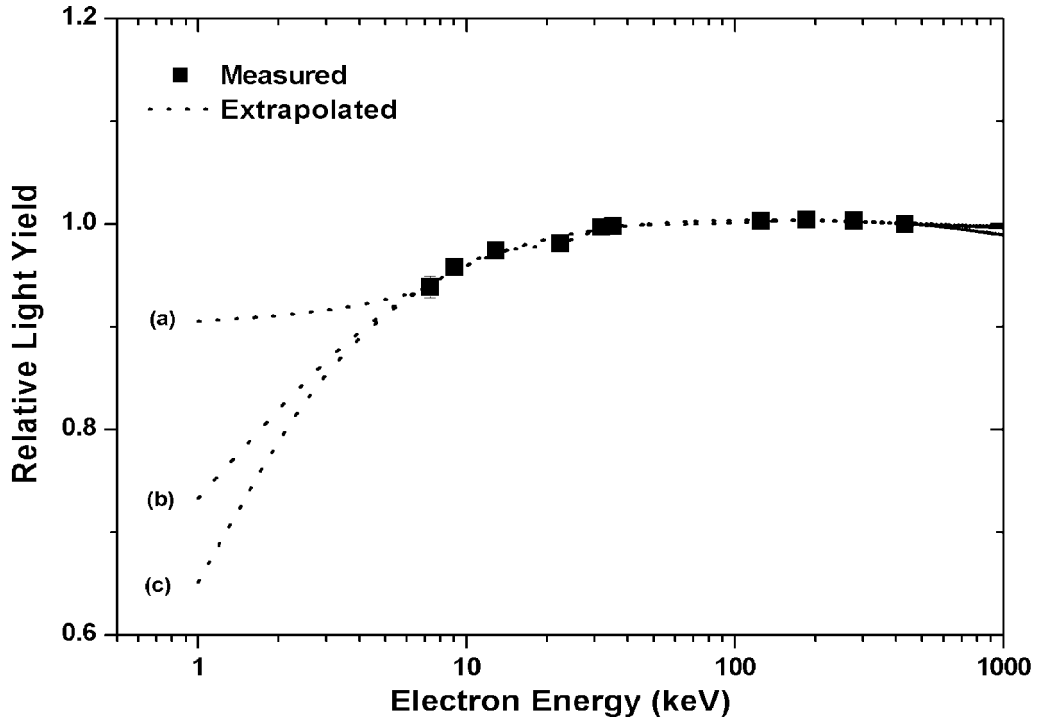


Fig. 4. Electron response of $\text{LaCl}_3:10\% \text{Ce}^{3+}$. The smooth functions are the extrapolated curves of the electron response with relative light yield (a) 0.0, (b) 0.5, and (c) 0.9 at electron energy 0.0 keV.

The general shape of the $\text{LaCl}_3:10\% \text{Ce}^{3+}$ photon response, as seen in Figure 5, is very similar to that of $\text{K}_2\text{LaCl}_5:10\% \text{Ce}^{3+}$ [14]. For $\text{K}_2\text{LaCl}_5:10\% \text{Ce}^{3+}$, the photon response gradually increases by 15 - 20% between 6 keV and 20 keV. Also for $\text{YAlO}_3:\text{Ce}$ a constant light yield response from 14 keV to 1.3 MeV was observed [15]. In contrast, NaI:Tl and CsI:Tl show a light yield response that gradually decreases by 15 to 20% from 50 keV to 1 MeV [16]. Additionally, for NaI:Tl a dip of 10% is observed near the iodine K-shell absorption edge whereas for CsI:Tl a dip of 5% is observed near the K-shell absorption edges of caesium and iodine ions. From 10 to 25 keV, a decrease of 5% and 10% occurs for NaI:Tl and CsI:Tl , respectively.

The intensity of the calculated photon response at the K edge of La (38 keV) appears to depend critically on the behaviour of the electron response below 10 keV. If the electron response levels at a relative light yield of 0.9 at $E_e = 0$ keV (a), the calculated photon response dips by about 3% between 30 keV to 40 keV. However, if the electron response levels at a relative light yield of 0.5 at $E_e = 0$ keV (b), the calculated photon response dips by about 7% between 30 keV to 40 keV. And if the electron response monotonically decreases to zero at electron energy $E_e = 0$ keV (c), the calculated photon response dips by about 12% between 30 keV to 40 keV. Apparently, the contribution of (low energy) Auger electrons to the calculated photon response is significant, especially near the K edge. At 40 keV (just above the K edge of La) electrons are produced that have a relatively low energy, i.e., $E_e < 10$ keV, whereas for γ -ray energies below the lanthanum K edge at 38 keV and above 50 keV, electrons are produced that have a relatively high energy, i.e., $E_e > 10$ keV. The measured photon response of $\text{LaBr}_3:0.5\% \text{Ce}^{3+}$ is very similar to that of $\text{LaCl}_3:10\% \text{Ce}^{3+}$. However, it has only been measured in the energy region between 20 keV and 1.3 MeV and is not shown in this thesis.

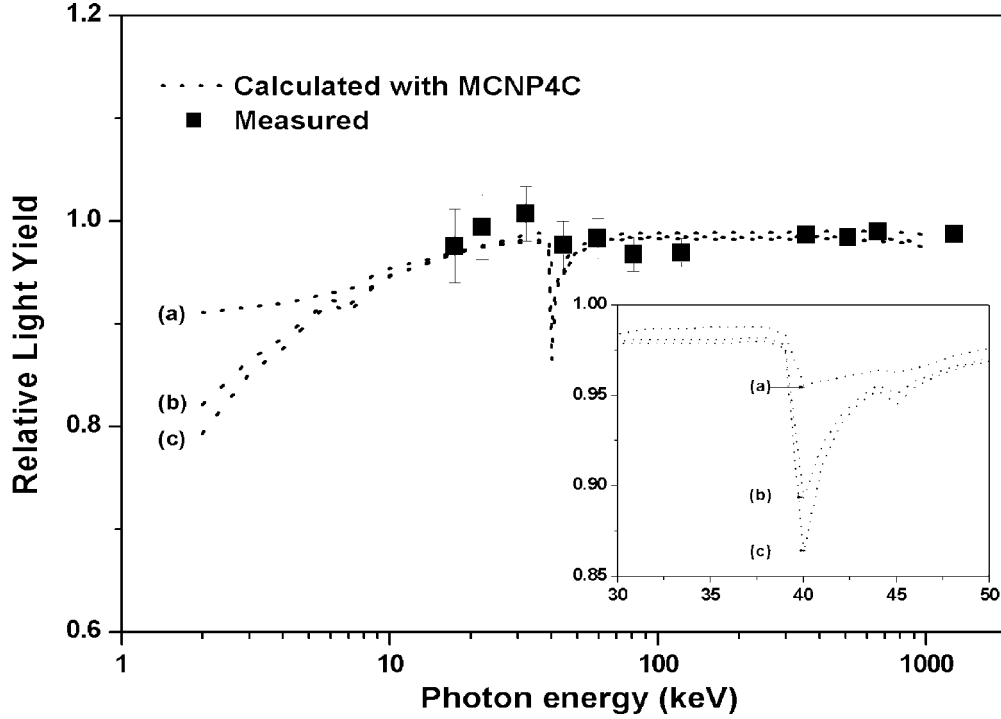


Fig. 5. Photon response of $\text{LaCl}_3:10\% \text{Ce}^{3+}$. The dotted curves are the calculated photon responses according to the electron response with relative light yield (a) 0.0, (b) 0.5, and (c) 0.9 at electron energy 0.0 keV. The inset shows part of the calculated photon responses, between 30 and 50 keV, on a linear energy scale.

4.2.4 Energy resolution

To determine the energy resolution, the photopeaks have been fitted by Gaussian curves. The photopeak obtained with a ^{137}Cs source is accompanied by a satellite peak at lower energy, due to escape of characteristic K X-rays of lanthanum. With the Hamamatsu R1791 PMT, an energy resolution R of $3.3 \pm 0.1\%$ (FWHM over peak position) for the 662 keV full energy peak has been observed for the $\text{LaCl}_3:10\% \text{Ce}^{3+}$ compound. For other Ce concentrations, the energy resolution at 662 keV does not change significantly. Only for pure LaCl_3 the energy resolution is worse, $4.7 \pm 0.2\%$ at 662 keV. The sample doped with 0.57% Ce^{3+} shows an even worse resolution. However, this is probably due to the quality of the crystal. To our knowledge, energy resolutions of $\sim 3\%$ have never been achieved with any other scintillator detector before. The $\sim 3\%$ values are considerably better than those of 4.1% [17] and 5.6% [18] of $\text{RbGd}_2\text{Br}_7:9.8\% \text{Ce}^{3+}$ and NaI:Tl , respectively.

Equally good energy resolutions are observed for $\text{LaBr}_3:\text{Ce}^{3+}$. Especially for the 0.5% Ce^{3+} doped compound, a world record energy resolution of $2.8 \pm 0.2\%$ at 662 keV has been obtained with a relatively small single crystal ($\text{Ø } 3 \times 3 \text{ mm}^2$). Usually, five separate contributions to R are distinguished according to [14]

$$R^2 = R_{np}^2 + R_{inh}^2 + R_p^2 + R_M^2 \quad (2)$$

Where R_{np} is the contribution of the non-proportional response of the scintillator, R_{inh} is connected with inhomogeneities in the scintillation crystal, which cause local fluctuations in the scintillation light yield. The transfer resolution, R_p is connected to fluctuations in the transfer efficiency, which results in the arrival of a photoelectron at

the first dynode and subsequently undergoes the full multiplication in the PMT. R_M is the photomultiplier resolution [14,19]. The photomultiplier resolution R_M is dependent on the number of photoelectrons emitted by the photocathode of the PMT. It is defined as

$$R_M = 2.35 \sqrt{\frac{1 + \nu(M)}{N_{phe}}} \quad (3)$$

where $\nu(M)$ is the variance in the PMT gain and N_{phe} the number of photoelectrons. Since the number of photoelectrons is proportional to the number of photons produced in the scintillator, an inverse square root dependence of R_M on the energy of the gamma-ray absorbed in the scintillator is expected.

The combined effect of R_{np} , R_{inh} , and R_p is often called the scintillator resolution, R_S . For an ideal scintillator, the three R_{np} , R_{inh} , and R_p resolutions vanish and $R = R_M$. Figure 6 shows the energy resolution as function of photon energy between 17.4 keV and 1.274 MeV for both a relatively large scintillation crystal ($\text{\O} 16 \times 19 \text{ mm}^2$) and a relatively small scintillation crystal ($\text{\O} 3 \times 5 \text{ mm}^2$) of $\text{LaCl}_3:10\% \text{ Ce}^{3+}$. Also shown are the PMT resolution calculated from the number of photoelectrons and the scintillator resolution of the crystals.

In Figure 6 the energy resolution as function of photon energy of $\text{LaCl}_3:\text{Ce}^{3+}$ is shown. To compare, the scintillator resolution as function of photon energy for a NaI:Tl crystal ($\text{\O} 1 \times 1 \text{ cm}^2$) is shown as well (dotted trace). When the gamma-ray energy decreases, the energy resolution R increases and becomes much larger - in absolute terms - than one would expect on basis of the variation in the number of detected photoelectrons. In other words, the energy resolution R increases much more than the photomultiplier resolution R_M does. This is most apparent for the larger ($\text{\O} 16 \times 19 \text{ mm}^2$) crystal of $\text{LaCl}_3:10\% \text{ Ce}^{3+}$. Interestingly, this crystal exhibits an almost linear relationship between resolution and the inverse square root of the energy and the observed energy resolution is mainly due to the scintillator resolution. For the smaller crystal ($\text{\O} 3 \times 5 \text{ mm}^2$), it is just the opposite way. Here, the photomultiplier resolution is dominant. The scintillator resolution as function of photon energy for NaI:Tl exhibits a step like curve with a bell-shaped contour in the energy range between 100 keV and 1 MeV, measured by Moszynski *et. al.* [20]. For the smaller crystal of $\text{LaCl}_3:10\% \text{ Ce}^{3+}$ a similar shape is observed for the scintillator resolution as function of photon energy.

Apparently, the contribution of R_S increases with the size of the crystal and increases when the gamma-ray energy decreases. What is the origin of this scintillator resolution? First, the crystal volumes differ by a factor of 100 and thus the contribution of multiple Compton scattering to the energy resolution is more significant in the larger crystal. This could explain the relatively large R_S for the larger crystal at energies above 100 keV. Since we observed a rather proportional response for both crystals between 40 keV and 1.274 MeV, the contribution of R_{np} to the scintillator resolution is probably negligible in this energy region. Nevertheless, the scattering of electrons produced by γ -rays, commonly referred to as δ -rays, may result in some spreading of the energy resolution for energies lower than 40 keV.

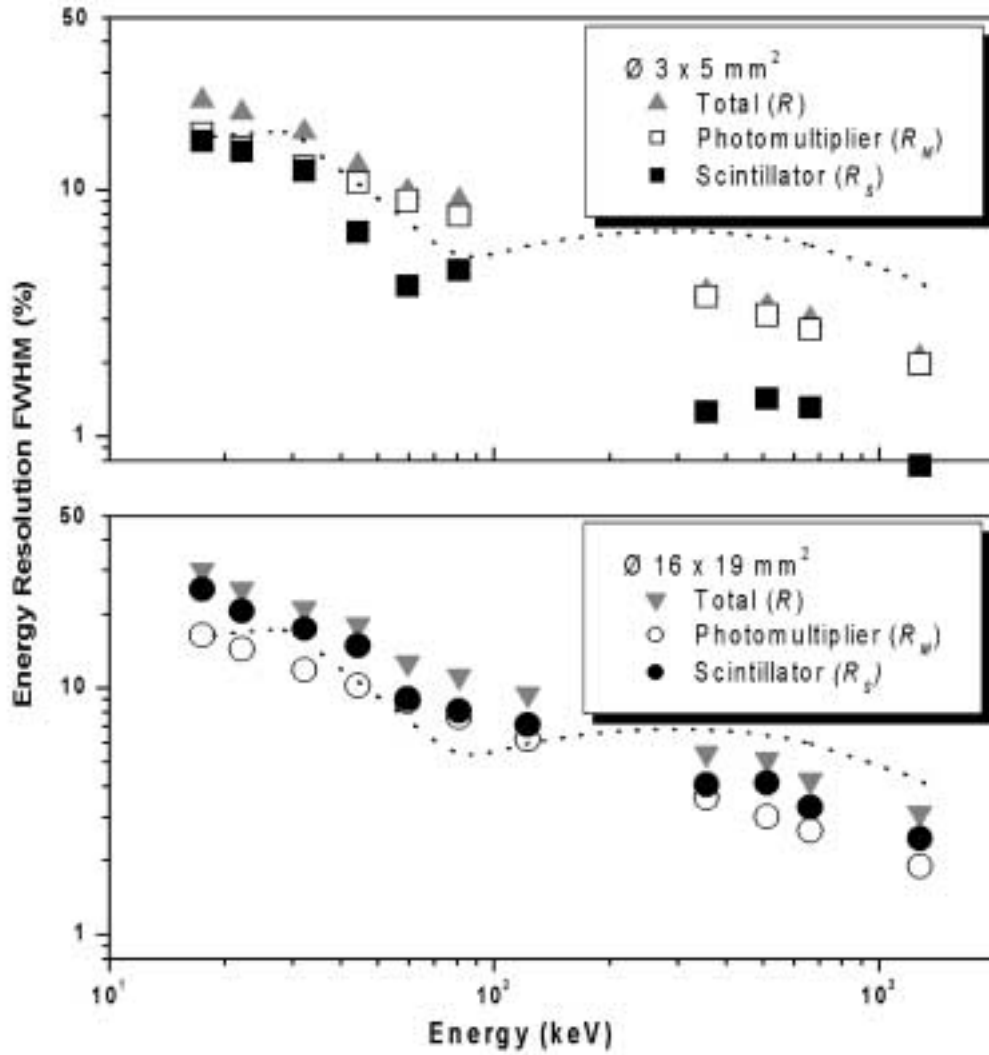


Fig. 6. Energy resolution as function of photon energy of $\text{LaCl}_3:10\% \text{ Ce}^{3+}$. The dotted curve shows the scintillator resolution as function of photon energy for a $\text{Ø } 1 \times 1 \text{ cm}^2$ crystal of NaI(Tl) [18].

According to Iredale [21], δ -rays of energy $>1 \text{ keV}$ add approximately 3.2% to the energy resolution of NaI:Tl for 0.66 MeV electrons. For $\text{LaCl}_3:10\% \text{ Ce}^{3+}$, we found that on average, 10% of the total energy deposited by electrons is dissipated by δ -rays with mean energy 1 keV. This value was obtained by summation of the energy transferred to δ -rays during electron transport simulations in the scintillator using GEANT 4. [22]. Since the contribution of δ -rays to the total energy resolution may vary with electron energy, we expect that R_{np} significantly contributes to the scintillator resolution, especially at lower energies. A larger R_S for $E_\gamma < 662 \text{ keV}$ may also be due to an increase in R_{inh} . For a 662 keV photon, the absorption length in LaCl_3 is 3.4 cm. For this energy, the gamma rays are uniformly absorbed in the crystal. For lower energies, the absorption length is considerably shorter: at 60 keV, 0.49 mm, and at 17.4 keV, 0.084 mm. These low energy photons are only absorbed in the surface layer of the crystal. If the scintillation or the light collection properties at the surface are somewhat different from the bulk, it will result in a worse energy resolution and R_{inh} increases.

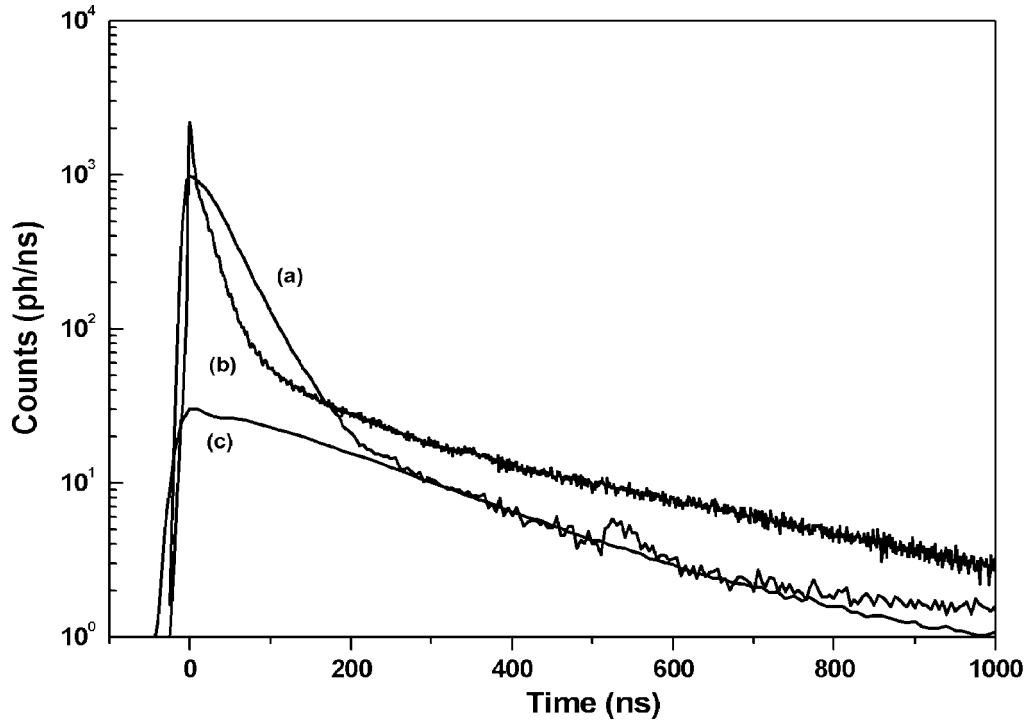


Fig. 7. Decay curves of (a) $\text{LaBr}_3:0.5\% \text{Ce}^{3+}$, (b) $\text{LaCl}_3:10\% \text{Ce}^{3+}$, and (c) NaI(Tl) .

4.2.5. Time information

The scintillation decay curves of $\text{LaCl}_3:10\% \text{Ce}^{3+}$ and $\text{LaBr}_3:0.5\% \text{Ce}^{3+}$ are shown in Figure 7. For comparison, the scintillation decay curve of NaI:Tl is shown as well. The curves have been normalised such that the time integral equals the absolute light yield as found from pulse height spectra recorded with a shaping time of $10 \mu\text{s}$.

In order to analyse these curves, a simple exponential decay function was used. $\text{LaCl}_3:10\% \text{Ce}^{3+}$ has as short decay component of $26 \pm 1 \text{ ns}$ which represents 41% of the total light yield. A relatively long decay component of $\sim 210 \text{ ns}$ accounts for 30%. The decay time of $\text{LaBr}_3:0.5\% \text{Ce}^{3+}$ is $35 \pm 1 \text{ ns}$, representing over 90% of the total light yield.

Time resolution spectra of $\text{LaCl}_3:10\% \text{Ce}^{3+}$ ($\text{Ø } 3 \times 5 \text{ mm}^2$) and $\text{LaBr}_3:0.5\% \text{Ce}^{3+}$ ($\text{Ø } 2 \times 5 \text{ mm}^2$) using XP2020Q PMTs, a ^{60}Co source and constant-fraction discrimination with a threshold set at $E \geq 800 \text{ keV}$ are depicted in Figure 8. The measured time resolutions (FWHM) are 224 ± 2 and $387 \pm 4 \text{ ps}$ for $\text{LaCl}_3:10\% \text{Ce}^{3+}$ and $\text{LaBr}_3:0.5\% \text{Ce}^{3+}$, respectively. These represent the combined time resolutions of the crystal under study against a reference crystal of BaF_2 ($\text{Ø } 2.5 \times 0.8 \text{ cm}^2$).

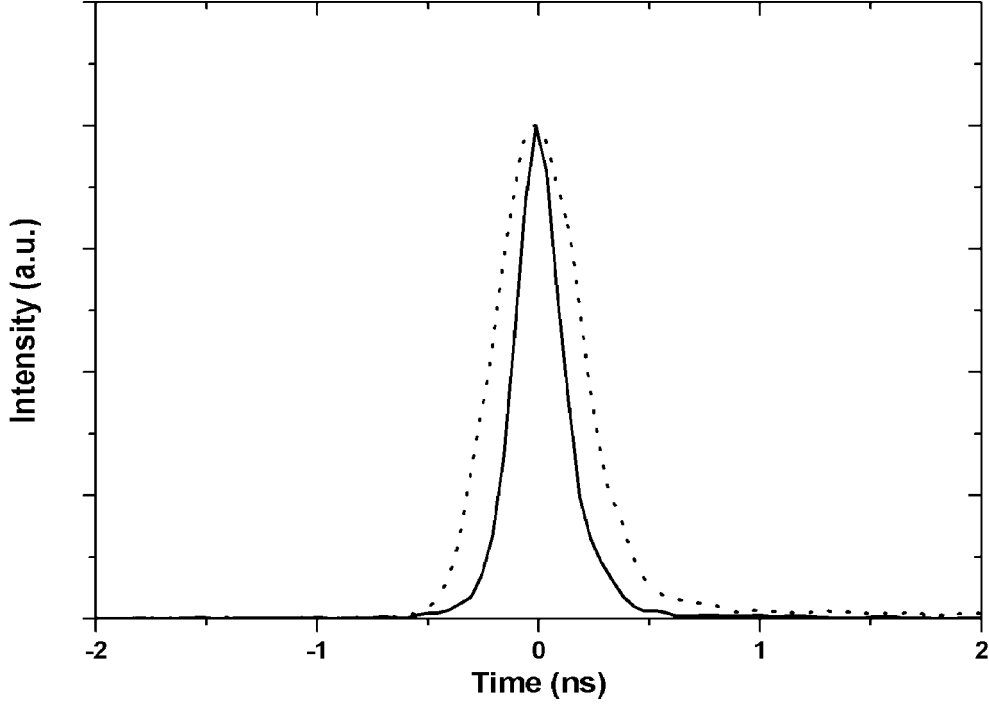


Fig. 8. Comparison of the time resolution spectra measured with $\text{LaCl}_3:10\% \text{Ce}^{3+}$ (solid trace) and $\text{LaBr}_3:0.5\% \text{Ce}^{3+}$ (dotted trace) against BaF_2 crystals for ^{60}Co γ -rays and an energy threshold set at $E \geq 800$ keV.

4.3 Conclusions

If we compare the scintillation properties of $\text{LaCl}_3:\text{Ce}^{3+}$ and $\text{LaBr}_3:\text{Ce}^{3+}$ with those of NaI:Tl and CsI:Tl , $\text{LaCl}_3:\text{Ce}^{3+}$ and $\text{LaBr}_3:\text{Ce}^{3+}$ show a much better energy resolution and a much faster response, see Table II. Although hygroscopic, both $\text{LaCl}_3:\text{Ce}^{3+}$ and $\text{LaBr}_3:\text{Ce}^{3+}$ are relatively easy to grow and crystals are commercially being developed. For applications where a good energy resolution is required in combination with fast scintillation, both $\text{LaCl}_3:\text{Ce}^{3+}$ and $\text{LaBr}_3:\text{Ce}^{3+}$ will be very good choice. These materials may become of interest for scintigraphy and SPECT and even for PET. Because the density and effective Z of LaBr_3 are higher than those of LaCl_3 , $\text{LaBr}_3:\text{Ce}^{3+}$ will eventually become the scintillator of choice in the near future, if it can be easily grown into large single crystals.

Table II. Scintillation properties of $\text{LaCl}_3:10\% \text{Ce}^{3+}$, $\text{LaBr}_3:0.5\% \text{Ce}^{3+}$, NaI:Tl , and CsI:Tl . Z_{eff} is the effective Z of the host.

Host	Dopant	Emission (nm)	Density (g/cm^3)	ρZ_{eff}^4	Light yield (ph/MeV)	Decay (ns)	Energy resolution (@ 662 keV)	Time resolution (ps)
LaCl_3	Ce	330	3.86	23.2	49000	26 (41%)	3.3	224
LaBr_3	Ce	358	5.29	25.6	61000	35 (90%)	2.8	387
NaI	Tl	415	3.67	24.4	40000	230	~ 6	-
CsI	Tl	560	4.51	38.3	59800	$\sim 10^3$	~ 6	-

References

- ¹ R. Hofstadter, Phys. Rev. 74 (1948) 100.
- ² R. Hofstadter, Phys. Rev. 75 (1948) 796.
- ³ R. Hofstadter, Nucleonics 6 (1950) 70.
- ⁴ P. Brinckman, Phys. Lett. 15 (1965) 305.
- ⁵ D.W. Aitken, B.L. Beron, G. Yenicay, H.R. Zulliger, IEEE Trans. Nucl. Sci. NS-14 (1967) 468.
- ⁶ O. Guillot-Noël, J.T.M. de Haas, P. Dorenbos, C.W.E. van Eijk, K. Krämer, H.U. Güdel, J. Lumin. 85 (1999) 21.
- ⁷ J.B. Reed, B.S. Hopkins, L.F. Audrieth, Inorg. Synth. 1 (1936) 28.
- ⁸ G. Meyer, Inorg. Synth. 25 (1989) 146.
- ⁹ B. Morosin, J. Chem. Phys. 49 (1968) 3007.
- ¹⁰ S. E. Derenzo, W.W. Moses, "Experimental efforts and results in finding new heavy scintillators," in Proc. Cristal 2000 Int. Workshop, CRYSTAL 2000, Editions Frontieres, Gif-sur-Yvette, France, 1993, p. 125.
- ¹¹ J.D. Valentine, B.D. Rooney, Nucl. Instr. Meth. Phys. Res. A 353 (1994) 37.
- ¹² B.D. Rooney, J.D. Valentine, IEEE Trans. Nucl. Sci. 43 (1996) 1271.
- ¹³ MCNP-A General Monte Carlo N Particle Transport Code, CCC-0700, Version 4C.
- ¹⁴ P. Dorenbos, J.T.M. de Haas, C.W.E. van Eijk, IEEE Trans. Nucl. Sci. 42 (1995) 2190.
- ¹⁵ M. Kapusta, M. Balcerzyk, M. Moszynski, J. Pawelke, Nucl. Instr. Meth. Phys. Res. A 421 (1999) 610.
- ¹⁶ D.W. Aitken, B.L. Beron, G. Yenicay, H.R. Zulliger, IEEE Trans. Nucl. Sci. NS-14 (1967) 468.
- ¹⁷ O. Guillot-Noël, J.C. van't Spijker, J.T.M. de Haas, P. Dorenbos, C.W.E. van Eijk, K.W. Krämer, H.U. Güdel, IEEE Trans. Nucl. Sci. 46 (1999) 1274.
- ¹⁸ D.E. Persyk, T.E. Moi, IEEE Trans. Nucl. Sci. 25 (1978) 615.
- ¹⁹ J.B. Birks, "The Theory and Practice of Scintillation Counting," Pergamon, New York, 1967.
- ²⁰ M. Moszynski, J. Zalipska, M. Balcerzyk, M. Kapusta, W. Mengesha, J.D. Valentine, Nucl. Instr. Meth. Phys. Res. A 484 (2002) 259.
- ²¹ P. Iredale, Nucl. Instr. Meth. 11 (1961) 340.
- ²² GEANT 4, Detector description and simulation tool, Application Software Group, Computing and Networks Division, CERN, Geneva, Switzerland (available from <http://www.cern.ch>).

Part B

SCINTILLATION MECHANISM

5. Scintillation

5.1. Introduction

Since the discovery of NaI:Tl by Hofstadter [1,2] significant progress has been made in the research and development of inorganic scintillators for the detection of ionising radiation. Basically, two different directions have been pursued during the five decades of scintillators research:

- (1) the search and development of new inorganic scintillators and
- (2) the optimisation of scintillators for specific applications, like PbWO₄ [3,4] BGO [5,6], NaI:Tl [7,8], and CsI:Tl [7-11].

In both fields, attention was focused on the characterisation of the scintillation properties. Relatively few studies present a more detailed investigation of the scintillation mechanism [12-17]. Nevertheless, many inorganic materials were found to be efficient scintillators with a high light yield and good energy resolution. Unfortunately, the question why these materials showed such excellent scintillation properties remained open, due to the lack of in-depth knowledge about the scintillation mechanism.

In this chapter, a general introduction to scintillation is given. The process that leads to the formation of electrons and holes and, in particular, the scintillation mechanism is discussed. In the next four chapters, the scintillation mechanism is described in detail for four different types of compounds. It is discussed for LaCl₃:Ce³⁺ and LaBr₃:Ce³⁺ in Chapter 6. The elpasolites with structural formula Cs₂LiYX₆:Ce³⁺ ($X = \text{Cl, Br}$) are treated in Chapter 7, the properties and mechanism of the lutetium halides, LuX₃:Ce³⁺ ($X = \text{Cl, Br}$) are discussed in Chapter 8, and Chapter 9 deals with the ternary halides K₂LaX₅:Ce³⁺ ($X = \text{Cl, Br, I}$). Finally, in chapter 10 the main conclusions addressing the scintillation mechanism are summarised and the predictability of scintillation properties and the scintillation mechanism of unknown compounds is addressed.

5.2. The scintillation process

When an inorganic crystal is subjected to radiation, numerous changes can occur in both the indigenous lattice ions as well as in the impurities present. In general, the interaction of electromagnetic radiation with matter proceeds by complete or partial absorption of the quantum which may lead to electronic excitations or ionic defects. Both may in turn lead to the formation of electrons and holes which can transfer their energy to a luminescent centre.

Here we define the *scintillation process* as the consecutive stages of

- (a) the interaction of radiation with matter, multiplication, relaxation and thermalisation of the resulting electrons and holes,
- (b) the formation of excitonic states and energy transport to luminescent centres, and
- (c) luminescence.

In contrast, the *scintillation mechanism* is the method by which the energy is transferred by the electrons and holes to the luminescent centre. Various models have been used to describe each of these three stages of the scintillation process, but only for (a) and (c) are workable theoretical models available. Nevertheless, different models of energy transfer have been presented in the past, based on the assumption that energy transfer was dependent on energy carrier density and electron stopping power [12,13]. Both are material specific properties that can be simulated using dedicated Monte Carlo codes.

5.2.1. Interaction of Radiation with Matter

The initial step in the scintillation process is the absorption of energy from the radiation field. This absorption occurs somewhat differently for various types of radiation, i.e. electrons, alpha particles, neutrons or electromagnetic radiation. In the interaction of electromagnetic radiation with matter, a quantum is completely or partially absorbed. The most important absorption processes in the case of absorption of electromagnetic radiation, particularly prominent at relatively low (< 10 MeV) energies are [18]

- (a) the photoelectric effect,
- (b) Compton scattering, and
- (c) pair production.

In *photoelectric effect*, the full photon energy is transferred to bound electrons of the atom (mostly *K*- or *L*-shell electrons). The cross section, κ , per atom for absorption of a photon is given by:

$$\kappa \sim \frac{Z^n}{E^{3.5}} \quad (1)$$

where n varies between 4 and 5. Consequently, absorption of a photon is most efficient for high- Z materials and low-energy photons. Energy transfer increases in efficiency as the photon energy decreases until the energy becomes too small to excite *K*-shell electrons. At that point, there is a sudden drop in efficiency. At even lower energies, the *L*- or *M*-shell electrons can no longer be ionised, so that a graph of efficiency versus energy has a sawtooth character in the keV energy region.

For photon energies larger than approximately 100 keV, a second mechanism of interaction of electromagnetic radiation with matter becomes important. This is the “Compton effect,” in which a photon partially transfers its energy to a weakly bound electron. The total cross section for Compton scattering varies much more slowly with energy than does that for the photoelectric effect. Since Compton scattering is proportional to the number of electrons, it varies as Z/E . At energies above 1.02 MeV, “pair production” becomes important and electron-positron pairs are produced with increasing efficiency as the energy rises. The absorption cross section, τ , per atom is proportional to

$$\tau \sim Z^2 \ln\left(\frac{2E}{m_0 c^2}\right) \quad (2)$$

where $m_0 c^2$ is the rest-mass energy of an electron (0.511 MeV). The absorption cross section for electromagnetic radiation of a compound that is comprised of different atoms with different Z , is determined by the cross sections mentioned above and the number of atoms per unit volume. However, the variation in the absorption cross section for electromagnetic radiation among materials that are constituted of different atoms is such that an easy comparison based on Z_i (atom number of the i^{th} element in the matrix) is not feasible. In order to be able to compare the attenuation of electromagnetic radiation by different materials, the so-called *effective Z* has been introduced. It is defined as [19]

$$Z_{\text{eff}} = \sqrt[x]{\sum_i w_i Z_i^x} \quad (3)$$

where w_i is the fraction by weight of element i with atomic number Z in the chemical formula, and x a value between 3 and 4. Equation (3) is only valid in the energy region where photoelectric effect is dominant and one has to realise that at energies between 100 keV and 1 MeV the absorption cross section contains contributions of both Compton scattering and photoelectric absorption.

The use of Z_{eff} to characterise the absorption cross sections in an extended energy range is in most cases unsatisfactory. However, Z_{eff} is a useful parameter to compare different materials over a certain limited energy range.

5.2.2 Multiplication, relaxation and thermalisation

After energy has been absorbed in a crystal, it is present in the form of energetic electrons of several keV energy in a normally empty conduction band and holes in the normally empty valence band. The hot electrons lose their energy by collisions with other electrons in the material, generating secondary electrons and holes. This avalanche of secondaries continues until the energy of the electrons is no longer sufficient to further ionise the material. The excess energy is then lost by thermalisation and optical phonon excitation. The time scale for these processes is believed to be of the order of 1 ps. Various physical models have been used for the description of these complicated processes of energy dissipation: simple phenomenological [20,21], “crazy-carpentry” [22], plasmon [23], and polaron [24].

These models consider only a single mechanism and do not take into account the whole variety of processes taking place. A detailed review of these theories was given by Rodnyi *et al.* [14]. As a rule of thumb, the energy needed to create an electron-hole pair after absorption of radiation is about 2 – 3 times the bandgap energy for materials having a relatively small valence bandwidth compared to the energy of the forbidden bandgap.

5.3. Defects

The second step in the scintillation process is the formation of defects and subsequently, the energy transport to luminescent centres.

The primary defects produced by radiation in materials with mainly ionic bonding, i.e. the alkali halides, are Frenkel defects. These Frenkel defects consist of electrons and holes that may be trapped at impurities or in the perfect lattice. Since the crystal as a whole must remain electrically neutral, free electron and holes are always created in pairs and for every electron trapping centre formed, there must also be a corresponding hole centre formed.

5.3.1 Electrons

When an electron is excited to the conduction band of a perfect ionic crystal, it may be energetically favourable to move in a spatially localised level, accompanied by a local deformation in the previously perfect ionic arrangement. The interaction between the electron and the lattice is dynamical and serves to reduce the electrostatic energy of the system. The electron plus induced lattice polarisation is called a polaron. Such an entity happens to be very mobile and is generally not viewed as a defect.

However, if the electron is bound to a negative ion vacancy, it may be stabilised long enough to be detected experimentally. Such an electron centre is often called an F centre, which is an abbreviation for the German word *Farbzentrum* (colour centre). The F centre has a number of electronic states, and optical absorption produces a transition of the electron from the ground state to the excited states. Its paramagnetic nature makes it a model system for electron paramagnetic resonance (EPR) studies. Figure 1 shows a schematic of the F centre.

If the F centre is located next to an impurity that has replaced an indigenous cation, the composite defect is called an F_A centre. For example, small concentration of Na^+ or Li^+ may be introduced into KCl and the F centres formed with these ions nearby are F_{Na} and F_{Li} centres, respectively. Other types of F centres include the F^- centre which consists of a negative ion vacancy that has trapped two electrons, whereas the F^+ centre is a double-negative ion, e.g. O^{2-} , vacancy that has trapped just one electron. In general, the designation F^- or F^+ is reserved for negative ion vacancies that have trapped a certain number of electrons, such that the ionic charge of the defect with respect to the perfect lattice is negative or positive, respectively.

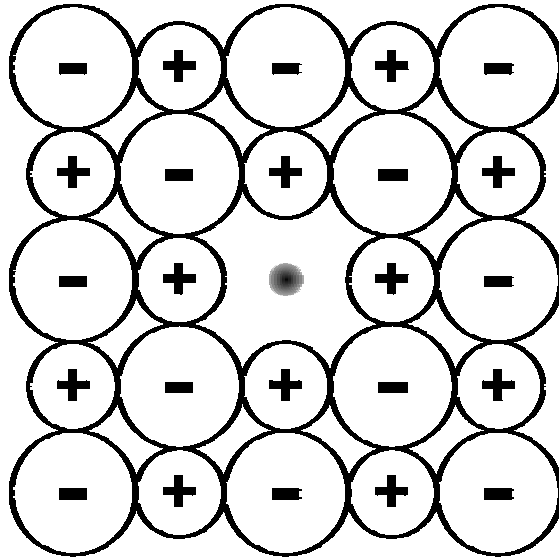


Fig.1. Schematic of the F centre. The missing anion in the centre is replaced by an electron.

5.3.2. Holes

In contrast to electrons that can move freely in ionic crystals once they are ionised into the conduction band, holes are trapped at low temperatures in the perfect crystal and are observed to move only at higher temperatures by a diffusion like hopping from one lattice position to the next. Since the energy necessary to localise a hole, approximately half the width of the valence band, is much less than the energy gained from polarisation, lattice relaxation, and X_2^- binding [25], self-trapping of holes is likely to occur. When self-trapped, the hole is localised on a halide ion X^- , forming an X^0 atom like defect. After polarisation and relaxation of the lattice, it binds a neighbouring halide ion, forming a X_2^- molecular like complex. Such a centre is called a V_K centre.

A similar hole centre, the H centre results from an interstitial halide ion being bound to a lattice ion by a hole; i.e. the singly ionised halide molecule X_2^- is forced to occupy a negative ion site. Therefore, the net charge of the defect with respect to the perfect lattice is zero. This is in marked contrast with the V_K centre which bears a net positive charge. The V_K and H centres are depicted schematically in Figure 2.

5.3.3 Excitons

A third class of defects are the excitons. These are carriers of electronic excitation energy in ionic crystals and may be regarded as a correlated electron-hole pair. Like the hole, the exciton may become self-trapped in the ionic crystal. In principle, one could distinguish two different types of self-trapped excitons (STEs):

- (a) the *on-centre* STE, i.e. a self-trapped hole with the electron in a *de-localised* orbit around the hole ($V_K + e^-$), and
- (b) the *off-centre* STE, i.e. a nearest-neighbour F – H pair where the electron is *localised* at a nearest neighbour anion vacancy.

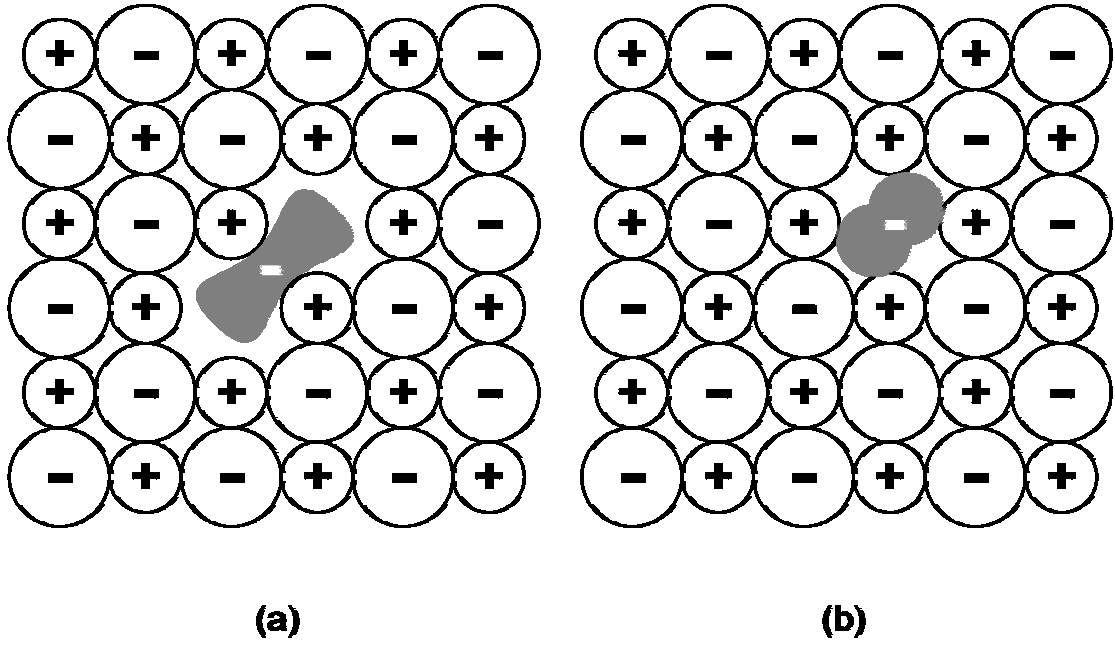


Fig.2. Schematic of the (a) V_K and (b) H centre.

In principle, the V_K core is repulsive to an excited electron due to its negative pseudopotential and the formation of an STE is solely due to the lattice relaxation around the V_K centre [26]. The energy of the excited electron can be significantly lowered if the excited electron occupies an anion vacancy (F centre). If the lattice allows for a suitable distortion, the electron will expel the V_K centre. Subsequently, the V_K centre may transform into a H centre where the anion vacancy formed is taken over by the electron which becomes a F centre. Thus, a nearest neighbour $F - H$ pair is formed. Figure 3 shows the STE as ($V_K + e^-$) and nearest neighbour $F - H$ pair schematically.

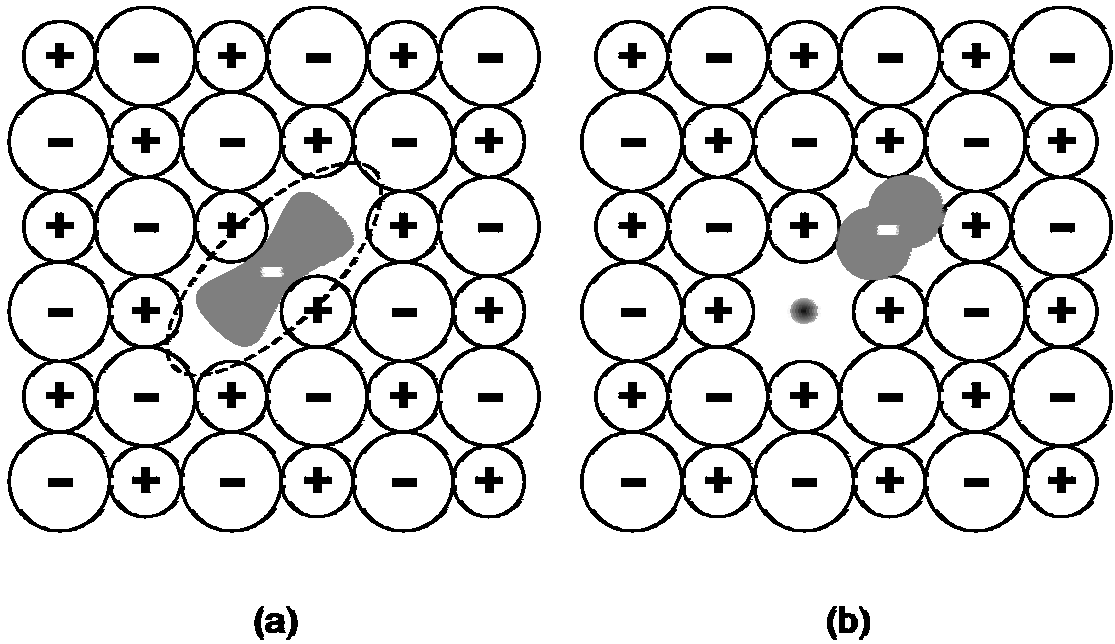


Fig. 3. Schematic of the STE as (a) $V_K + e^-$ and (b) nearest neighbour $F - H$ pair.

When the electron and hole components of the STE recombine, STE luminescence is observed. These luminescence bands are either σ - or π -polarised. The σ -polarised bands have a short lifetime of the order of 10^{-9} s and are due to dipole –and spin-allowed transitions to the $^1\Sigma_g$ ground state of the STE. In many cases the σ -polarised bands are observed only at liquid helium temperatures. The π -polarised bands have a lifetime of the order of $10^{-3} - 10^{-6}$ s and arise from a transition from a $^3\Pi$ excited state to the $^1\Sigma_g$ ground state of the STE. For the alkali halides, these normally strictly spin-forbidden transitions are relaxed by the halogen spin-orbit interaction of the “ V_K core” of the STE. Since the spin-orbit interaction increases as the halogen atom becomes heavier [27], a basic trend of shorter STE lifetimes in crystals with heavier halogen constituents is expected.

5.4. Energy transport

The different types of defects may either transfer their energy to luminescent centres, recombine radiatively or non-radiatively. In the following discussion, we distinguish two categories of inorganic scintillators as a matter of convenience: intrinsically pure inorganic scintillators, like BaF₂ and BGO, and impurity-activated inorganic scintillators, like NaI:Tl, CsI:Tl and LaCl₃:Ce³⁺.

Since our objective is to discuss the *scintillation mechanism*, our focus will be on impurity-activated inorganic scintillators, in particular on Ce³⁺-activated materials. In general we can define three different energy transport mechanisms, i.e. *scintillation mechanisms*, which occur at different time scales and with different probabilities:

- (a) energy transfer by direct electron-hole capture,
- (b) energy transfer by binary electron-hole diffusion, and
- (c) energy transfer by STE diffusion.

5.4.1 Energy transfer by direct electron-hole capture

This type of energy transfer is desired for Ce³⁺ activated fast-response inorganic scintillators. After absorbing a gamma ray quantum, free electron and holes are created in the conduction band and valence band, respectively. These free electrons and holes may be trapped within 1 ns by a Ce³⁺ ion. The scintillation and the observed luminescence decay time is characteristic for the relaxation of the excited state of Ce³⁺.

5.4.2 Energy transfer by binary electron-hole diffusion

Instead of being trapped by Ce³⁺, the hole can also be trapped by the host. As was shown previously, self-trapping of the hole is likely to occur and often is a bulk process. This means that the major fraction of the holes that are produced are created randomly in the ionic crystal and not near a particular site, e.g. Ce³⁺. At a certain temperature, the self-trapped hole (V_K or H centre) becomes mobile and may be trapped by Ce³⁺ eventually. Recombination with the electron will excite the Ce³⁺ centre. Alternatively, it is also possible that Ce³⁺ traps the electron first, and that the

V_K or H centre diffuses to Ce^{3+} . However, the trapping of an electron by Ce^{3+} has a rather low probability and has only been observed in CaF_2 , SrF_2 , and BaF_2 [28]. If one assumes (i) a binary electron-hole recombination as described above, (ii) that the electrons and holes are distributed randomly, and (iii) that the electron diffusion migration is random, then the scintillation decay is described by a $(1 + ct)^{-2}$ dependence [29], where the “constant” c may vary with temperature.

The motion of a self-trapped hole can be described by a modification of the general theory of small polaron diffusion [30]. In this theory, the V_K centre is treated as a small polaron that diffuses through the lattice by a random hopping to neighbouring sites, where each jump has to overcome a potential barrier by thermal activation. In the high temperature limit, $\hbar\omega/kT \rightarrow 0$, these treatments predict a transition probability W , for the hole and the relaxed lattice around it to go from one lattice site to an adjacent one as:

$$W = \nu e^{\frac{-E}{kT}} \quad (4)$$

where ν is a frequency factor, E the thermal activation energy, and k Boltzmann’s constant [31,32]. The diffusion constant D of the hopping motion is given by R^2W , where R is the length of the hop. Calculations by T. Lida *et al.* [33] and R. Monnier *et al.* [34] show that the activation energy for V_K diffusion in $CsCl$, $CsBr$, and CsI decreases in the order $Cl > Br > I$. This can be seen in Table I, where we compiled some experimentally determined and calculated values of the activation energy E and the diffusion constant D .

Table I. Experimentally determined activation energies, E_{exp} and calculated activation energies, E_{calc} for different angles of re-orientation, and the diffusion constant, D_{exp} at room temperature of the V_K centre in several alkali halides.

Alkali halide	E_{exp} (eV)	V_K centre			D_{exp} (cm ² /s)
		E_{calc} (eV)			
		60°	90°	180°	
NaCl	0.42 ^{d)}	0.79 ^{b)}	1.18 ^{b)}	1.47 ^{b)}	-
NaBr	0.36 ^{d)}	-	-	-	-
NaI	0.18 ^{a)}	-	-	-	$> 4 \cdot 10^{-4}$ ^{a)}
KCl	0.54 ^{a)}	1.03 ^{b)}	1.55 ^{b)}	2.04 ^{b)}	10^{-10} ^{a)}
KBr	0.45 ^{d)}	-	-	-	-
KI	0.27 ^{a)}	-	-	-	$4 \cdot 10^{-6}$ ^{a)}
RbCl	0.59 ^{d)}	1.04 ^{b)}	1.57 ^{b)}	2.07 ^{b)}	-
RbBr	0.53 ^{d)}	-	-	-	-
RbI	0.28 ^{a)}	-	-	-	$> 5 \cdot 10^{-8}$ ^{a)}
CsCl	-	-	0.76 ^{c)}	0.98 ^{c)}	-
CsBr	0.27 ^{e)}	-	0.73 ^{c)}	0.90 ^{c)}	-
CsI	0.16 ^{d)}	-	0.64 ^{c)}	0.74 ^{c)}	-

a) Ref. [31] b) Ref. [32] c) Ref. [34] d) Ref. [35] e) Ref. [36]

Disappointingly, the calculated values for the activation energy disagree with the experimental data by a factor of at least two. Song [32] attributed this to the simplistic model of a perfect lattice and the quantum mechanical approximations used. Ascarelli *et al.* [35] used a phenomenological model to predict the activation energy of

diffusion of V_K centres. He showed that one-sixth of the Stokes shift of the singlet exciton peak plus one-third of the potential energy of the electron, is in excellent agreement with the experimentally determined values for the activation energy of diffusion of V_K centres presented in Table I. A similar trend with type of halogen has been observed for KCl, KBr, and KI [37]. Here, the temperature at which the rate of re-orientation of the V_K centre is maximal, i.e. the translation of the V_K centre through the lattice, decreases in the series $Cl > Br > I$. For Ce^{3+} activated inorganic scintillators, the diffusion rate of the V_K centre towards Ce^{3+} is likely to increase as well in the order $Cl > Br > I$.

5.4.3 Energy transfer by STE diffusion

A third type of energy transfer that is discussed in this thesis is *STE diffusion*. In principle, the STE can transfer its energy to Ce^{3+} by two different mechanisms, i.e. (non-) radiative energy transfer, or STE diffusion. In the first case, overlap between the STE emission band and the energy levels of Ce^{3+} is necessary. For this type of energy transfer a strong temperature dependence is not expected and the scintillation decay associated with this mechanism is characteristic of the lifetime of the STE. Since the lifetime of the σ -polarised bands is in general much smaller than the intrinsic lifetime of Ce^{3+} , only the π -polarised bands contribute significantly to the elongation of the scintillation decay time.

In the case of *STE diffusion* [38], the STEs move through the lattice by a hopping like motion. The diffusion process is thermally activated and the mobility of the STE increases when the temperature rises. However, STE emission is usually thermally quenched at elevated temperatures and thus there will be an optimum temperature for maximum energy transport efficiency. Table II gives the experimentally determined and calculated values of the activation energy E and the diffusion constant D of the STE in NaCl, NaBr, and NaI.

Table II. Experimentally determined and calculated activation energies E_{exp} and E_{calc} , and the diffusion constant D_{exp} , at room temperature of the STE in NaCl, NaBr, and NaI.

Alkali halide	STE		
	E_{exp} (eV)	E_{calc} (eV)	D (cm ² /s)
NaCl	0.15 ^{a)}	0.16 ^{b)}	$2 \cdot 10^{-5}$ ^{a)}
NaBr	-	0.18 ^{b)}	-
NaI:K	0.07 ^{c)}	-	$1 \cdot 10^{-2}$ ^{c)}
NaI:TI	0.07 ^{c)}	-	$2 \cdot 10^{-2}$ ^{c)}

^{a)} Ref. [38] ^{b)} Ref. [39] ^{c)} Ref. [40]

In case of energy transfer from the STE to Ce^{3+} , the effective lifetime τ_{STE} of the STE is given by

$$\frac{1}{\tau_{STE}} = \frac{1}{\tau_0} + k_q + k_t \quad (5)$$

where τ_0 is the intrinsic lifetime of the STE, k_q the rate of thermal quenching of the STE, and k_t the rate of energy transfer from the STE to Ce^{3+} . The thermal quenching

rate and the energy transfer rate can be described by the general expression $\nu e^{-E/kT}$ with a frequency factor ν and an activation energy E . Accordingly, the expansion of (5) yields

$$\frac{1}{\tau_{STE}} = \frac{1}{\tau_0} + \nu_q \exp\left(-\frac{E_q}{kT}\right) + \nu_t \exp\left(-\frac{E_t}{kT}\right) \quad (6)$$

In this formula, τ_0 is the radiative decay time of the STE, E_q and ν_q are the activation energy and frequency factor for thermal quenching, respectively, E_t and ν_t are the activation energy and frequency factor for energy transfer from the STE to Ce^{3+} , respectively, and k the Boltzmann constant.

In the high temperature limit, the diffusion of the STE through the lattice can be described by a hopping-like motion from one lattice site to a nearest neighbour site [41]. The rate of energy transfer from the STE to Ce^{3+} in an isotropic medium is given by [42]

$$k_t = 4\pi DRN_{Ce} \quad (7)$$

where D , R , and N_{Ce} are the diffusion constant of the STE, the radial distance from a Ce^{3+} centre in which the STE transfers its energy, and the Ce concentration, respectively. The intensity as function of Ce concentration and time, $n_{STE}(t,x)$ of the STE and $n_{Ce}(t,x)$ of excited Ce^{3+} ions, is given by

$$n_{STE}(t,x) = n_{STE}^0(x) \exp\left\{-\left(\frac{1}{\tau_0} + k_q + k_t\right)t\right\} \quad (8)$$

$$n_{Ce}(t,x) = \frac{n_{STE}^0(x)k_t}{\frac{1}{\tau_{Ce}} - \left(\frac{1}{\tau_0} + k_q + k_t\right)} \left[\exp\left\{-\left(\frac{1}{\tau_0} + k_q + k_t\right)t\right\} - \exp\left(-\frac{t}{\tau_{Ce}}\right) \right] K + n_{Ce}^0(x) \exp\left(-\frac{t}{\tau_{Ce}}\right) \quad (9)$$

where $n_{STE}^0(x)$ is the number of STEs initially created after absorption of a gamma quantum as function of Ce concentration at time $t = 0$, and $n_{Ce}^0(x)$ the number of excited Ce^{3+} ions as function of Ce concentration at time $t = 0$. The total scintillation light yield as function of time and Ce concentration will be given by the sum of (8) and (9). The first term of (9) is due to energy transfer from the STE to Ce^{3+} centres which is dependent on both STE and Ce concentrations, whereas the second term of (9) is due to *direct capture of electron-hole pairs* by Ce^{3+} which is governed by the Ce concentration only. If the Ce concentration is increased, $n_{Ce}^0(x)$ will increase and the second term of (9) will become more important.

Equations (8) and (9) predict an exponential decay of both STE and Ce^{3+} luminescence. In the past, a diffusion limited energy transfer has been suggested for NaCl:Li [38] to account for the observed exponential square root dependence of the luminescence decay with time

$$I(t) = I_0 \exp(-at - 2b\sqrt{t}) \quad (10)$$

where I_0 , a and b are constants. However, in a review by Jonscher and de Polignac [43] it was shown that often the luminescence does not decay exponential but follows a power law dependence on time with fractional exponent s

$$I(t) \propto t^{-s} \quad (11)$$

with $0 < s < 2$ [44]. The physical processes underlying the delayed luminescence according to the power law of equation (11) may be very complex and may involve several stages, but in general a power law dependence between luminescence intensity and time is expected when there is some sort of tunnelling, diffusion or percolation of the energy carriers (STEs) in combination with a distribution of tunnelling probabilities or energy barriers.

If we compare the activation energies and the diffusion constants for the diffusion of the V_K centre and the STE in the alkali halides, it becomes clear that STE diffusion proceeds at a much higher rate than V_K diffusion, due to the generally lower activation energies and the larger diffusion constants. Therefore, STE diffusion is favoured over V_K diffusion in Ce^{3+} activated inorganic scintillators. An explanation for the differences between STE diffusion and V_K diffusion may be found in the electric charge of the defect. From a long range perspective, the STE is electrically neutral whereas the V_K centre has a net positive charge. The hopping of the V_K centre from one lattice position to the next requires more energy than the hopping of the STE from one lattice position to the next, because the V_K centre is more strongly bound to its present lattice position by the short –and long range electrostatic Coulomb interactions.

5.5 Luminescence

The last stage in the scintillation process is the transfer of energy to the luminescent centre which in turn will emit a photon with a certain probability. For the following discussion, we will restrict ourselves to the luminescence of the Ce^{3+} ion in Ce^{3+} activated inorganic scintillators.

In inorganic scintillators doped with cerium, the Ce^{3+} ion acts as luminescent centre. This trivalent lanthanide ion has one electron in the $4f$ ground state configuration. The $4f$ electron is shielded from the crystal field by $5p$ and $5s$ electron shells. Excitation of Ce^{3+} promotes the f electron to a higher $5d$ orbital. Subsequent de-excitation will occur by a $5d \rightarrow 4f$ electric dipole allowed transition with a decay time of about $\tau = 15 - 60$ ns. Since the energy difference between the lowest energy of the Ce^{3+} $5d$ configuration and the highest energy of the Ce^{3+} $4f$ configuration is large, multiphonon-relaxation from the $5d$ to the $4f$ groundstate is unlikely to occur. However, when the lowest multiplet of the Ce^{3+} $5d$ configuration is admixed with conduction band wave functions, excitation of the $4f$ electron to a higher $5d$ orbital may result in auto-ionisation of Ce^{3+} and the excitation energy is lost; the electron immediately de-localises in the conduction band and may eventually be trapped at another impurity or at a dislocation in the perfect lattice. For this reason $La_2O_3:Ce^{3+}$,

$\text{Lu}_2\text{O}_3:\text{Ce}^{3+}$, and $\text{LaAlO}_3:\text{Ce}^{3+}$ do not show Ce^{3+} luminescence. Therefore, knowledge of the positions of the Ce^{3+} $5d$ levels inside the band gap is of great importance to the understanding of the scintillation mechanisms and the probability of energy transfer to Ce^{3+} and its luminescence.

5.6 Summary

Multiplication, relaxation and thermalisation of the electrons and holes, *energy transfer*, and the *luminescence* quantum efficiency of the optical centre determine the scintillation efficiency. For the light yield Y , expressed in photons per megaelectronvolt of absorbed gamma ray energy (ph/MeV), the following expression is derived:

$$Y = \frac{10^6 S Q}{\beta E_g} \quad (12)$$

where S is the efficiency of energy transport to the optical centre, Q the luminescence quantum efficiency of the optical centre, E_g the energy of the bandgap between the valence band and conduction band (expressed in eV), and βE_g denotes the energy needed to create one electron - hole pair (expressed in eV). According to (11), the light yield is inversely proportional to the energy of the band gap and a higher light yield should be obtained for materials with an increasingly smaller bandgap. Generally, Q is assumed to be close to unity.

The value for S is closely related to the energy transport efficiency and is normally not easy to predict. As was shown in the previous paragraphs, there are many processes to be considered when evaluating the scintillation properties of a certain scintillator, and the presence of a dominant scintillation mechanism does not allow for the conclusive determination of the value for S . Obviously, this is also the weakness of (11). If we do not know the value of S , we cannot predict accurately the minimum light yield and as such, (11) provides merely a quantitative approximation of maximal attainable light yield.

References

- ¹ R. Hofstadter, Phys. Rev. 74 (1948) 100.
- ² R. Hofstadter, Phys. Rev. 75 (1949) 796.
- ³ P. Lecoq, "The Challenge of new scintillator development for High Energy Physics," in Proceedings of the International Conference on Inorganic Scintillators and their Applications, SCINT 97, Shanghai Branch Press, Shanghai, China, 1997, p. 13.
- ⁴ M. Kobayashi, Y. Usuki, M. Ishii, T. Yazawa, K. Hara, M. Tanaka, M. Nikl, S. Baccaro, A. Cecilia, M. Diemoz, I. Dafinei, "Improvement in Scintillation Characteristics of PbWO_4 Scintillation Crystals by La-doping," in Proceedings of the International Conference on Inorganic Scintillators and their Applications, SCINT 97, Shanghai Branch Press, Shanghai, China, 1997, p. 167.
- ⁵ M.J. Weber, R.R. Monchamp, J. Appl. Phys. 44 (1973) 5495.
- ⁶ P. Lecoq, J.P. Martin, M. Schneegans, M. Vivargent, Europhys. News 16 (1985) 8.
- ⁷ E. Sakai, IEEE Trans. Nucl. Sci. 34 (1987) 418.
- ⁸ I. Holl, E. Lorenz, G. Margeras, IEEE Trans. Nucl. Sci. 35 (1987) 105.
- ⁹ V.D. Ryzhikov, V.P. Sokhin, Instr. Exp. Tech. 31 (1988) 1303.
- ¹⁰ A.J. Bird, T. Carter, A.J. Dean, D. Ramsden, B.M. Swinyard, IEEE Trans. Nucl. Sci. 40 (1993) 395.
- ¹¹ J. Brose, G. Dahlinger, K.R. Schubert, Nucl. Instr. Meth. Phys. Res. A 417 (1998) 311.
- ¹² R.B. Murray, A. Meyer, Phys. Rev. 122 (1961) 815.

-
- ¹³ M. Luntz, *Phys. Rev. B* 4 (1971) 2857.
- ¹⁴ P.A. Rodnyi, P. Dorenbos, C.W.E. van Eijk, *Phys. Stat. Sol. B* 187 (1995) 15.
- ¹⁵ A.J. Wojtowicz, J. Glodo, D. Wisniewski, A. Lempicki, *J. Lumin.* 72-74 (1997) 731.
- ¹⁶ J.C. van't Spijker, P. Dorenbos, C.W.E. van Eijk, K. Krämer, H.U. Güdel, *J. Lumin.* 85 (1999) 1.
- ¹⁷ O. Guillot-Noël, J.T.M. de Haas, P. Dorenbos, C.W.E. van Eijk, K. Krämer, H.U. Güdel, *J. Lumin.* 85 (1999) 21.
- ¹⁸ G.F. Knoll, "Radiation Detection and Measurement," 3rd edition, J. Wiley & Sons, New York, U.S.A., 2000, ch. 4.
- ¹⁹ A.J.J. Bos, F. Draaisma, W.J.C. Okx, C.E. Rasmussen, "Inleiding tot de stralingshygiëne," Elsevier gezondheidszorg, Maarssen, 2000, p. 64.
- ²⁰ W. Shockley, *Sol. St. Elec.* 2 (1961) 35.
- ²¹ C.A. Klein, *J. Appl. Phys.* 39 (1968) 2029.
- ²² W. van Roosbroeck, *Phys. Rev.* 139 (1965) A1702.
- ²³ A. Rothwarf, *J. Appl. Phys.* 44 (1973) 752.
- ²⁴ D.J. Robbins, *J. Electrochem. Soc.* 127 (1980) 2694.
- ²⁵ A.N. Jette, T.L. Gilbert, T.P. Das, *Phys. Rev.* 184 (1969) 884.
- ²⁶ R.T. Williams, K.S. Song, *J. Phys. Chem. Sol.* 51 (1990) 679.
- ²⁷ S. Satpathy, *Phys. Rev. B* 33 (1986) 8706.
- ²⁸ C. Pedrini, P.O. Pagost, C. Madej, D.S. McClure, *J. Physique* 42 (1981) 323.
- ²⁹ H.W. Leverenz, "An Introduction to luminescence in solids," in: *Structure and Matter Series*, Wiley, London, 1950, p. 270.
- ³⁰ J. Yamashita, T. Kurosawa, *J. Phys. Soc. Jpn.* 15 (1960) 802.
- ³¹ R.D Popp, R.B. Murray, *J. Phys. Chem. Sol.* 33 (1972) 601.
- ³² K.S. Song, *Sol. St. Commun.* 9 (1971) 1263.
- ³³ T. Lida, R. Monnier, *Phys. Stat. Sol. (b)* 74 (1976) 91.
- ³⁴ R. Monnier, K.S. Song, A.M. Stoneham, *J. Phys. C.: Sol. St. Phys.* 10 (1979) 4441.
- ³⁵ G. Ascarelli, R.H. Sturen, *Phys. Rev. B* 11 (1975) 4045.
- ³⁶ A.Ch. Lushchik, A.E. Ots, L.A. Pung, S.P. Reifman, V.O. Seman, Yu.Yu. Khaldre, *Bull. Acad. Sci. USSR Physical Series*, 38 (1974) 137.
- ³⁷ C.J. Delbecq, W. Hayes, P.H. Yuster, *Phys. Rev.* 121 (1961) 1043.
- ³⁸ K. Tanimura, N. Itoh, *J. Phys. Chem. Solids* 42 (1981) 901.
- ³⁹ L.F. Chen, K.S. Song, C.H. Leung, *Nucl. Instr. Meth. Phys. Res. B* 46 (1990) 216.
- ⁴⁰ S. Nagata, K. Fujiwara, H. Nishimura, *J. Lumin.* 47 (1991) 147.
- ⁴¹ K.S. Song, *J. Phys. C.* 34-9 (1973) 495.
- ⁴² T.R. Waite, *Phys. Rev.* 107 (1957) 463.
- ⁴³ A.K. Jonscher, A. de Polignac, *J. Phys. C.: Solid State Phys.* 17 (1984) 6493.
- ⁴⁴ L.A. Dissado, *Chem. Phys. Lett.* 124 (3) (1986) 206.

6. Scintillation mechanism in $\text{LaCl}_3:\text{Ce}^{3+}$ and $\text{LaBr}_3:\text{Ce}^{3+}$

6.1 Introduction

In chapter 4 we presented the optical and scintillation properties of the $\text{LaCl}_3:\text{Ce}^{3+}$ and $\text{LaBr}_3:\text{Ce}^{3+}$ scintillators relevant for application. It was shown that both have a high light yield, good timing properties, and excellent energy resolution of about 3% at 662 keV. In this chapter we will review the scintillation properties of $\text{LaCl}_3:\text{Ce}^{3+}$ and $\text{LaBr}_3:\text{Ce}^{3+}$ and present additional data aimed at understanding the scintillation mechanisms. It is shown that *STE diffusion* and *direct capture of electron-hole pairs* are the dominant energy transport mechanisms.

6.2 Results

In order to systematically investigate the scintillation properties of $\text{LaCl}_3:\text{Ce}^{3+}$ and $\text{LaBr}_3:\text{Ce}^{3+}$, we used a series of single crystals of LaCl_3 and LaBr_3 doped with different Ce concentrations. The crystals were grown by the vertical Bridgman technique. Details can be found in chapter 4.

6.2.1 X-ray excited optical luminescence

The X-ray excited optical luminescence spectra of pure LaCl_3 , $\text{LaCl}_3:0.57\%$, 2%, 4%, 10%, and 30% Ce^{3+} at room temperature are shown in Fig. 1. The spectra are corrected for the wavelength dependence of the photodetector quantum efficiency as well as monochromator transmission. Each spectrum is normalised such that its integral over all wavelengths is equal to the value for the absolute light yield expressed in photons per MeV, as found from pulse-height spectra recorded with a shaping time of 10 μs (see chapter 4, section 2). For pure LaCl_3 , the X-ray excited optical luminescence spectrum at room temperature consists of a broad structured band with its maximum near 400 nm. It is attributed to self-trapped exciton (STE) luminescence. For other chlorides [1], and pure LaF_3 [2], similar bands have been observed and were readily assigned to STE luminescence.

The X-ray excited optical luminescence spectra of the cerium-doped LaCl_3 crystals are dominated by a broad emission band located between 300 and 400 nm. It is attributed to Ce^{3+} luminescence. In addition, a weak emission band can be observed between 400 and 550 nm. It is not present under optical excitation and is probably due to some residual STE luminescence. With increasing Ce concentration, the intensity of the residual STE luminescence decreases and that of the Ce^{3+} luminescence increases. For $\text{LaCl}_3:10\% \text{Ce}^{3+}$, the contribution of Ce^{3+} emission to the total light yield is about 35 times higher than that of the STE, whereas in $\text{LaCl}_3:0.57\% \text{Ce}^{3+}$, it is only 2 times higher. Assuming that the peak position and the width of the STE luminescence band remains equal for all Ce^{3+} concentrations, the light yield of both STE and Ce^{3+} luminescence were estimated. The results are shown in Table I.

The temperature dependence of Ce^{3+} and STE luminescence intensity in $\text{LaCl}_3:\text{Ce}^{3+}$ were measured for pure LaCl_3 , $\text{LaCl}_3:0.57\%$, 2% , 4% , and $10\% \text{Ce}^{3+}$. The results on $\text{LaCl}_3:0.57\% \text{Ce}^{3+}$ have already been published by Guillot-Noël *et al.* [3]. The temperature-dependent X-ray excited optical luminescence spectra of pure LaCl_3 , measured between 100 and 400 K with step size of 50 K are shown in Fig. 2 (a). For pure LaCl_3 , the total light yield decreases with temperature. The total light yield at 400 K with respect to that at 100 K is about 50%. It is due to thermal quenching of STE luminescence.

Table I. Light yields of $\text{LaCl}_3:\text{Ce}^{3+}$ derived from X-ray excited optical luminescence spectra. The error in the total light yield is about 10%.

$[\text{Ce}^{3+}]$ (at%)	Ce^{3+} light yield (ph/MeV)	STE light yield	Total light yield (ph/MeV)
-	-	34,000	34,000
0.57	26,600	13,400	40,000
2	39,800	9,200	49,000
4	45,800	3,200	49,000
10	47,200	1,800	49,000
30	42,700	300	43,000

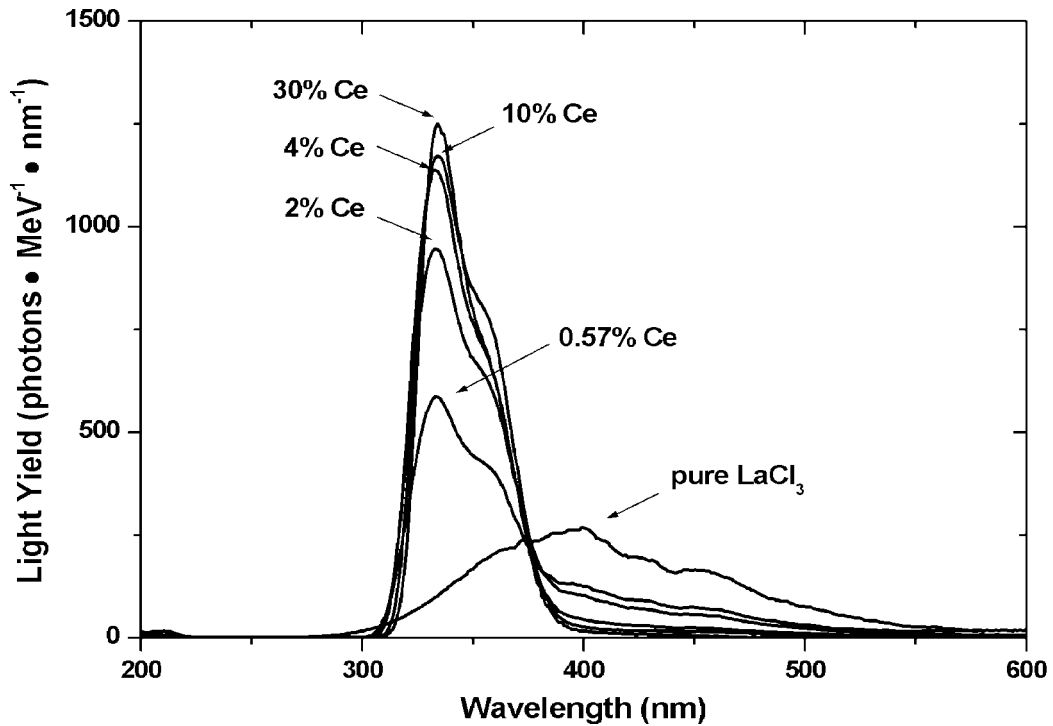
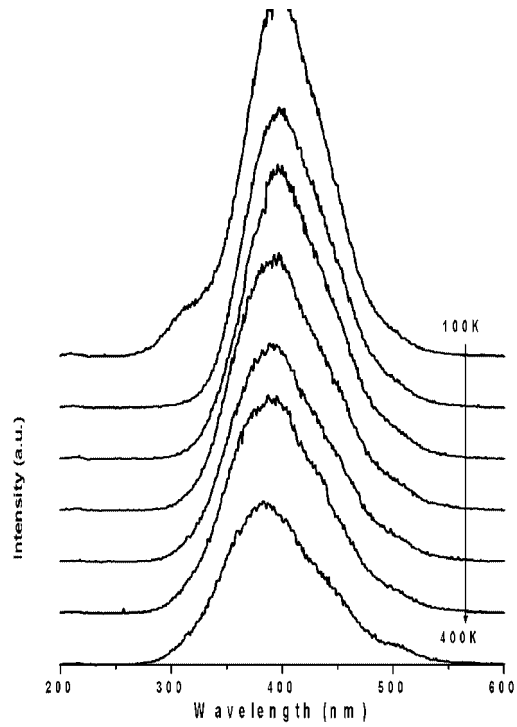
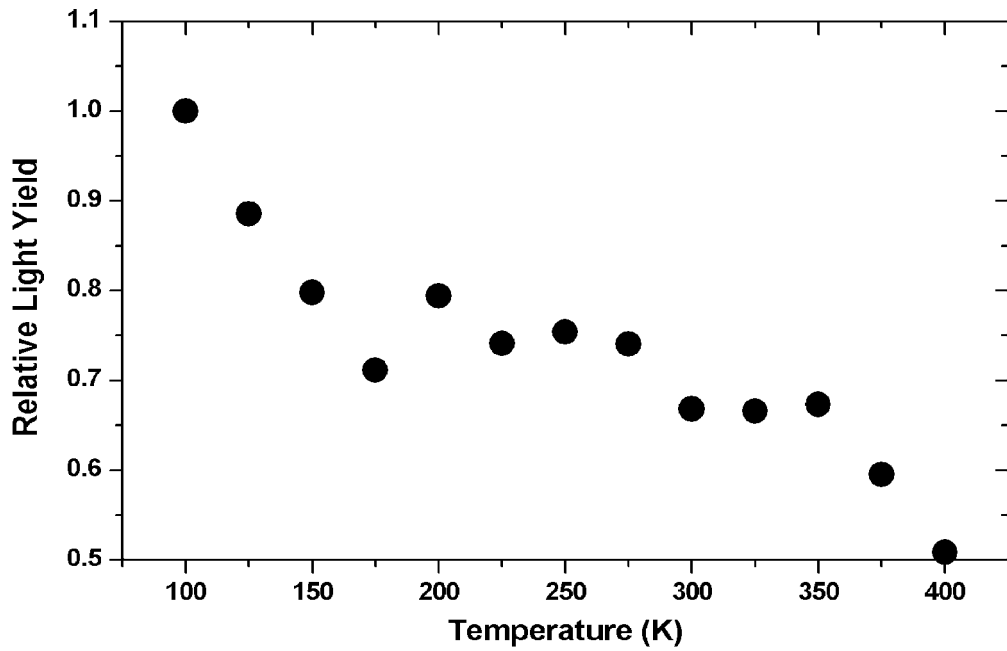


Fig.1 X-ray excited optical luminescence spectra of pure LaCl_3 , $\text{LaCl}_3:0.57\%$, 2% , 4% , 10% , and $30\% \text{Ce}^{3+}$ at room temperature. The y-axis has been calibrated using the light yields derived from pulse-height measurements.



(a)



(b)

Fig. 2 (a) X-ray excited optical luminescence spectra of pure LaCl_3 in the range from 100 to 400 K, recorded in steps of 50 K. The spectra are stacked on top of each other for clarity. (b) Temperature dependence of the total light yield, derived from X-ray excited optical luminescence spectra.

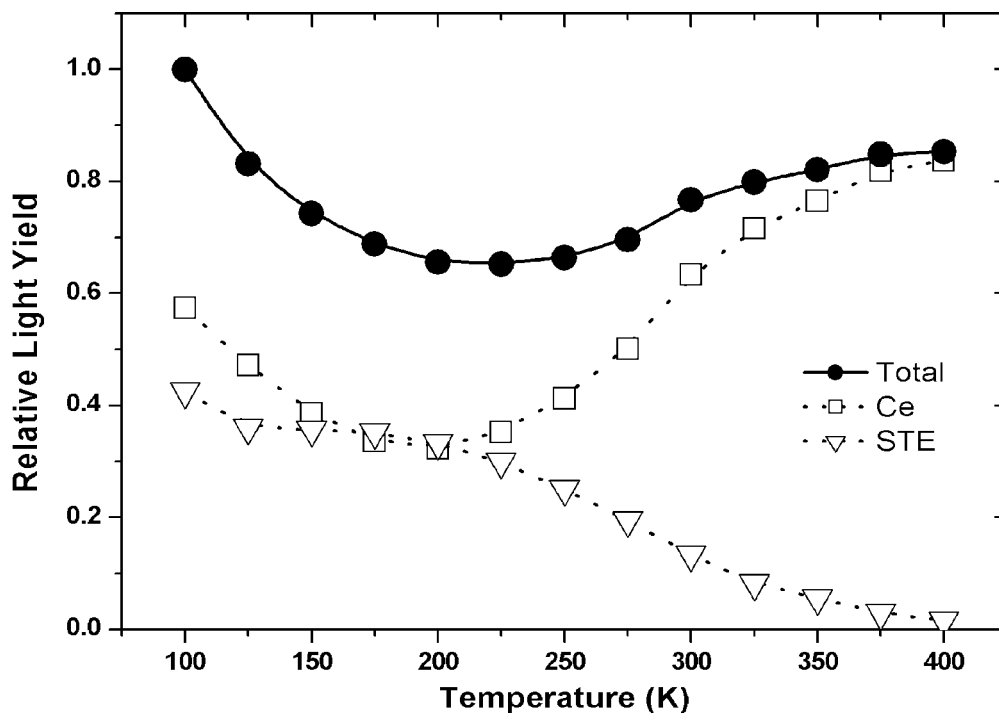


Fig.3 Temperature dependence of the light yields of Ce^{3+} , STE and total luminescence in $\text{LaCl}_3:2\% \text{Ce}^{3+}$, derived from X-ray excited optical luminescence spectra.

In the X-ray excited optical luminescence spectrum at 100 K, a weak emission band can be observed near 320 nm next to the main peak at 390 nm. At elevated temperatures, the 320-nm band has completely disappeared. Thermoluminescence glow curves of pure LaCl_3 irradiated with X-rays at 77 K reveal a main peak at 111 K that is attributed to the release of self-trapped holes [4]. Possibly, the peak at 320 nm in the X-ray excited optical luminescence spectrum of pure LaCl_3 is associated with the release of the self-trapped holes. However, it was suggested by Rogulis *et al.* [5], that the band near 320 nm could also be attributed to STE luminescence.

The temperature dependence of the light yields of Ce^{3+} , STE and total light yield of $\text{LaCl}_3:2\%$, 4% and $10\% \text{Ce}^{3+}$ are shown in Fig. 3, 4, and 5, respectively. Between 100 and 225 K, the light yield of $\text{LaCl}_3:2\% \text{Ce}^{3+}$ is due to the combined luminescence of Ce^{3+} and the STE, see Fig. 3. Both decrease with increasing temperature. From 225 up to 400 K, the Ce^{3+} luminescence intensity is enhanced at the expense of STE luminescence intensity while the total light yield increases as well. The anti-correlation between Ce^{3+} and STE luminescence intensity has been observed before by Guillot-Noël *et al.* in $\text{LaCl}_3:0.57\% \text{Ce}^{3+}$ [3] and by van't Spijker *et al.* in $\text{K}_2\text{LaCl}_5:0.23\% \text{Ce}^{3+}$ [6]. For $\text{LaCl}_3:0.57\%$, 2% , and $4\% \text{Ce}^{3+}$, it is observed between 225 and 400 K, whereas in the case of $\text{K}_2\text{LaCl}_5:0.23\% \text{Ce}^{3+}$ it is observed between 100 and 300 K. As for $\text{LaCl}_3:0.57\%$, 2% and $4\% \text{Ce}^{3+}$, we do observe a change in Ce^{3+} and STE luminescence yield for $\text{LaCl}_3:10\% \text{Ce}^{3+}$ at temperatures in the 100 – 400 K range, see Fig. 5. However, at these temperatures the luminescence intensity is mainly due to Ce^{3+} emission. The contribution of STE luminescence to the total light yield is less than ten percent. In order to emphasise the anti-correlation between Ce^{3+} and STE luminescence intensity, we used a logarithmic scale for the ordinate. Between 100 and 175 K, the STE luminescence intensity remains more or less constant, whereas Ce^{3+} luminescence and total light yield decrease by about 40%. Between 200 and 400 K, Ce^{3+} luminescence and total light yield level at 95% with

respect to that at 100 K. In the same temperature interval, the STE luminescence intensity decreases by about 80%.

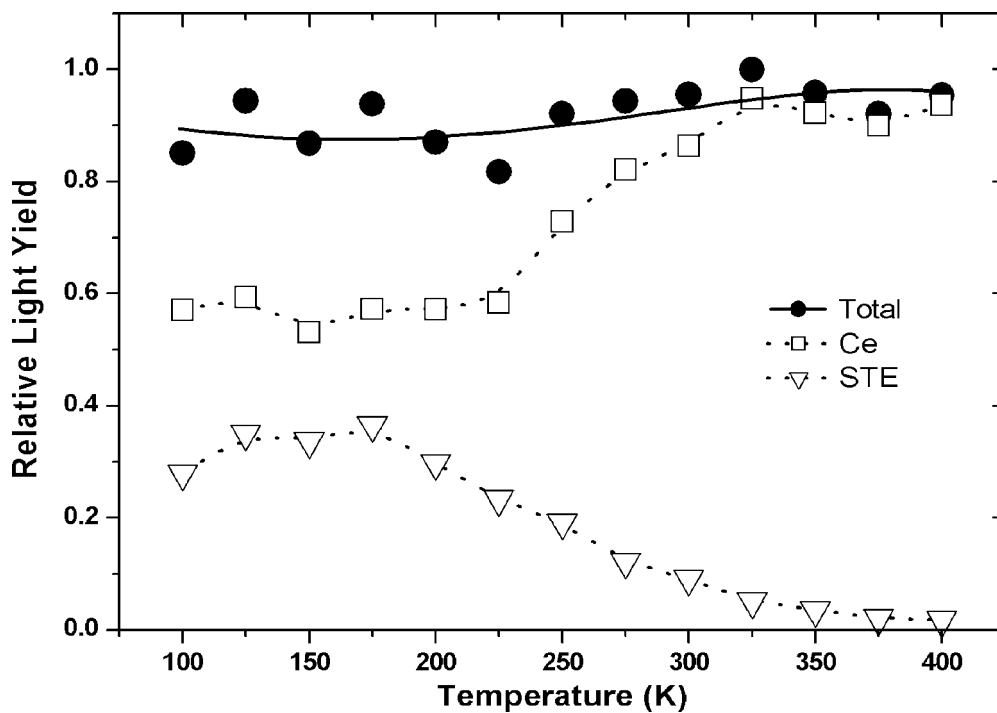


Fig.4 Temperature dependence of the light yields of Ce³⁺, STE and total luminescence in LaCl₃:4% Ce³⁺, derived from X-ray excited optical luminescence spectra.

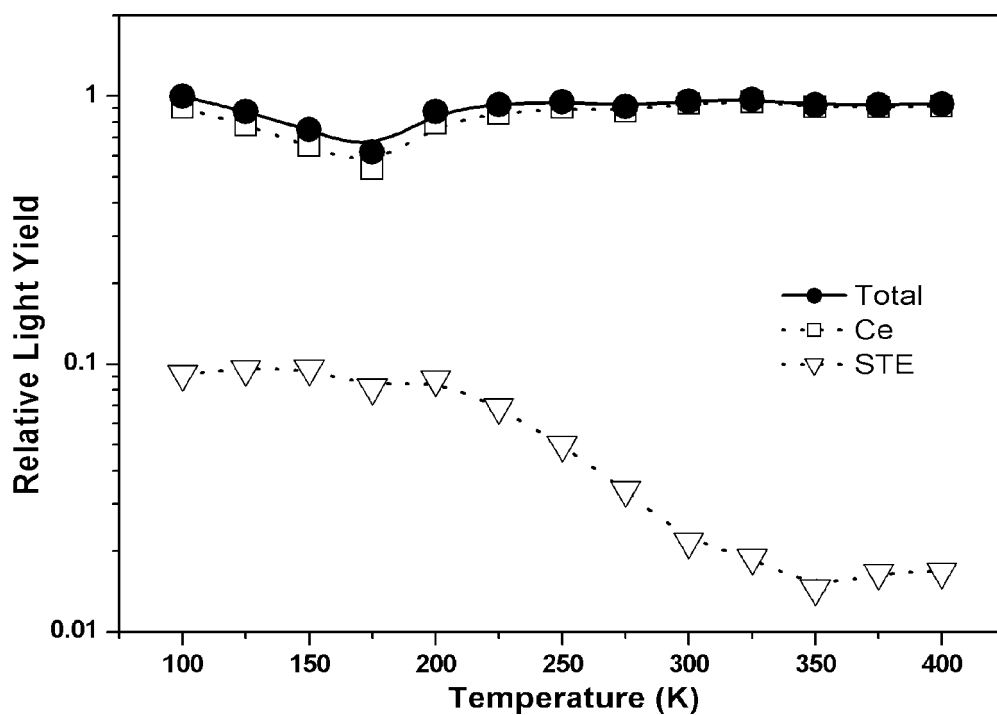


Fig.5 Temperature dependence of the light yields of Ce³⁺, STE and total luminescence in LaCl₃:10% Ce³⁺, derived from X-ray excited optical luminescence spectra.

The X-ray excited optical luminescence spectra of pure LaBr_3 , $\text{LaBr}_3:0.5\%$, 4% , and 10% Ce^{3+} are shown in Fig. 6. For pure LaBr_3 , the spectrum at 100 K (see inset) consists of two broad bands with their maxima near 340 and 430 nm. Both bands are attributed to STE luminescence. At elevated temperatures, the 340 nm band completely disappears and the maximum of the 430 nm band shifts to shorter wavelengths. For other bromides [3,7-9] similar bands have been observed and were readily assigned to STE emission.

The X-ray excited optical luminescence spectra of $\text{LaBr}_3:\text{Ce}^{3+}$ at room temperature are dominated by a broad emission band located between 325 and 425 nm. It is attributed to Ce^{3+} emission. In contrast to $\text{LaCl}_3:\text{Ce}^{3+}$, no residual STE emission is present. Also, with increasing Ce concentration, the intensity of Ce^{3+} luminescence decreases, whereas for $\text{LaCl}_3:\text{Ce}^{3+}$ the Ce^{3+} luminescence intensity increases. In the X-ray excited optical luminescence spectrum of $\text{LaBr}_3:10\% \text{Ce}^{3+}$, an additional emission band is observed near 275 nm. This band was not present in the X-ray excited optical luminescence spectrum of pure LaBr_3 showing only STE luminescence near 340 and 430 nm. Probably, the 275 nm band is due to an impurity trapped exciton or some other defect related to Ce^{3+} .

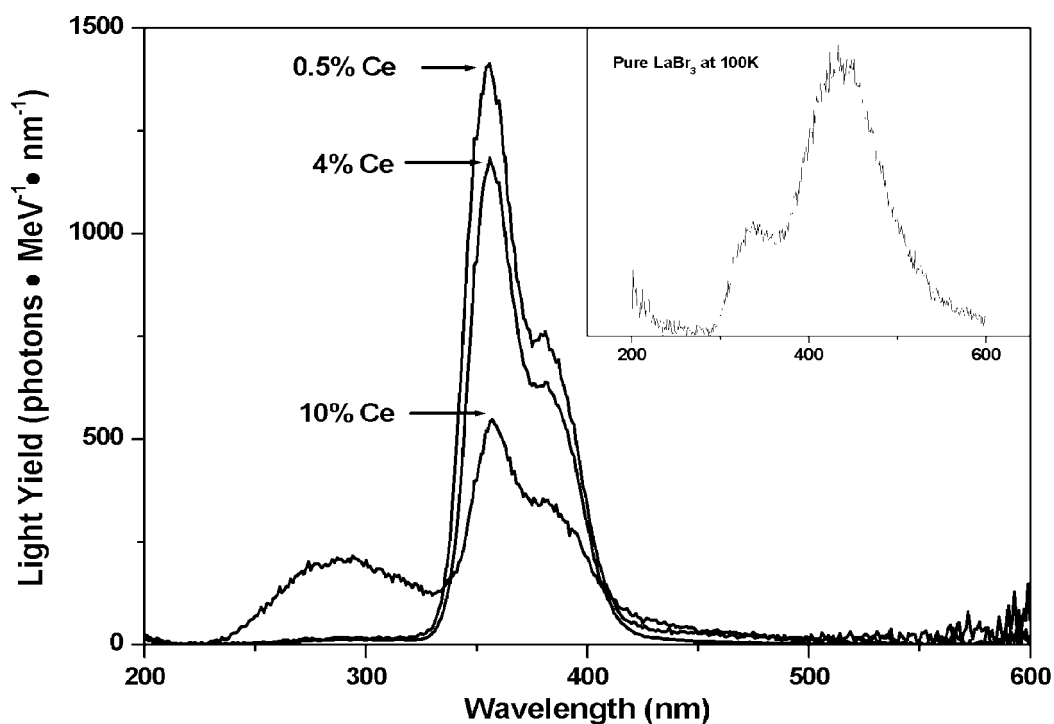


Fig.6 X-ray excited optical luminescence spectra of $\text{LaBr}_3:0.5\%$, 4% , and 10% Ce^{3+} at room temperature. The inset shows the spectrum of pure LaBr_3 at 100 K. The left most y-axis has been calibrated using the light yields derived from pulse-height measurements.

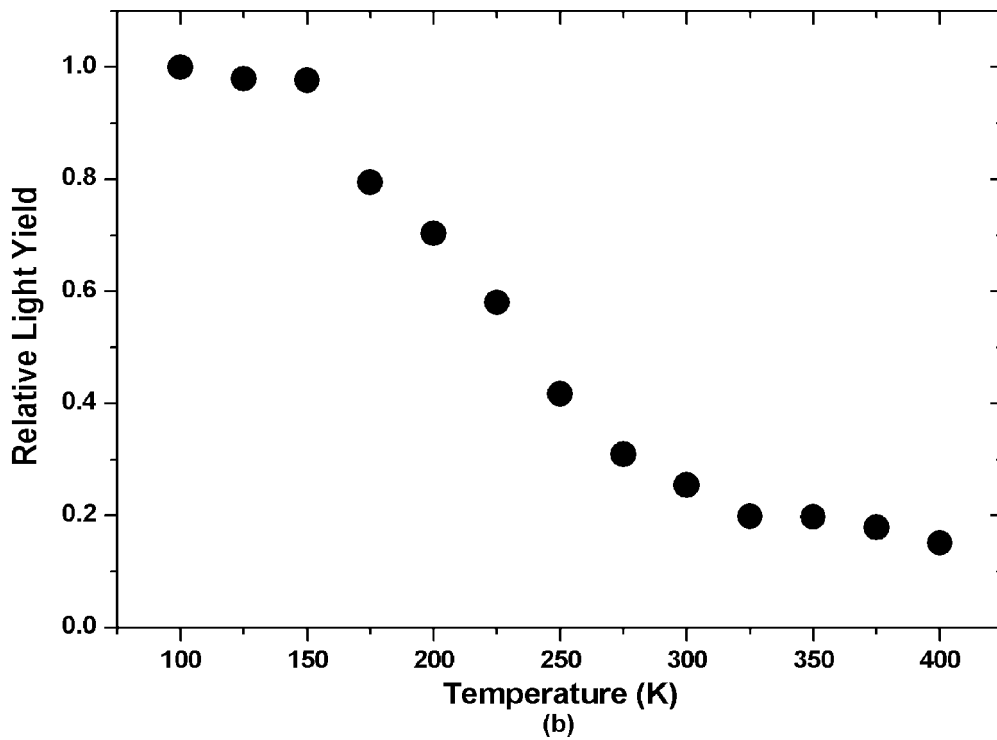
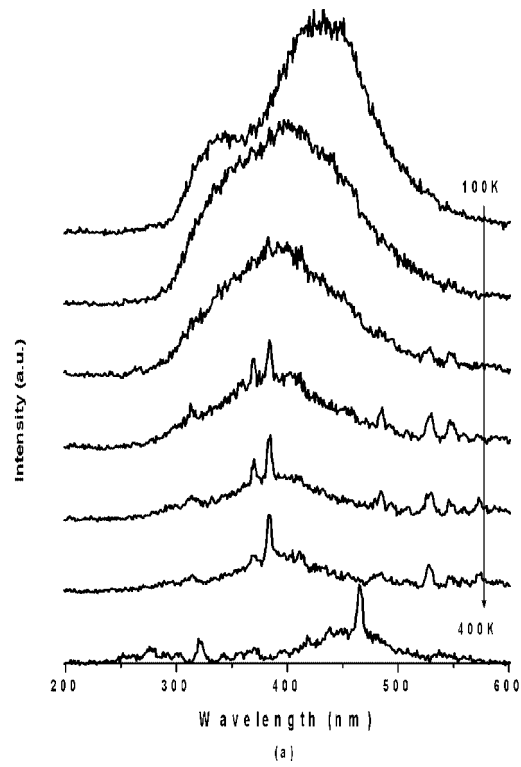


Fig.7 (a) X-ray excited optical luminescence spectra of pure LaBr_3 in the range from 100 to 400 K, recorded in steps of 50 K. The spectra are stacked on top of each other for clarity. (b) Temperature dependence of the total light yield, derived from X-ray excited optical luminescence spectra.

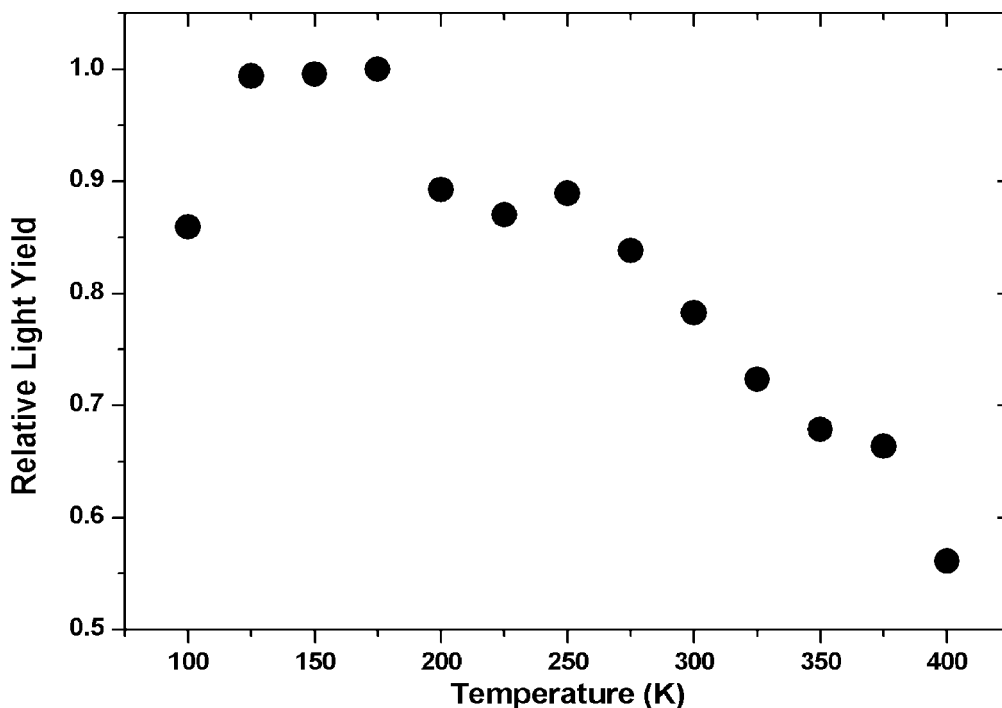


Fig.8 Temperature dependence of the total light yield of $\text{LaBr}_3:0.5\% \text{Ce}^{3+}$.

Temperature-dependent X-ray excited optical luminescence spectra of pure LaBr_3 , measured between 100 and 400 K with step size of 50 K are shown in Fig. 7 (a). For pure LaBr_3 , the total light yield decreases with temperature. The total light yield at 400 K is 15% with respect to that at 100 K. It is due to thermal quenching of STE luminescence. In the X-ray excited optical luminescence spectrum at 100 K, a weak emission band can be observed near 340 nm next to the main peak at 430 nm. At elevated temperatures, the 340 nm band has completely disappeared. The light yield as function of temperature of $\text{LaBr}_3:0.5\% \text{Ce}^{3+}$ is shown in Fig. 8. As for pure LaBr_3 , the total light yield decreases with temperature. At 400 K it is 56% with respect to the maximum at 175. For $\text{LaBr}_3:2\%$, 4% , and $10\% \text{Ce}^{3+}$ a similar correlation between light yield and temperature is observed.

6.2.2. Scintillation decay

Scintillation decay time spectra of pure LaCl_3 , $\text{LaCl}_3:0.57\%$, 2% , 4% , and $10\% \text{Ce}^{3+}$ at room temperature under ^{137}Cs gamma ray excitation are shown in Fig. 9. The irregularity in curve (e) at $t = 2 \mu\text{s}$ is due to after pulses in the photomultiplier tube. For pure LaCl_3 , the scintillation pulse decays exponentially with a decay time of about $3.5 \mu\text{s}$. For LaCl_3 doped with Ce^{3+} , a decay component with a decay time of a few microseconds is also present and can be observed in the scintillation pulse at times larger than, say $1 \mu\text{s}$ after the start of the scintillation pulse. The lifetime of this component becomes increasingly shorter when the Ce concentration is increased: for $\text{LaCl}_3:0.57\%$, 2% , 4% , and $10\% \text{Ce}^{3+}$ it is 2.5 , 1.8 , 1.1 , and $0.8 \mu\text{s}$, respectively. The origin of this decay component is attributed to STE luminescence and energy transfer from the STE to Ce^{3+} . For $\text{K}_2\text{LaCl}_5:\text{Ce}^{3+}$ [6] a similar correlation was found between the lifetime of the long decay component and Ce concentration.

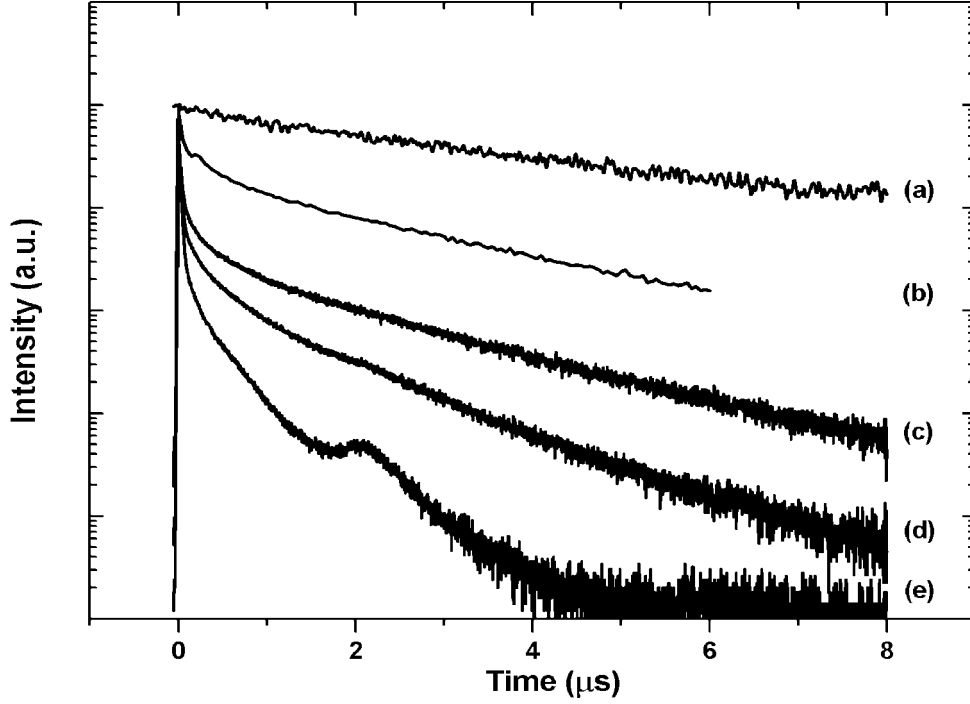


Fig.9 Scintillation decay time spectra at room temperature under ^{137}Cs gamma-ray excitation of (a) pure LaCl_3 , (b) $\text{LaCl}_3:0.57\% \text{Ce}^{3+}$, (c) $\text{LaCl}_3:2\% \text{Ce}^{3+}$, (d) $\text{LaCl}_3:4\% \text{Ce}^{3+}$, and (e) $\text{LaCl}_3:10\% \text{Ce}^{3+}$.

Additionally, a fast decay component is present in the scintillation decay of $\text{LaCl}_3:\text{Ce}^{3+}$ that can be observed in the scintillation pulse at times shorter than, say $1 \mu\text{s}$ after the start of the scintillation pulse. The relative contribution of this component to the total light yield becomes increasingly larger when the Ce concentration is increased: for $\text{LaCl}_3:0.57\%$, 2% , 4% , and $10\% \text{Ce}^{3+}$ it is 8, 10, 18, and 41%, respectively. It is attributed to direct capture of the electron and holes from the conduction band and valence band, respectively, by Ce^{3+} centres.

When we assume that (i) the decreases of the observed lifetime of the STE in $\text{LaCl}_3:\text{Ce}^{3+}$ is only due to energy transfer from the STE to Ce^{3+} and (ii) that the rate of thermal quenching of the STE in $\text{LaCl}_3:\text{Ce}^{3+}$ is comparable with the rate of thermal quenching of the STE in pure LaCl_3 , we can use a simplification of the formula used in chapter 5, section 4 for the effective lifetime τ of the STE

$$\frac{1}{\tau} = \frac{1}{\tau_{\text{pure}}} + k_t \quad (1)$$

where the first term of (1) is the rate of STE decay in pure LaCl_3 and the second term of (1) the rate of energy transfer from the STE to Ce^{3+} . Using equation (1) we can calculate the energy transfer rate, k_t for $\text{LaCl}_3:\text{Ce}^{3+}$. The results are compiled in Table II.

Figure 10 shows the decay curves of $\text{LaCl}_3:1\% \text{Ce}^{3+}$ as function of temperature monitoring Ce^{3+} emission at 3.7 eV. At 167 K, the decay curve of $\text{LaCl}_3:1\% \text{Ce}^{3+}$ shows an almost perfect power-law dependence between Ce^{3+} luminescence intensity and time, according to

$$I(t) \propto t^{-s} \quad (2)$$

with $s \approx 0.3$. If the temperature is raised, the decay curve of $\text{LaCl}_3:1\% \text{Ce}^{3+}$ gradually turns into an exponential decay curve.

Table II. The decay time of the STE, τ and the calculated energy transfer rate, k_t as function of Ce concentration at room temperature.

[Ce] (%)	τ (μs)	k_t (10^5 s^{-1})
-	3.5 ± 0.3	-
0.57	2.5 ± 0.3	1.1 ± 0.1
2	1.8 ± 0.2	2.7 ± 0.3
4	1.1 ± 0.1	6.2 ± 0.6
10	0.8 ± 0.1	9.6 ± 0.9

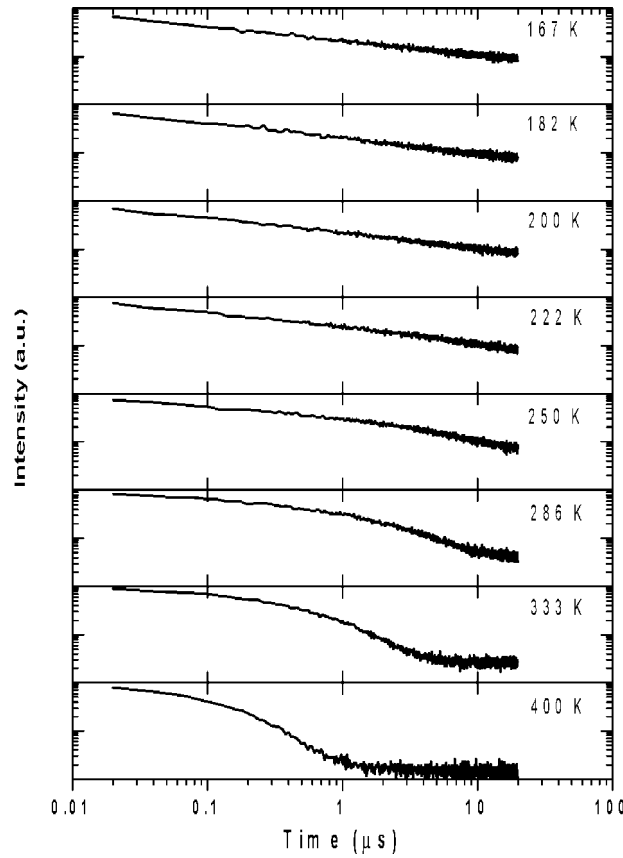


Fig.10 Decay curves of $\text{LaCl}_3:1\% \text{Ce}^{3+}$ as function of temperature. Both axis are scaled on a log 10 base.

In Fig. 11 the decay time τ of the STE in (a) pure LaCl_3 and (b) $\text{LaCl}_3:1\% \text{Ce}^{3+}$ is presented as function of $1/T$ (K^{-1}). The dotted curves show model calculation according to equation (6) in chapter 5 (section 4). From a fit to this equation values for the radiative decay time of the STE τ_0 , the activation energy and frequency factor for thermal quenching, E_q and ν_q , respectively, and the activation energy and frequency factor for energy transfer from the STE to Ce^{3+} , E_t and ν_t , respectively, were obtained. They are summarised in Table III. For $\text{LaCl}_3:1\% \text{Ce}^{3+}$, the values for τ_0 and E_q were taken from the fit of pure LaCl_3 and were assumed to be constant. The activation energies for thermal quenching and energy transfer are $E_q = 108 \pm 8$ meV and $E_t = 24 \pm 2$ meV, respectively. To compare, the activation energy for STE diffusion in NaCl [10], NaI:K , and NaI:Tl [11] was estimated to be 150 meV, 70 meV, and 70 meV, respectively. The value for the radiative decay time of the STE could not be determined with high accuracy due to limitations of the set-up.

Table III. The radiative decay time τ_0 , the activation energy and frequency factor for thermal quenching, E_q and ν_q , respectively, and the activation energy and frequency factor for energy transfer from the STE to Ce^{3+} , E_t and ν_t , respectively, of the STE in pure LaCl_3 and $\text{LaCl}_3:1\% \text{Ce}^{3+}$.

Compound	Radiative decay τ_0 (μs)	Thermal quenching		Energy transfer	
		E_q (meV)	ν_q (10^6 s^{-1})	E_t (meV)	ν_t (10^6 s^{-1})
LaCl_3	~ 50	108 ± 8	18 ± 4	-	-
$\text{LaCl}_3:1\% \text{Ce}^{3+}$	~ 50	108 ± 8	9 ± 1	24 ± 2	1.4 ± 0.2

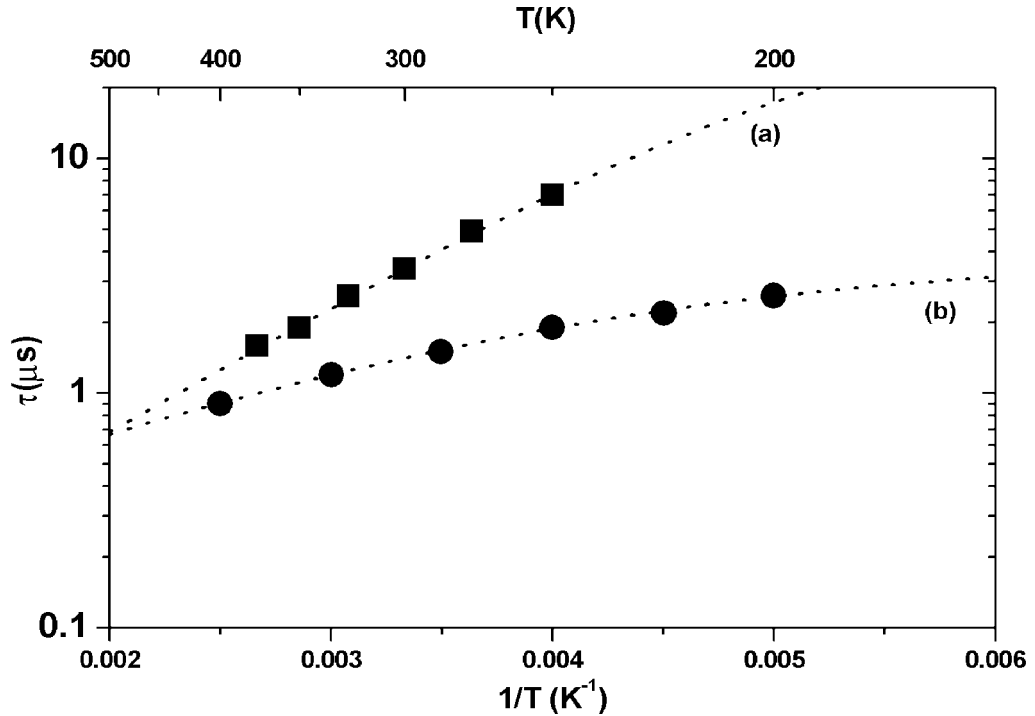


Fig. 11. Decay time of the STE, τ in (a) pure LaCl_3 and (b) $\text{LaCl}_3:1\% \text{Ce}^{3+}$ as function of temperature.

Scintillation decay time spectra of pure LaBr_3 and $\text{LaBr}_3:0.5\% \text{Ce}^{3+}$ at room temperature under ^{137}Cs gamma ray excitation are shown in Figure 12. The scintillation decay curves have been normalised such that the time integral equals the absolute light yield as found from pulse height spectra recorded with a shaping time of $10 \mu\text{s}$. At first sight, the scintillation pulses do not decay exponentially but are probably composed of different decay components, e.g. a relatively short, exponential decay component due to *direct capture of electron-hole pairs* by Ce^{3+} centres and a relatively long decay component due to energy transfer to Ce^{3+} centres by *STE diffusion* or *binary electron-hole recombination* (see chapter 5, section 4). Nevertheless, the contribution of the long decay component to the total light yield of $\text{LaBr}_3:0.5\%$, 2%, 4%, and 10% Ce^{3+} is small. Thus, for practical purposes a simple exponential decay function was used to analyse these curves. To correct for deviations at time scales up to $200 \mu\text{s}$ an additional error in the decay time was taken into account. Table IV summarises the decay components present in $\text{LaCl}_3:\text{Ce}^{3+}$ and $\text{LaBr}_3:\text{Ce}^{3+}$ as well as their relative contribution to the total light yield.

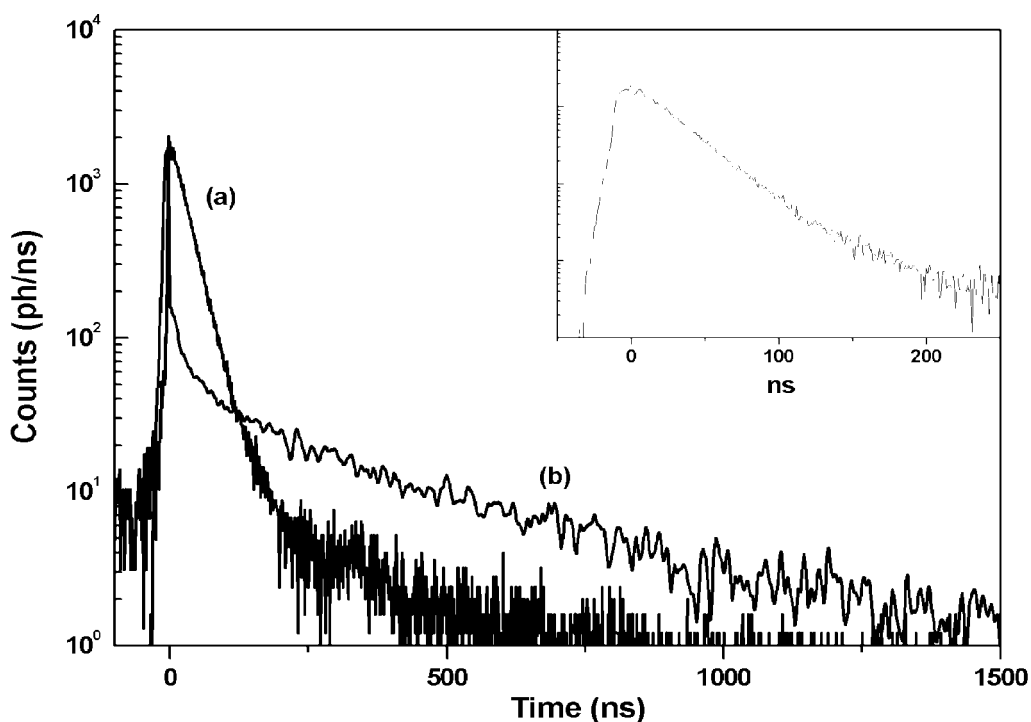


Fig.12 Scintillation decay time spectra of (a) $\text{LaBr}_3:0.5\% \text{Ce}^{3+}$ and (b) pure LaBr_3 at room temperature under ^{137}Cs gamma ray excitation. The inset shows the spectrum of $\text{LaBr}_3:0.5\% \text{Ce}^{3+}$ on an extended time scale.

Table IV. Characteristic components of the scintillation decay curves of pure LaCl₃, LaCl₃:0.57%, 2%, 4%, 10% Ce³⁺, pure LaBr₃, LaBr₃:0.5%, 2%, 4%, and 10% Ce³⁺.

Host	[Ce] (%)	Decay components		
		Short (ns)	Intermediate (ns)	Long (μ s)
LaCl ₃	-	-	-	3.5 \pm 0.1 (100%)
LaCl ₃	0.57	20 \pm 2 (8%)	350 \pm 50 (20%)	2.5 \pm 0.2 (72%)
LaCl ₃	2	27 \pm 3 (10%)	230 \pm 20 (18%)	1.8 \pm 0.2 (72%)
LaCl ₃	4	25 \pm 3 (18%)	210 \pm 20 (25%)	1.1 \pm 0.1 (57%)
LaCl ₃	10	25 \pm 3 (41%)	210 \pm 20 (29%)	0.8 \pm 0.1 (30%)
LaBr ₃	-	22 \pm 2 (16%)	330 \pm 30 (84%)	-
LaBr ₃	0.5	31 \pm 3 (100%)	-	-
LaBr ₃	2	31 \pm 3 (100%)	-	-
LaBr ₃	4	31 \pm 3 (100%)	-	-
LaBr ₃	10	31 \pm 3 (100%)	-	-

6.3 Discussion

6.3.1 LaCl₃:Ce³⁺

In the past, three different scintillation mechanisms have been proposed for LaCl₃:Ce³⁺ [3,12], i.e., *direct capture of electron-hole pairs*, *binary electron-hole recombination*, and *STE diffusion*, of which *STE diffusion* seems to be the most dominant one, especially at low Ce concentrations. Recently [13], two types of STEs have been found at 10 K in the X-ray excited electron-paramagnetic-resonance (EPR) spectra of pure LaCl₃ and LaCl₃:Ce³⁺. Stable self-trapped holes (V_K centres) were not detected at low temperatures ($T < 100$ K) in the EPR spectra, probably because the V_K centre immediately ($t < 10^{-9}$ s) captures an electron from the conduction band to form an STE (see chapter 5, section 3). The presence of STEs in LaCl₃:Ce³⁺ and the absence of stable V_K centres is a strong indication that *STE diffusion* is an important scintillation mechanism in LaCl₃:Ce³⁺ indeed. But also the anti-correlation between STE and Ce³⁺ luminescence intensity, the effective lifetime of Ce³⁺ and STE luminescence that decreases with increasing Ce concentration, and the evolution of the decay profile of LaCl₃:Ce³⁺ with temperature from a power-law dependence to an exponential one support this assumption.

Let us review the data presented thus far. The anti-correlation between STE and Ce³⁺ luminescence intensity as function of Ce concentration is attributed to the *direct capture of electron-hole pairs* and the immediate trapping of part of the STEs by Ce³⁺. In all samples, the fast decay component is due to the former process: when the Ce concentration is increased, the contribution of the fast decay component to the total light yield is expected to increase as well, because the probability of direct capture of electron-hole pairs by Ce³⁺ increases (see chapter 5, section 4). Indeed, from LaCl₃:0.57% Ce³⁺ to LaCl₃:10% Ce³⁺, the contribution of this component to the total light yield increases from 8% to 41% (see Table IV).

The anti-correlation between STE and Ce³⁺ luminescence intensity as function of temperature is due to the mobility of the STE. When the temperature is raised, the mobility of the STE increases and the energy is transferred to a Ce³⁺ centre the moment the STE encounters an Ce³⁺ ion. The anti-correlation can be observed for

LaCl₃:2% Ce³⁺ (Fig. 3), LaCl₃:4% Ce³⁺ (Fig. 4), and LaCl₃:10% Ce³⁺ (Fig. 5) at temperatures $T > 200$ K. The shortening of the decay time of the STE (Figure 9) is consistent with this model. If the Ce concentration is increased, the diffusion path length and travel time of the STE to a Ce³⁺ centre are shortened, as well as the decay time of the STE (see chapter 5, section 4).

For LaCl₃:Ce³⁺ it is assumed that the STE transfers its energy to Ce³⁺ before it decays non-radiatively. This assumption seems reasonable since the activation energy for energy transfer ($E_t = 24 \pm 2$ meV) is significantly lower than the activation energy for thermal quenching ($E_q = 108 \pm 8$ meV). At room temperature kT is about 25 meV which is of the same order of magnitude as the activation energy for energy transfer from the STE to Ce³⁺. This is also a strong indication that *STE diffusion* is a dominant energy transfer mechanism in LaCl₃:Ce³⁺ indeed.

6.3.2 LaBr₃:Ce³⁺

If we assume that *STE diffusion* is also the dominant scintillation mechanism in LaBr₃:Ce³⁺, the diffusion rate of the STEs ought to be much higher than the diffusion rate of the STEs in LaCl₃:Ce³⁺, to account for both the efficient scintillation of LaBr₃:Ce³⁺ at low Ce concentrations and the absence of STE luminescence at room temperature. Additionally, the scintillation pulse of LaBr₃:Ce³⁺ should display a rise time depending on the speed of *STE diffusion*. Indeed, this has been observed in Fig. 12 (see inset).

In chapter 5, section 4, it was shown that there is a possible correlation between the rate of *STE diffusion* and the type of anion in the lattice: the diffusion constant of the STE increases in the series Cl > Br > I. The data presented in this chapter seems to confirm this correlation: LaBr₃:Ce³⁺ is a more efficient and faster scintillator than LaCl₃:Ce³⁺ and does show a risetime in its scintillation pulse, due to the transport of energy carriers to Ce³⁺ centres.

Another possibility is *direct capture of electron-hole pairs* by Ce³⁺. In this case, the decay time is characteristic of the lifetime of the excited state of Ce³⁺ with negligible risetime. Then, an increase in Ce concentration would also mean an increase in the relative contribution of this decay component to the total light yield. However, already for LaBr₃:0.5% Ce³⁺ the short decay component represents over 90% of the total light yield. Increasing the Ce concentration has hardly any effect.

6.4 Conclusions

Although LaBr₃ and LaCl₃ are closely related with respect to crystal structure and other physical properties, doping these matrices with trivalent cerium results in two distinct scintillators. LaBr₃:Ce³⁺ scintillates fast and very efficiently already at low Ce concentrations. LaCl₃:Ce³⁺ needs a relatively high Ce concentration to obtain 41% intensity with a decay component of 25 ns. Another difference is the presence of STEs at room temperature in LaCl₃:Ce³⁺; they appear to be absent in LaBr₃:Ce³⁺.

In the case of LaCl₃:Ce³⁺, V_K centres are created which immediately recombine with an electron to form an STE. Thermally activated STE diffusion to Ce³⁺ is then the dominant scintillation mechanism. It results in a relatively slow decay component. If the Ce concentration is increased, the probability that an STE transfers its energy to Ce³⁺ increases as well. It is also possible that a V_K centre is trapped near Ce³⁺ before a STE can be formed. Recombination with the electron yields Ce³⁺ emission. However,

this process must then be very fast, since there was no evidence of stable V_K or F (electron) centres in EPR spectra of $\text{LaCl}_3:\text{Ce}^{3+}$. As such, it does not contribute to the elongation of the scintillation decay. In principle, Ce^{3+} could also capture a free electron and hole from the conduction and valence band, respectively, leading to fast Ce^{3+} luminescence. However, the contribution of this component to the scintillation decay is relatively small.

For $\text{LaBr}_3:\text{Ce}^{3+}$ we assume that either the V_K centres immediately recombine with an electron to form an STE followed by high speed STE diffusion to Ce^{3+} , or Ce^{3+} captures a free electron and hole from the conduction and valence band, respectively, leading to fast Ce^{3+} luminescence. The contribution of the latter is probably relatively large.

References

- ¹ K.S. Song, R.T. Williams, "Alkali halides," in *Self-Trapped Excitons*, ser. Solid-State Sciences no. 105, M. Cardona, Ed. New York: Springer-Verlag, 1993, ch. 4 and 5.
- ² E. Radzhabov, A.I. Nepomnyashik, *Mater. Sci. For.* 239-241 (1997) 275.
- ³ O. Guillot-Noël, J.T.M. de Haas, P. Dorenbos, C.W.E. van Eijk, K. Krämer, H.U. Güdel, *J. Lumin.* 85 (1999) 21.
- ⁴ S.M. Kuzakov, *Rad. Protect. Dos.* 33 (1) (1990) 115.
- ⁵ U. Rogulis, S. Schweizer, J.-M. Spaeth, E.V.D. van Loef, P. Dorenbos, C.W.E. van Eijk, K. Krämer, H.U. Güdel, to be published.
- ⁶ J.C. van't Spijker, P. Dorenbos, C.W.E. van Eijk, K. Krämer, H.U. Güdel, *J. Lumin.* 85 (1999) 1.
- ⁷ P. Dorenbos, J.C. van't Spijker, O.W.V. Frijns, C.W.E. van Eijk, K. Krämer, H.U. Güdel, A. Ellens, *Nucl. Instr. Meth. B* 132 (1997) 728.
- ⁸ O. Guillot-Noël, J.C. van't Spijker, J.T.M. de Haas, P. Dorenbos, C.W.E. van Eijk, K.W. Krämer, H.U. Güdel, *IEEE Trans. Nucl. Sci.* NS-46 (1999) 1274.
- ⁹ E.V.D. van Loef, P. Dorenbos, C.W.E. van Eijk, K.W. Krämer, H.U. Güdel, *Opt. Commun.* 189 (2001) 297.
- ¹⁰ K. Tanimura, N. Itoh, *J. Phys. Chem. Sol.* 42 (1981) 901.
- ¹¹ S. Nagata, K. Fujiwara, H. Nishimura, *J. Lumin.* 47 (1991) 147.
- ¹² J. Andriessen, O.T. Antonyak, P. Dorenbos, P.A. Rodnyi, G.B. Stryganyuk, C.W.E. van Eijk, A.S. Voloshinovskii, *Opt. Commun.* 178 (2000) 355.
- ¹³ U. Rogulis, S. Schweizer, J.-M. Spaeth, E. V. D. van Loef, P. Dorenbos, C. W. E. van Eijk, K. Krämer, H. U. Güdel, *Rad. Eff. Def. Sol.* 157 (2002) 951.

7. The Elpasolites - $\text{Cs}_2\text{LiYX}_6:\text{Ce}^{3+}$ ($X = \text{Cl}, \text{Br}$)*

7.1 Introduction

The elpasolites with structural composition A_2BMX_6 (with $\text{A} = \text{Rb}, \text{Cs}$; $\text{B} = \text{Li}, \text{Na}, \text{K}$; $\text{M} = \text{La} - \text{Lu}$; $\text{X} = \text{F}, \text{Cl}, \text{Br}$) are model systems investigated in numerous optical, scintillation and magnetic studies. They have the advantage over many other crystalline systems that the M^{3+} site, located at the centre of a regular octahedron of halide ions X^- , offers a natural environment for the incorporation of Ce^{3+} and other trivalent ions. The fact that the crystal structure of Cs_2LiYX_6 remains the same for $X = \text{Cl}$ and Br enables us to study the effect of the anion on the scintillation mechanism in particular. Additionally, the Li – containing elpasolites are possible candidates for neutron sensitive scintillators, as Li – containing compounds possess the ability to convert incident neutrons into secondary ionising particles by the reaction (1)



These materials are of particular interest because of the possible presence of core-valence (CV) luminescence [1]. CV luminescence requires the creation of holes in a metal band by excitation of electrons from this band to the conduction band. Those holes are short lived and may recombine with electrons from the valence band. If this process proceeds radiatively it is called CV luminescence.

CV luminescence was observed for the first time in BaF_2 by Ershov *et al* [2] and studied in the chloro-elpasolite $\text{Cs}_2\text{NaLaCl}_6$ by Voloshinovskii *et al* [3]. The scintillation properties of $\text{Cs}_2\text{NaMCl}_6$ ($\text{M} = \text{La}, \text{Ce}, \text{Lu}$) were studied by van't Spijker *et al* [4]. Unfortunately no CV luminescence was observed, probably because of absorption by impurity Ce^{3+} . Rodnyi *et al* investigated Ce^{3+} - doped $\text{Cs}_2\text{LiLaCl}_6$ [5]. This compound does show CV luminescence, but no detailed study of the scintillation mechanism was reported. Combes *et al* investigated pure and Ce^{3+} - doped $\text{Cs}_2\text{LiYCl}_6$ [6] and reported for the first time on the scintillation mechanism in elpasolites. It was suggested that for low Ce concentrations, both radiative energy transfer from the self-trapped exciton (STE) to Ce^{3+} as well as STE diffusion to Ce^{3+} centres play an important role. For relatively high Ce concentrations ($[\text{Ce}^{3+}] > 1\%$), not the diffusion of the STE to Ce^{3+} centres appeared to be dominant, but trapping and stabilisation of a V_K centre near Ce^{3+} . Electron paramagnetic resonance (EPR) studies on $\text{Cs}_2\text{NaYCl}_6$ by Pawlik and Spaeth [7] revealed that the V_K centre (Cl_2^-) is thermally stable down to liquid nitrogen temperatures. At lower temperatures, x-ray irradiation produces an intrinsic electron-trapping center that was identified as a Jahn-Teller-distorted Y^{2+} defect. With respect to the bromide-elpasolites, a brief report on the scintillation properties of Ce^{3+} - doped $\text{Cs}_2\text{LiYBr}_6$ was published by Mishin *et al* [8].

* based on: E.V.D. van Loef, P. Dorenbos, C.W.E. van Eijk, K.W. Krämer, H.U. Güdel, J. Phys. Condens. Mat. 14 (2002) 8481.

7.2 Material

$\text{Cs}_2\text{LiYCl}_6$, $\text{Cs}_2\text{LiYCl}_6:0.5\% \text{Ce}^{3+}$, $\text{Cs}_2\text{LiYBr}_6$ and $\text{Cs}_2\text{LiYBr}_6:1\% \text{Ce}^{3+}$ single crystals were grown by the vertical Bridgman technique in silica ampoules under vacuum. The starting materials were prepared from CsCl/Br (Merck, 99.9%), Li_2CO_3 (Heraeus, 99.995%), Y_2O_3 (Johnson and Matthey, 99.999%) and CeO_2 (Johnson and Matthey, 99.99%) according to the ammonium halide method [9,10]. The crystals are hygroscopic and were sealed under helium atmosphere into small quartz ampoules to prevent hydration of the surface. The density of $\text{Cs}_2\text{LiYCl}_6$ and $\text{Cs}_2\text{LiYBr}_6$ is 3.31 and 4.15 g/cm^3 , respectively.

7.3 Results

7.3.1 X-ray excited optical luminescence

X-ray excited optical luminescence spectra of both pure $\text{Cs}_2\text{LiYCl}_6$ [6] and pure $\text{Cs}_2\text{LiYBr}_6$ at 100 K are shown in Fig. 1. $\text{Cs}_2\text{LiYCl}_6$ emits in a broad band, centred at 3.6 eV (FWHM = 1.1 eV). Additionally, a low intensity emission occurs between 2 and 3 eV. For several other elpasolites [4] and bromides [11,12] similar bands have been observed in this spectral range and were ascribed to emission from self-trapped excitons (STEs). In the case of $\text{Cs}_2\text{LiYBr}_6$, the emission spectrum is dominated by a single broad band at 3.6 eV (FWHM = 0.6 eV).

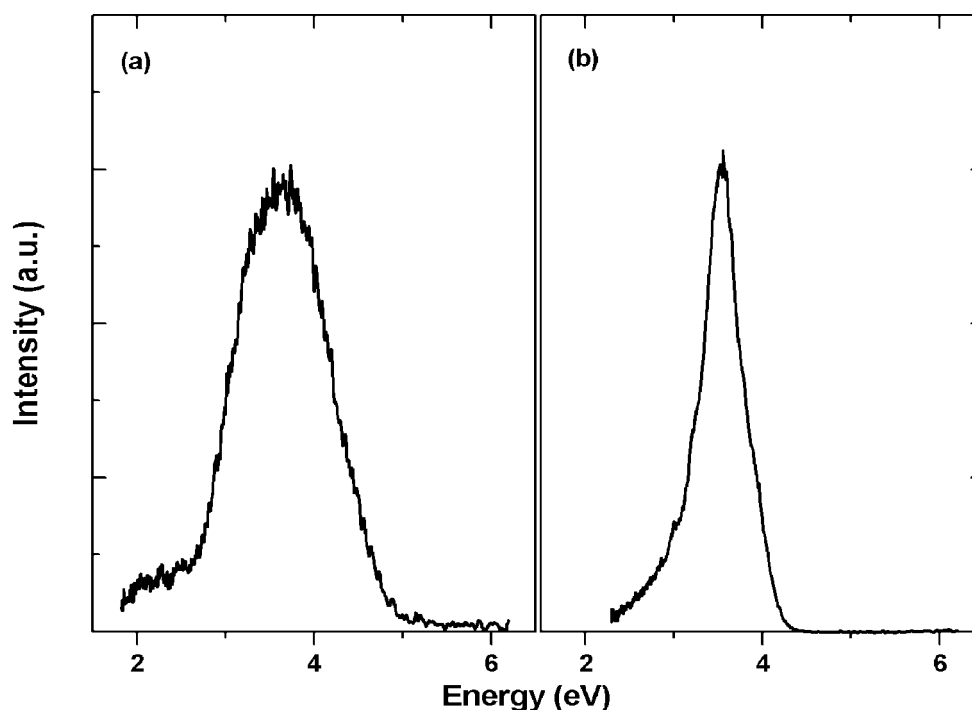


Fig.1. X-ray excited optical luminescence spectra of (a) $\text{Cs}_2\text{LiYCl}_6$ and (b) $\text{Cs}_2\text{LiYBr}_6$ at 100 K.

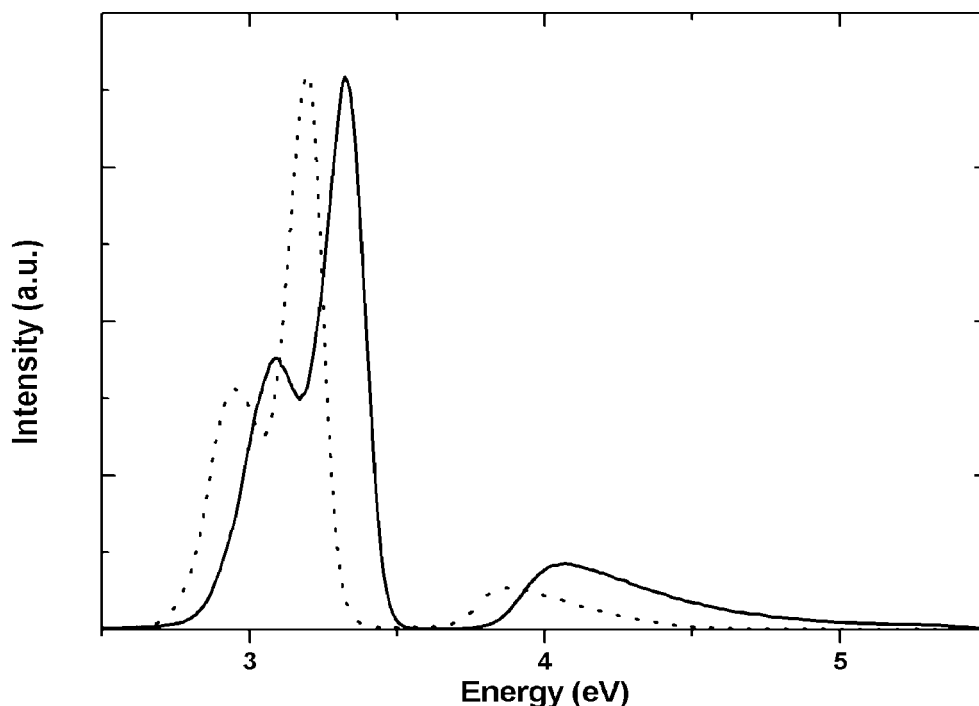


Fig. 2. X-ray excited optical luminescence spectra of $\text{Cs}_2\text{LiYCl}_6:\text{Ce}^{3+}$ (solid trace) and $\text{Cs}_2\text{LiYBr}_6:\text{Ce}^{3+}$ (dotted trace) at room temperature.

Figure 2 shows the x-ray excited optical luminescence spectra of $\text{Cs}_2\text{LiYCl}_6:\text{Ce}^{3+}$ [6] and $\text{Cs}_2\text{LiYBr}_6:\text{Ce}^{3+}$ [8] recorded at room temperature. The chloride spectrum (solid trace) is dominated by the characteristic doublet of the $5d \rightarrow 4f$ Ce^{3+} luminescence with maxima at 3.07 and 3.30 eV. The transitions from the lowest $5d^1$ excited state to the $^2\text{F}_{5/2}$ groundstate and the $^2\text{F}_{7/2}$ state of the $4f^1$ configuration are nicely resolved. The spin-orbit splitting between the ^2F states is 0.23 eV. The weak broad band around 4 eV is attributed to residual STE emission. The absence of luminescence between 3.5 and 3.8 eV is due to the absorption of STE emission by Ce^{3+} . For the bromide (dotted trace) the shape of the spectrum is very similar to that of the chloride. The luminescence maxima are observed at 2.93 eV and 3.19 eV. Again, the absence of luminescence between 3.3 eV and 3.6 eV is ascribed to the absorption of STE emission by Ce^{3+} .

The temperature dependence of the relative light yield under X-ray excitation is shown for pure $\text{Cs}_2\text{LiYCl}_6$ (solid trace) and $\text{Cs}_2\text{LiYBr}_6$ (dotted trace) in Fig. 3. For both compounds the light yield decreases with temperature due to the quenching of STE emission. Figure 4 shows the behaviour of the Ce^{3+} doped compounds $\text{Cs}_2\text{LiYCl}_6:\text{Ce}^{3+}$ (solid trace) and $\text{Cs}_2\text{LiYBr}_6:\text{Ce}^{3+}$ (dotted trace) which is distinctly different from that of the pure ones. Both traces show a maximum at 300 K and 200 K for the chloride and bromide, respectively.

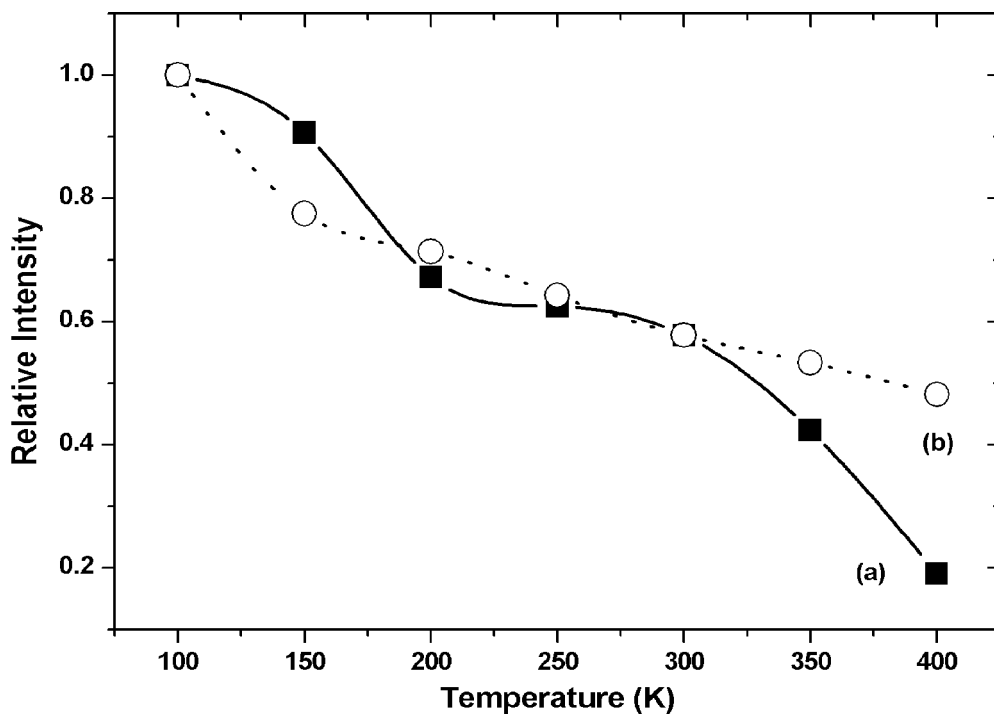


Fig. 3. Temperature dependence of the light yield of $\text{Cs}_2\text{LiYCl}_6$ (\blacksquare) and $\text{Cs}_2\text{LiYBr}_6$ (\circ) under X-ray excitation. The lines are drawn to guide the eye.

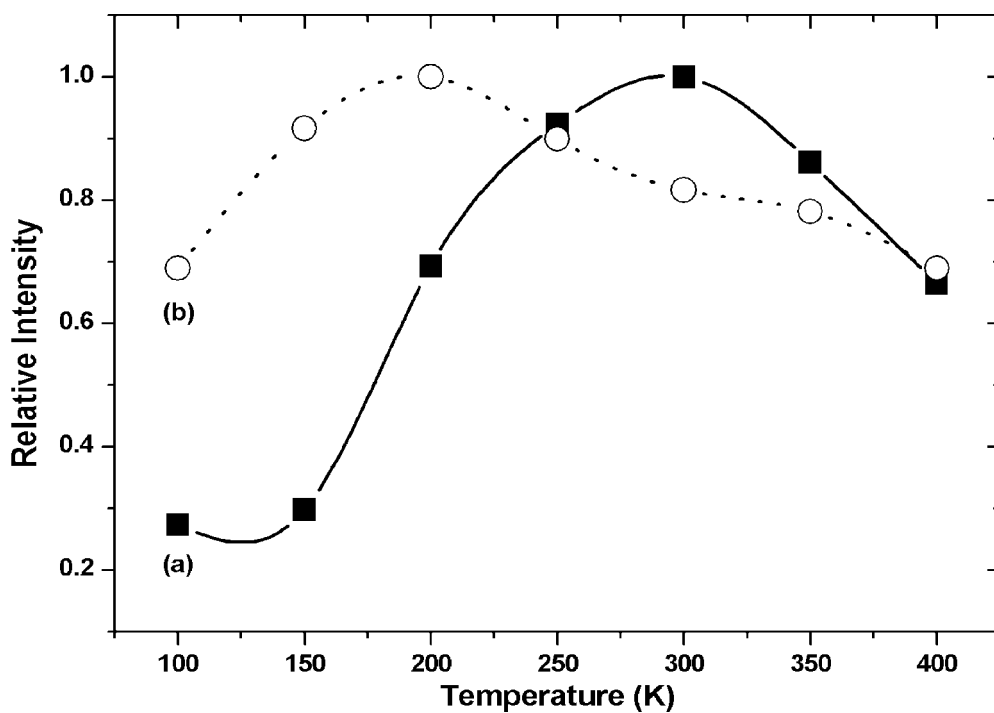


Fig. 4. Temperature dependence of the light yield of $\text{Cs}_2\text{LiYCl}_6:\text{Ce}^{3+}$ (\blacksquare) and $\text{Cs}_2\text{LiYBr}_6:\text{Ce}^{3+}$ (\circ) under X-ray excitation. The lines are drawn to guide the eye.

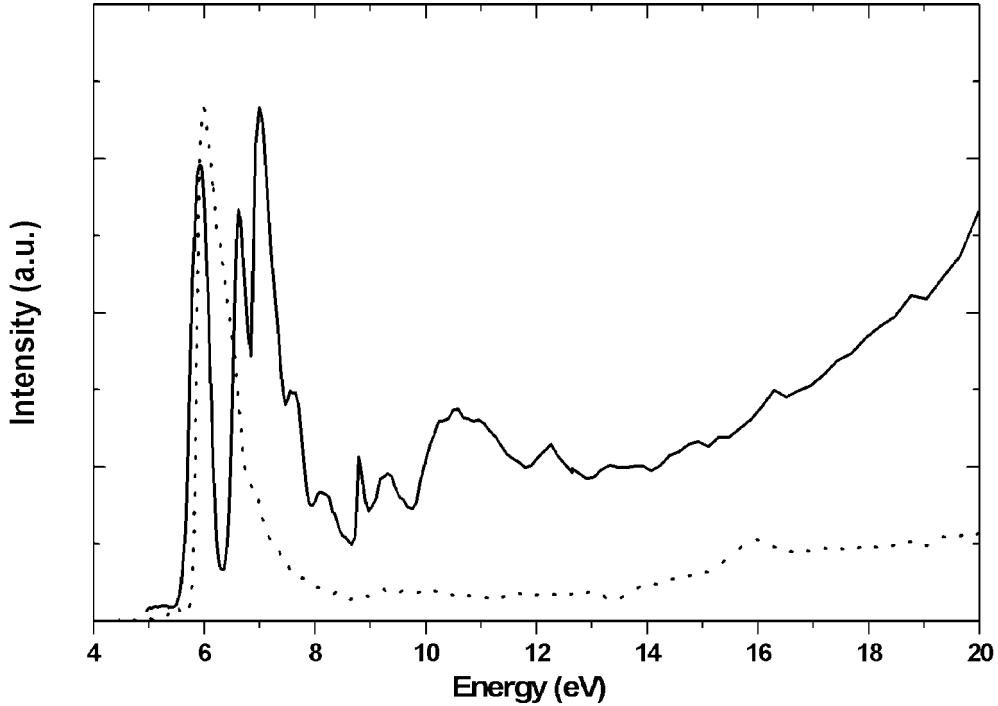


Fig. 5. Optical excitation spectra of $\text{Cs}_2\text{LiYCl}_6$ (solid trace) and $\text{Cs}_2\text{LiYBr}_6$ (dotted trace) at 10K, monitoring host lattice emission at 3.6 eV.

7.3.2 Optical excitation and emission

The optical excitation spectra of pure $\text{Cs}_2\text{LiYCl}_6$ and $\text{Cs}_2\text{LiYBr}_6$ at 10 K monitoring STE emission at 3.6 eV are depicted in Fig. 5. The excitation spectrum of $\text{Cs}_2\text{LiYCl}_6$ (solid trace) consists of a structured band with maxima at 5.9 eV, 6.6 eV and 7.0 eV. A much weaker band is observed near 10.6 eV. The intensity of the excitation spectrum gradually increases above 14 eV. A single band at 6.0 eV dominates the excitation spectrum of $\text{Cs}_2\text{LiYBr}_6$. If the low energy side of this peak is taken as the onset of the valence-to-conduction band transition, then the bandgap of $\text{Cs}_2\text{LiYBr}_6$ is about 5.7 eV.

Figure 6 shows the 10 K emission spectra of (a) $\text{Cs}_2\text{LiYCl}_6$ excited at (i) 5.9 eV, (ii) 7.0 eV, and (iii) 10.8 eV and (b) $\text{Cs}_2\text{LiYBr}_6$ excited at 6.0 eV. The emission spectrum of $\text{Cs}_2\text{LiYCl}_6$, under 5.9 eV excitation shows a band at 3.8 eV (FWHM = 0.4 eV) which is attributed to STE emission. At lower energy, near 2.8 eV, an additional weaker band can be distinguished (FWHM = 0.7 eV). Excitation at 6.6 eV or 7.0 eV yields a broad emission band at 3.6 eV similar to that shown in Figure 1(a). However, there is an additional sharp peak near 3.9 eV, which is probably due to ${}^6\text{P}_{7/2} \rightarrow {}^8\text{S}_{7/2}$ emission of a Gd^{3+} impurity. Excitation into the low-intensity band near 10.6 eV gives rise to another emission at 4.1 eV (FWHM = 0.6 eV). The emission spectrum of $\text{Cs}_2\text{LiYBr}_6$ consists of a single band at 3.4 eV (FWHM = 0.6 eV).

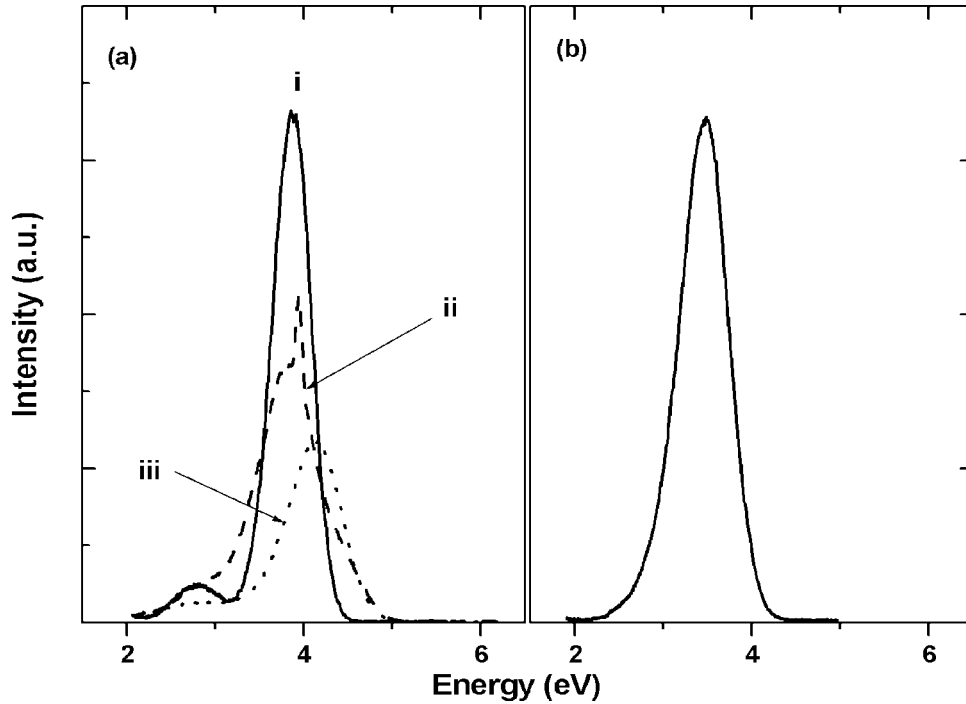


Fig. 6. Optical emission spectra of (a) $\text{Cs}_2\text{LiYCl}_6$, excited at (i) 5.9 eV, (ii) 7.0 eV and (iii) 10.8 eV, and (b) $\text{Cs}_2\text{LiYBr}_6$, excited at 6.0 eV. All spectra were recorded at 10K.

Time-resolved excitation spectra of $\text{Cs}_2\text{LiYCl}_6$ at 194 K monitoring the host lattice emission at 4.5 eV are shown in Fig. 7. Between 14 and 24 eV an intense broad band is observed in the 13 ns gated excitation spectrum (dotted trace). This band is neither present in the 81 ns gated excitation spectrum (solid trace), nor in the excitation spectra of the 3.6 eV and 4.1 eV emission bands (see Fig. 5). Apparently, the band corresponds to an excited state with a short lifetime, whereas excitation into the peaks at 5.9 eV and 6.6 eV leads to luminescence with a long decay time. A similar intense, broad excitation was observed by Rodnyi et al. for pure and Ce^{3+} doped $\text{Cs}_2\text{LiLaCl}_6$ [5]. They ascribed it to an excitation of 5p Cs levels. The peak observed at 7.0 eV in the excitation spectrum of $\text{Cs}_2\text{LiYCl}_6$ monitoring STE emission at 3.6 eV (Fig. 5, solid trace) is not observed in the time-resolved excitation spectrum (Fig. 7). It seems that the two peaks at 5.9 eV and 6.6 eV have a different origin from the peak at 7.0 eV. The former two are probably due to direct excitation of STEs, whereas the latter is likely the onset of a band-to-band transition at 6.8 eV.

Time-resolved emission spectra of $\text{Cs}_2\text{LiYCl}_6$ excited at 17.2 eV are shown in Figure 8 for 10 K and 200 K. The 13 ns gated spectrum (dotted trace) at 200 K shows a broad structured band between 3 eV and 6 eV. It is probably composed of two different emissions with maxima near 3.7 eV and 4.5 eV. Those emissions are completely absent in the 81 ns gated emission spectrum (solid trace) and ascribed to core-valence (CV) luminescence [5]. At 10 K, the intensity of the broad structured band decreases in favour of a 0.6 eV wide emission with a maximum near 4.1 eV. Its shape deviates from a Gaussian form. It is only present in the 81 ns gated spectra between 10 K and 100 K and probably due to some type of STE luminescence.

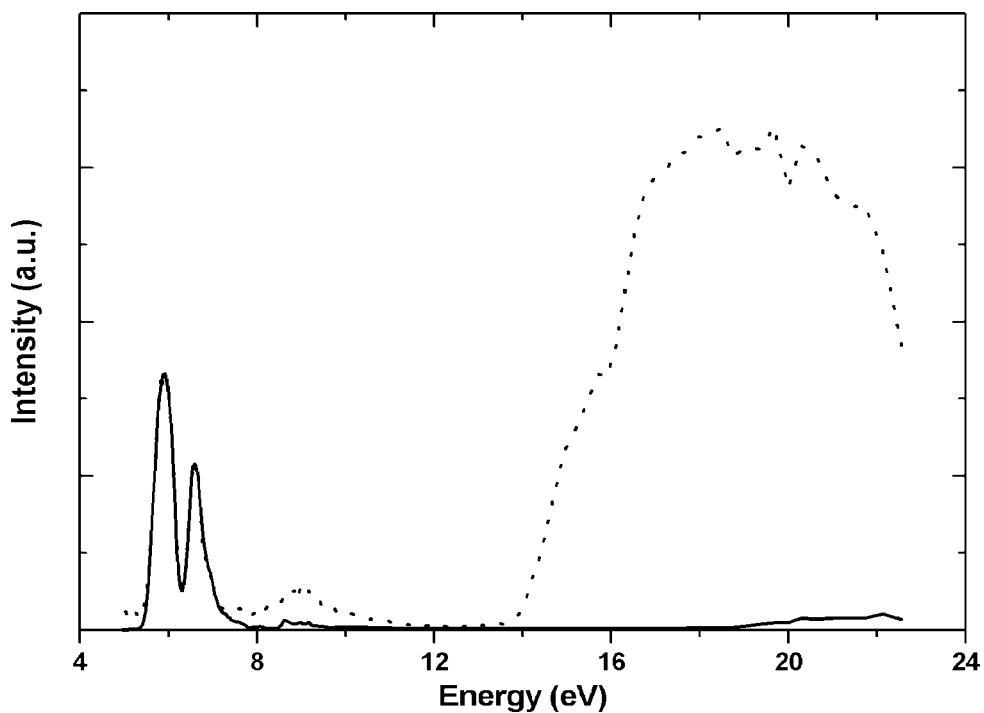


Fig. 7. Time-resolved optical excitation spectra of $\text{Cs}_2\text{LiYCl}_6$ at 194K, monitoring host lattice emission at 4.5 eV. The dotted curve represent the 13 ns gated excitation spectrum, whereas the solid curve represent the integral spectrum.

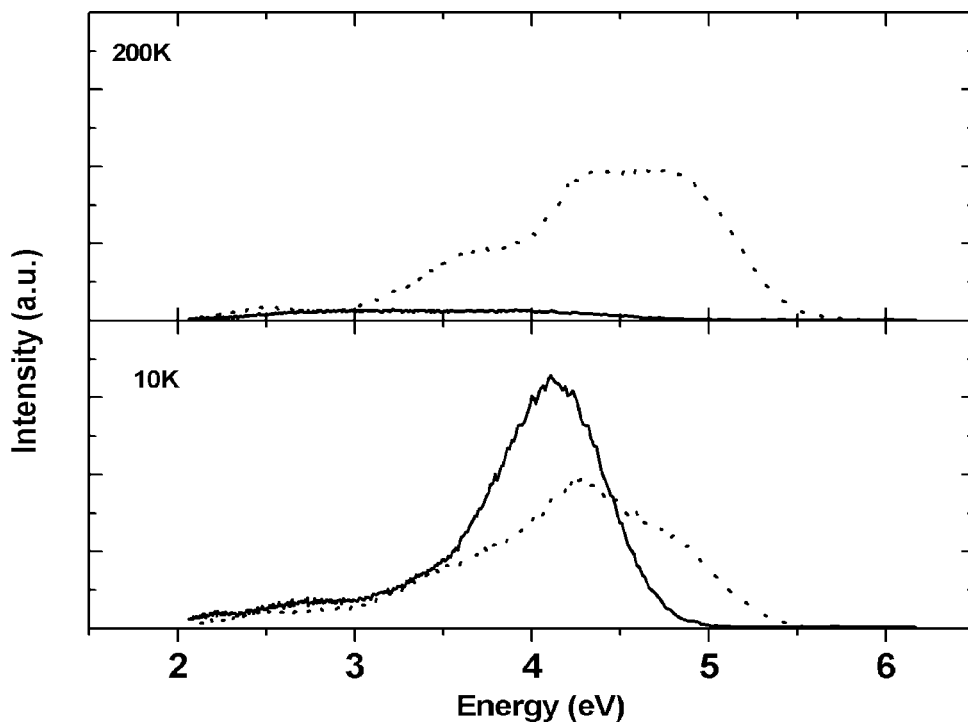


Fig. 8. Time-resolved optical emission spectra of $\text{Cs}_2\text{LiYCl}_6$ at 10 K and 200 K, excited at 17.2 eV. The dotted curves represent the 13 ns gated emission spectra, whereas the solid curves represent the 81 ns gated emission spectra.

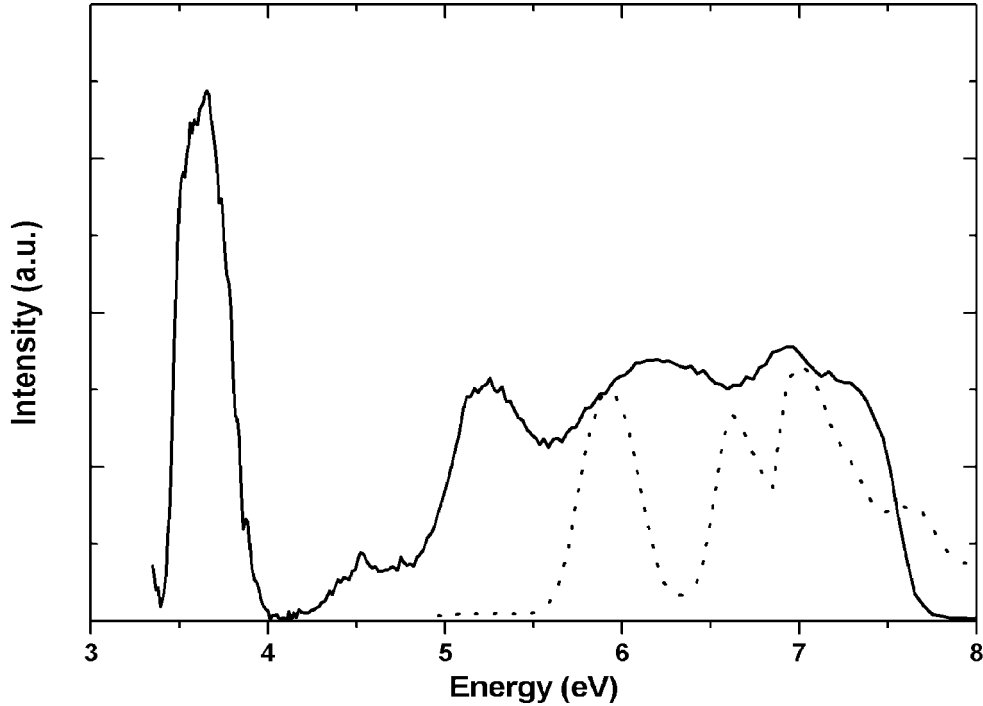


Fig. 9. Excitation spectrum of $\text{Cs}_2\text{LiYCl}_6:\text{Ce}^{3+}$ monitoring Ce^{3+} emission, recorded at 130 K. The dotted trace represents the excitation spectrum of pure $\text{Cs}_2\text{LiYCl}_6$.

Figure 9 shows the excitation spectrum of $\text{Cs}_2\text{LiYCl}_6:\text{Ce}^{3+}$ [6] at 130 K monitoring the Ce^{3+} emission at 3.1 eV (solid line). For comparison pure $\text{Cs}_2\text{LiYCl}_6$ (dotted line), is shown as well. The $\text{Cs}_2\text{LiYCl}_6:\text{Ce}^{3+}$ spectrum is dominated by the intense band of the $\text{Ce}^{3+} 4f(^2F_{5/2}) \rightarrow 5d(t_{2g})$ transitions between 3.4 eV and 4.0 eV. Four further broad bands are observed near 4.5 eV, 5.3 eV, 6.2 eV and 6.9 eV. Excitation near 4.5 eV and 5.3 eV predominantly results in Ce^{3+} emission, whereas excitation around 6.2 eV and 6.9 eV yields both Ce^{3+} and STE emission. Since the bands near 4.5 eV and 5.3 eV are completely absent in the optical excitation spectrum of pure $\text{Cs}_2\text{LiYCl}_6$, they are both ascribed to Ce^{3+} transitions. That near 4.5 eV might be due to a Ce^{3+} centre of lower symmetry [8] caused for example by aggregation of Ce^{3+} ions. The band near 5.3 eV is ascribed to $\text{Ce}^{3+} 4f(^2F_{5/2}) \rightarrow 5d(e_g)$ transitions. Accordingly, the $5d(t_{2g} - e_g)$ crystal field splitting is $\epsilon_{\text{cfs}} = 15,300 \pm 2,400 \text{ cm}^{-1}$, which is relatively small compared to numbers for chloro-elpasolites reported by Dorenbos [13]. Nevertheless, it compares well with the results for $\text{Cs}_2\text{NaLuCl}_6:\text{Ce}^{3+}$ [4] and $\text{Cs}_2\text{LiLaCl}_6:\text{Ce}^{3+}$ [5]. The bands near 6.2 eV and 6.9 eV are due to direct STE excitation and band-to-band transitions, respectively. However, $\text{Cs}_2\text{LiYCl}_6:\text{Ce}^{3+}$ is also efficiently excited in the region between 5.3 and 6.2 eV. Possibly, it is due to the increase in temperature which broadens the excitation bands considerably, but it can also be due to $\text{Ce}^{3+} 4f \rightarrow 6s$ transitions. At the moment we cannot discriminate between the two.

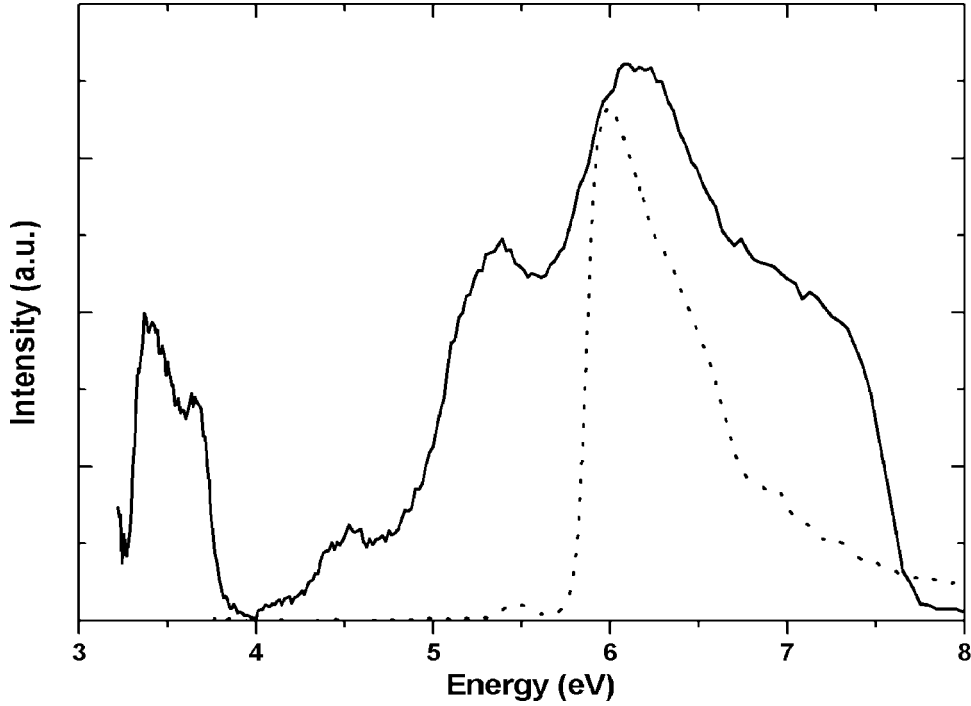


Fig. 10. Excitation spectrum of $\text{Cs}_2\text{LiYBr}_6:\text{Ce}^{3+}$ monitoring Ce^{3+} emission, recorded at 130 K. The dotted trace represents the excitation spectrum of pure $\text{Cs}_2\text{LiYBr}_6$.

The excitation spectrum of $\text{Cs}_2\text{LiYBr}_6:\text{Ce}^{3+}$ at 130 K monitoring the Ce^{3+} emission at 3.0 eV is shown in Fig. 10 (solid trace). The $\text{Ce}^{3+} 4f \rightarrow 5d(t_{2g})$ transitions of the bromide are found at lower energies than for the chloride, i.e. between 3.2 and 3.9 eV. The $\text{Ce}^{3+} 4f \rightarrow 5d(e_g)$ transition is located at 5.3 eV which results in a $5d(t_{2g} - e_g)$ crystal field splitting of $\epsilon_{\text{cfs}} = 17,300 \pm 1,300 \text{ cm}^{-1}$. Similar values for the energy and the $5d$ crystal field splitting of Ce^{3+} have been reported for other bromides [11]. It is remarkable that for $\text{Cs}_2\text{LiYCl}_6:\text{Ce}^{3+}$ the $\text{Ce}^{3+} 4f \rightarrow 5d(t_{2g})$ transitions are more intense than the band-to-band transitions between 6 and 7 eV, whereas it is the other way around for the bromide.

7.3.3 Scintillation decay

Figure 11 shows the scintillation decay time spectra of (a) $\text{Cs}_2\text{LiYCl}_6$, (b) $\text{Cs}_2\text{LiYCl}_6:\text{Ce}^{3+}$, (c) $\text{Cs}_2\text{LiYBr}_6$, and (d) $\text{Cs}_2\text{LiYBr}_6:\text{Ce}^{3+}$ at room temperature under ^{137}Cs gamma-ray excitation. The insets in Figs. 11a and b show the decay time spectra under pulsed X-ray excitation on an extended time scale for $\text{Cs}_2\text{LiYCl}_6$ and $\text{Cs}_2\text{LiYCl}_6:\text{Ce}^{3+}$, respectively.

The decay curve of $\text{Cs}_2\text{LiYCl}_6$ is characterised by two components: a fast one with a lifetime of $2 \pm 1 \text{ ns}$, characteristic for CV luminescence in Cs-based chlorides [14,15] and a slow component with a decay time of $6.9 \pm 0.1 \mu\text{s}$ due to STE emission. Both components are also present in the $\text{Cs}_2\text{LiYCl}_6:\text{Ce}^{3+}$ spectra but the slow component has a shorter life time of $4.3 \pm 0.1 \mu\text{s}$ probably due to both STE and Ce^{3+} emission. However, there are further contributions that can be modelled by a non-exponential decay with a lifetime of about 400 ns.

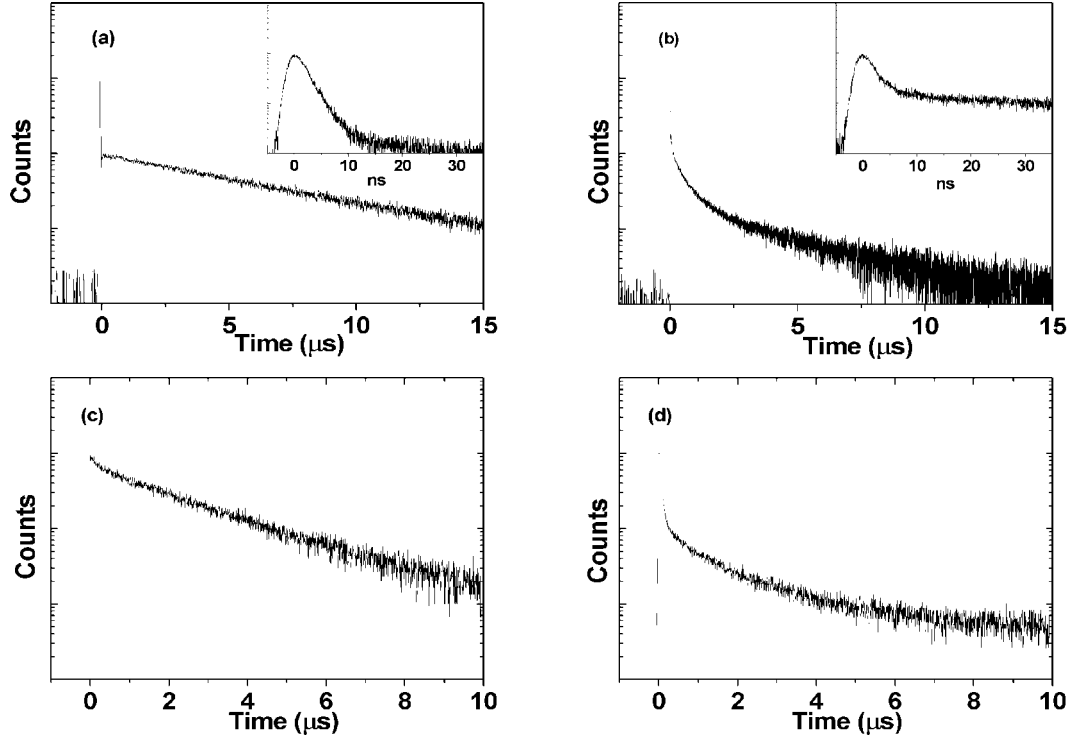


Fig. 11. Scintillation decay time spectra of (a) $\text{Cs}_2\text{LiYCl}_6$, (b) $\text{Cs}_2\text{LiYCl}_6:\text{Ce}^{3+}$, (c) $\text{Cs}_2\text{LiYBr}_6$ and (d) $\text{Cs}_2\text{LiYBr}_6:\text{Ce}^{3+}$ at room temperature under Cs-137 gamma-ray excitation.

The only compound that seems to have a single exponential decay is $\text{Cs}_2\text{LiYBr}_6$. Its luminescence has a lifetime of $2.4 \pm 0.2 \mu\text{s}$. The decay curve of $\text{Cs}_2\text{LiYBr}_6:\text{Ce}^{3+}$ can be described by three decay components. A relatively fast component of $65 \pm 5 \text{ ns}$, typical for Ce^{3+} emission, an intermediate, non-exponential one of $1.1 \pm 0.1 \mu\text{s}$ and a slow one of $9 \pm 1 \mu\text{s}$. The latter are probably due to Ce^{3+} and STE emission, respectively. Neither bromide shows a fast component due to CV luminescence.

In Fig. 12 the decay time τ of the STE in (a) $\text{Cs}_2\text{LiYCl}_6$ and (b) $\text{Cs}_2\text{LiYBr}_6$ is presented as function of $1/T$. The samples were excited at 5.9 eV and 6.0 eV respectively, monitoring all emissions. The dotted curves show model calculations according to

$$\frac{1}{\tau} = \frac{1}{\tau_R} + \frac{1}{\tau_t} \exp\left(-\frac{\Delta E}{kT}\right) \quad (2)$$

where $1/\tau_R$ and $(1/\tau_t)\exp(-\Delta E/kT)$ are the probabilities of radiative and thermal decay, respectively, ΔE is the activation energy for thermal decay, and k the Boltzmann constant. From a fit to equation 2 values for ΔE , τ_R , and τ_t were obtained. They are summarised in Table I.

Table I. The activation energy for thermal decay, ΔE , the lifetime of radiative decay, τ_R , and thermal decay, τ_t , for self-trapped excitons in $\text{Cs}_2\text{LiYCl}_6$ and $\text{Cs}_2\text{LiYBr}_6$.

Compound	ΔE (eV)	τ_t (ps)	τ_R (μs)
$\text{Cs}_2\text{LiYCl}_6$	0.10 ± 0.01	-	33 ± 5
$\text{Cs}_2\text{LiYBr}_6$	0.30 ± 0.03	150 ± 50	4 ± 1

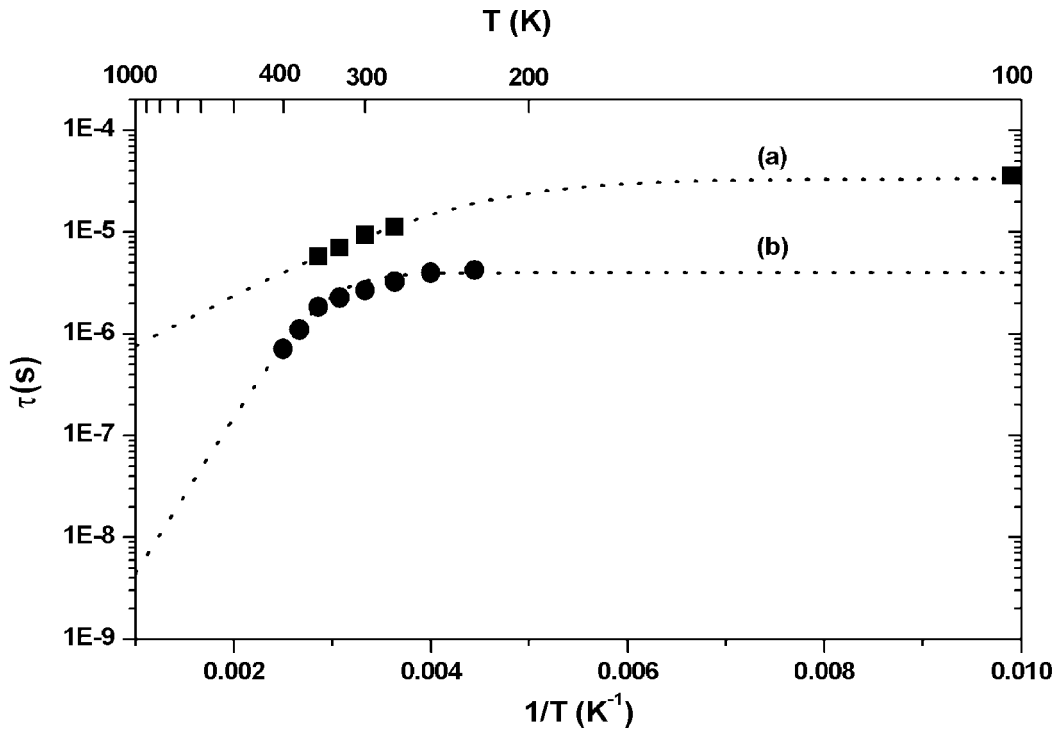


Fig. 12. Decay time of the STE, $[\tau]$, in (a) $\text{Cs}_2\text{LiYCl}_6$ and (b) $\text{Cs}_2\text{LiYBr}_6$ as function of temperature.

The activation energies for thermal decay ΔE are 100 ± 10 meV and 300 ± 30 meV, for $\text{Cs}_2\text{LiYCl}_6$ and $\text{Cs}_2\text{LiYBr}_6$, respectively. The lifetime of radiative decay, τ_R of the STE in $\text{Cs}_2\text{LiYBr}_6$ is significantly shorter than in $\text{Cs}_2\text{LiYCl}_6$.

7.4 Discussion

Pure $\text{Cs}_2\text{LiYCl}_6$ shows a broad structured emission band between 3 eV and 6 eV (see Figure 6), with a fast decay time ($\tau \approx 10^{-9}$ s) due to CV luminescence. A model for CV transitions, according to which the energy position and width of the CV luminescence bands depend on the position and width of the 3p Cl valence band and the 5p Cs core band, can be used to rationalise the situation in the band structure picture shown in Fig. 13. The energies of the bands were calculated using the GAUSSIAN98 (G98) program [16]. The widths of the 3p Cl and 5p Cs bands were taken to be 3 eV and 4 eV [3], respectively, and the band gap energy $E_g = 6.8$ eV (see Figure 3).

In contrast to the chloride, $\text{Cs}_2\text{LiYBr}_6$ does not show CV luminescence. Apparently, the condition for the detection of CV band transitions [1] is not met in $\text{Cs}_2\text{LiYBr}_6$. Probably because of the relatively high probability of the competing Auger-decay [1]. This assumption is supported by the fact that the bandgap of $\text{Cs}_2\text{LiYBr}_6$ is smaller than for $\text{Cs}_2\text{LiYCl}_6$, 5.7 eV and 6.8 eV, respectively. Hence, CV luminescence is more easily quenched in $\text{Cs}_2\text{LiYBr}_6$ than in $\text{Cs}_2\text{LiYCl}_6$, see Figure 13.

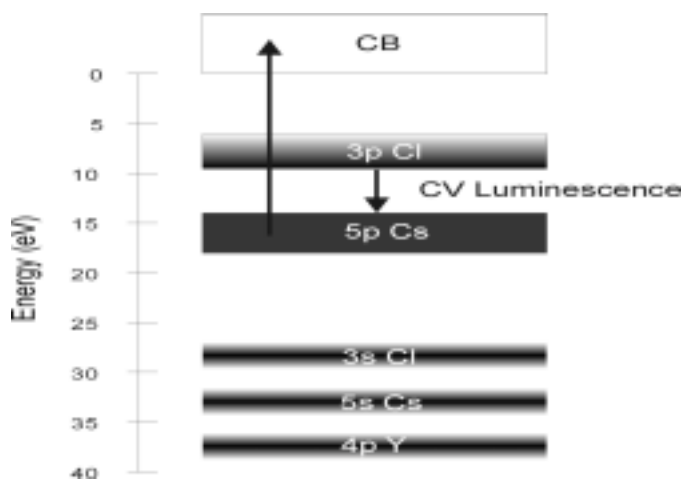


Fig. 13. Energy band scheme of $\text{Cs}_2\text{LiYCl}_6$. The large arrow represents the 5p Cs core excitation, whereas the smaller arrow represents CV luminescence. In the case of $\text{Cs}_2\text{LiYBr}_6$ no CV luminescence was observed.

Unfortunately, the contribution of CV luminescence to the total light yield is relatively small in $\text{Cs}_2\text{LiYCl}_6$. The major contribution to the total light yield is STE emission. In both $\text{Cs}_2\text{LiYCl}_6$ and $\text{Cs}_2\text{LiYBr}_6$, STE emission is observed with a long life time in the order of 1 – 10 μs and a large activation energy for thermal decay of the order of 100 – 300 meV. For most alkaline-earth halides [17] and for KI [18], [19], an equally large activation energy for thermal decay was reported, but most other alkali halides show STE emission with a decay time and activation energy for thermal decay being an order of magnitude smaller. The smaller lifetime of radiative decay of the STE in the bromide is due to the stronger spin-orbit coupling of the groundstate [20] of the STE. Additionally, the spin-orbit splitting of the halogen p valence band increases as the halogen atom becomes heavier [21]. Since $\text{Cs}_2\text{LiYCl}_6$ and $\text{Cs}_2\text{LiYBr}_6$ have the same crystal structure, the valence band in the bromide is broader than the valence band in the chloride. Consequently, free holes will move more easily through the valence band in the case of $\text{Cs}_2\text{LiYBr}_6$.

Although the energy of the STE luminescence band overlaps with $\text{Ce}^{3+} 4f \rightarrow 5d$ transitions, in both $\text{Cs}_2\text{LiYCl}_6:\text{Ce}^{3+}$ and $\text{Cs}_2\text{LiYBr}_6:\text{Ce}^{3+}$ (compare Fig. 1 with Fig. 9 and 10), there is still some STE emission present in the room temperature x-ray excited optical luminescence spectra (see Fig. 2). Apparently, energy transfer from the STE to Ce^{3+} centres is inefficient and occurs to a large extent radiatively.

Energy transfer due to absorption of STE emission by Ce^{3+} ions results in Ce^{3+} emission and a dip in the STE emission band at the position of the Ce^{3+} absorption band (see Fig. 2). In this case, the effective lifetime of the Ce^{3+} emission equals the lifetime of the STE. It is expected that for this type of energy transfer the luminescence intensity as function of temperature decreases with increasing temperature due to the quenching of STE luminescence. However, the model described above does not explain the bell-shaped curves of the X-ray excited optical luminescence spectra as function of temperature shown in Fig. 4. That is, one needs to explain the *increase* in the relative light yield, from 100 to 300 K and from 100 to 200 K for $\text{Cs}_2\text{LiYCl}_6:\text{Ce}^{3+}$ and $\text{Cs}_2\text{LiYBr}_6:\text{Ce}^{3+}$, respectively, and subsequently the *decrease* in the relative light yield for both $\text{Cs}_2\text{LiYCl}_6:\text{Ce}^{3+}$ and $\text{Cs}_2\text{LiYBr}_6:\text{Ce}^{3+}$ up to 400 K.

Interestingly, the bell-shaped curves have been observed before [22,23] and were attributed to the production of F centres. As an example, the production of F centres in KCl at different temperatures [24] is shown in Fig. 14.

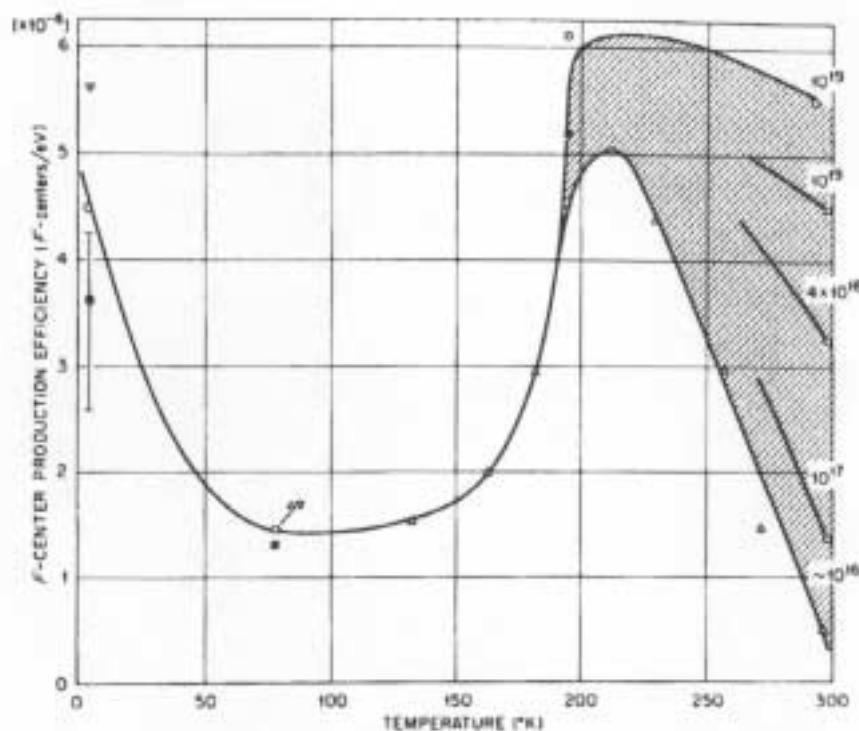


Fig. 14. Radiation production efficiency for F centres in KCl at different temperatures (reproduced from [24]). The numbers above the room temperature points give the dose rate in eV absorbed per cm^3 per sec.

Vilu and Elango [25] compared the temperature dependence of the production efficiency of F centres in a number of alkali halides with the temperature dependence of recombination luminescence and thermoluminescence spectra. Their results show that the bell-shaped curve shown in Fig. 14 is also present in NaCl, KBr, and KI. Moreover, the optimum temperature at which the efficiency of the F centre formation is maximal decreases along the series $\text{Cl} \rightarrow \text{Br} \rightarrow \text{I}$, which is in good agreement with the temperature at which localisation and self-trapping of holes takes place in the crystal lattice. Also the X-ray excited optical luminescence spectra as function of temperature shown in Fig. 4 shows this trend with halide ion. Keeping this in mind, we propose that *energy transfer by binary electron hole diffusion* is the dominant scintillation mechanism in the elpasolites and the following mechanisms are operation when the temperature increases:

A. $1.2 \text{ K} < T < 100 \text{ K}$

At temperatures between 1.2 and 100 K, the holes are trapped in the lattice and form immobile V_K centres. Whether the electron is actually bound to an Y^{3+} ion, or forming a self-trapped exciton with the localised hole is not known. Recombination with the electron predominately gives rise to STE luminescence. Alternatively, it is also possible that the holes are trapped in the lattice and form H centres. In this case, the electrons occupy anion vacancies and form F centres. If some of the H centres are mobile, recombination with the electron also leads to STE luminescence. When the temperature increases, more and more H centres will become mobile and, consequently, the number of F centres decreases (see Fig. 14).

B. $100\text{ K} < T < 200\text{ K}^\dagger$

At liquid nitrogen temperatures, additional holes are created by the decay of the V_K centres that are captured by Ce^{3+} . Free electrons subsequently recombine with the Ce^{4+} centres and Ce^{3+} emission is observed. The Ce^{3+} luminescence efficiency increases with temperature because the decay of the V_K centres increases with temperature. Alternatively, both F centres and H centres may be stabilised next to Ce^{3+} . Recombination of the electron and hole excite Ce^{3+} and Ce^{3+} emission is observed. The Ce^{3+} luminescence efficiency increases with temperature because the number of stabilised F centres and H centres increases (see Fig. 14).

C. $T \sim 200\text{ K}^\dagger$

The maximum intensity of Ce^{3+} luminescence in $\text{Cs}_2\text{LiYCl}_6:\text{Ce}^{3+}$ and $\text{Cs}_2\text{LiYBr}_6:\text{Ce}^{3+}$ is found at 300 K and 200 K, respectively (see Fig. 4). Probably, the decay of the trapped holes in the chloride takes place at higher temperatures than in the bromide. We already referred to the work of Vilu *et al.* [25].

D. $T > 200\text{ K}^\dagger$

At elevated temperatures, the Ce^{3+} luminescence efficiency decreases due to the quenching of Ce^{3+} emission. The majority of the electrons and holes form an (impurity perturbed) STE which is relatively stable in both pure and Ce^{3+} doped $\text{Cs}_2\text{LiYCl}_6$ and $\text{Cs}_2\text{LiYBr}_6$. Assuming that in both cases free electrons move faster than free holes, fast Ce^{3+} luminescence is observed if the diffusion rate of the holes is of the order of magnitude of the time needed to create an STE. Since this process is dependent on Ce concentration, it is expected that increasing the Ce^{3+} concentration will lead to an (slight) increase in the contribution of the short decay component to the light yield.

7.5 Conclusions

The optical and scintillation properties of pure and Ce^{3+} -doped Cs_2LiYX_6 ($X = \text{Cl}, \text{Br}$) have been presented. In these systems, *energy transfer by binary electron-hole diffusion* is the dominant scintillation mechanism. Additionally, core-valence (CV) luminescence is present in the pure chloride. The anion does not seem to influence the scintillation mechanism significantly apart from the mobility of the holes. Therefore, we expect that the same scintillation mechanism is dominant in the iodide and other variants: $\text{Cs}_2\text{AYX}_6:\text{Ce}^{3+}$ ($A = \text{Li}, \text{Na}, \text{K}; X = \text{Cl}, \text{Br}, \text{I}$). The lifetime of STE luminescence tends to decrease from Cl to Br, due to the larger spin-orbit coupling in the bromide. It is expected that in the iodide, the lifetime of the STE is even shorter.

[†] For the chloride this value is about 300 K, i.e. the maximum of the Ce^{3+} luminescence efficiency.

References

- ¹ P.A. Rodnyi, *Sov. Phys. – Solid State* 34 (1992) 1053.
- ² N.N. Ershov, N.G. Zakharov, P.A. Rodnyi, *Opt. Spectrosc.* 53 (1982) 51.
- ³ A.S. Voloshinovskii, A.G. Dimitriev, V.B. Mikhailik, P.A. Rodnyi, *Sov. Phys. – Solid State* 34 (1992) 1998.
- ⁴ J.C. van't Spijker, P. Dorenbos, C.W.E. van Eijk, M.S. Wickleder, H.U. Güdel, *J. Lumin.* 72-74 (1997) 786.
- ⁵ P.A. Rodnyi, V.B. Mikhailik, G.B. Stryganyuk, A.S. Voloshinovskii, C.W.E. van Eijk, G.F. Zimmerer, *J. Lumin.* 86 (2000) 161.
- ⁶ C.M. Combes, P. Dorenbos, C.W.E. van Eijk, K.W. Krämer, H.U. Güdel, *J. Lumin.* 82 (1999) 299.
- ⁷ Th. Pawlik, J-M. Spaeth, *J. Phys.: Condens. Matter* 9 (1997) 8737.
- ⁸ A.N. Mishin, P.A. Rodnyi, A.V. Sidorenko, A.S. Voloshinovskii, P. Dorenbos, *Proc. SPIE* 4348 (2001) 47.
- ⁹ J.B. Reed, B.S. Hopkins, L.F. Audrieth, *Inorg. Synth.* 1 (1936) 28.
- ¹⁰ G. Meyer, *Inorg. Synth.* 25 (1989) 146.
- ¹¹ P. Dorenbos, J.C. van't Spijker, O.W.V. Frijns, C.W.E. van Eijk, K. Krämer, H.U. Güdel, A. Ellens, *Nucl. Instr. Meth. Phys. Res. B* 132 (1997) 728.
- ¹² O. Guillot-Noël, J.C. van't Spijker, J.T.M. de Haas, P. Dorenbos, C.W.E. van Eijk, K.W. Krämer, H.U. Güdel, *IEEE Trans. Nucl. Sci.* 46 (1999) 1274.
- ¹³ P. Dorenbos, *Phys. Rev. B* 62 (2000) 15650.
- ¹⁴ A.S. Voloshinovskii, V.B. Mikhailik, Ya. O. Struk, P.A. Rodnyi, C.W.E. van Eijk, G. Zimmerer, *J. Lumin.* 79 (1998) 115.
- ¹⁵ V.B. Mikhailik, A.S. Voloshinovskii, V. Kisand, S. Vielhauer, *Phys. Stat. Sol. B* 212 (1999) 367.
- ¹⁶ J.M. Frisch *et al.*, GAUSSIAN98 (REVISION A 1) (Pittsburgh, PA: Gaussian).
- ¹⁷ P. Dorenbos, P. Visser, R. Dool, L. Andriessen, C.W.E. van Eijk, *J. Phys.: Condens. Matter* 4 (1992) 5281.
- ¹⁸ D. Pooley, W.A. Runciman, *J. Phys. C.: Solid State Phys.* 3 (1970) 1815.
- ¹⁹ I. M. Blair, D. Pooley, S. Smith, *J. Phys. C.: Solid State Phys.* 5 (1972) 1537.
- ²⁰ K.S. Song, R.T. Williams, "Self-Trapped Excitons", Springer Series on Solid State Sciences no. 105, Ed. M. Cardona, New York, 1993, p. 149.
- ²¹ S. Satphathy, *Phys. Rev. B* 33 (1986) 8706.
- ²² J.D. Comins, P.T. Wedepohl, *Solid St. Commun.* 4 (1966) 537.
- ²³ E. Sonder, *Phys. Rev. B* 2 (10) (1970) 4189.
- ²⁴ E. Sonder, W.A. Sibley, "Point Defects in Solids", J.H. Crawford, L. M. Slifkin (Eds.), Plenum Press, New York, 1972, p. 258.
- ²⁵ R.O. Vilu, M.A. Elango, *Sov. Phys. - Solid State* 7(12) (1966) 2967.

8. The lutetium halides - $\text{LuX}_3:\text{Ce}^{3+}$ ($X = \text{Cl}, \text{Br}$)*

8.1 Introduction

In the previous chapter, we have presented the optical and scintillation properties of the elpasolites - $\text{Cs}_2\text{LiYX}_6:\text{Ce}^{3+}$ ($X = \text{Cl}, \text{Br}$). It was proposed that *energy transfer by binary electron hole recombination* be the dominant scintillation mechanism in these materials. Although self-trapped exciton (STE) emission had been observed, both at liquid nitrogen temperatures and at room temperature, *STE diffusion* did not play a significant role.

In this chapter, we discuss the properties and mechanism of scintillation in $\text{LuCl}_3:\text{Ce}^{3+}$ and $\text{LuBr}_3:\text{Ce}^{3+}$ crystals. Some of the properties of $\text{LuCl}_3:\text{Ce}^{3+}$ and $\text{LuBr}_3:\text{Ce}^{3+}$ have already been reported [1]. In this work, the scintillation properties of $\text{LuCl}_3:2\%, 4\%, 10\% \text{Ce}^{3+}$, $\text{LuBr}_3:2.5\%$ and $8\% \text{Ce}^{3+}$ are also presented. Additionally a scintillation mechanism for both $\text{LuCl}_3:\text{Ce}^{3+}$ and $\text{LuBr}_3:\text{Ce}^{3+}$ is proposed and discussed. It is shown that at room temperature, *energy transfer by binary electron hole diffusion* is the dominant mechanism in these materials. At lower irradiation temperatures, V_K diffusion is probably more important.

8.2 Material

Single crystals of LuCl_3 and LuBr_3 doped with different Ce concentrations were grown by the Bridgman technique using a static vertical silica ampoule and a moving furnace. Starting materials were prepared according to the ammonium halide method [2],[3] from Lu_2O_3 (Materials Technology International, > 99.995%), CeO_2 (Heraeus, 99.999%), $\text{NH}_4\text{Cl/Br}$ (Merck, reinst) and HCl/Br (Merck, pro-analysi). The Ce concentration was determined by Induction Coupled Plasma Spectroscopy (ICPS). LuCl_3 and LuBr_3 crystallise in the AlCl_3 and BiI_3 type structure with space group $C 2/m$ (no. 12) [4] and $R-3$ (no. 148) [5], respectively. Both structures are layered. Based on structure and lattice parameters, LuCl_3 and LuBr_3 have a calculated density of 4.00 g/cm^3 and 5.17 g/cm^3 , respectively.

8.3 Results

8.3.1 X-ray excited optical luminescence

X-ray excited optical luminescence spectra of pure LuCl_3 , $\text{LuCl}_3:2\% \text{Ce}^{3+}$, $\text{LuBr}_3:0.021\%, 2.5\%$, and $8\% \text{Ce}^{3+}$ are shown in Fig. 1. The spectra of pure LuCl_3 , $\text{LuCl}_3:0.45\% \text{Ce}^{3+}$, $\text{LuBr}_3:0.021\%, 0.46\%$, and $0.76\% \text{Ce}^{3+}$ have already been published by Guillot-Noël *et al.* [1]. For pure LuCl_3 , the X-ray excited optical luminescence spectrum at 140 K (see inset) consists of a broad structured band peaking at 386 nm. It is attributed to self-trapped exciton (STE) luminescence. Also

* based on: E.V.D. van Loef, P. Dorenbos, C.W.E. van Eijk, K.W. Krämer, H.U. Güdel, Nucl. Instr. Meth. Phys. Res. A 496 (2003) 138.

Tb³⁺ impurities are observed (marked with asterisks). For LuCl₃ doped with Ce³⁺, the spectrum is dominated by a broad emission band located between 350 and 500 nm, peaking at 374 nm. It is caused by transitions from the lowest energy level of the Ce³⁺ 4*f*5*d* configuration to the spin-orbit split ²F_{5/2} and ²F_{7/2} levels. The x-ray excited optical luminescence spectrum of LuBr₃:0.021% Ce³⁺ is dominated by a broad luminescence band, ranging from 200 nm to at least 800 nm with a maximum around 455 nm. It is probably due to STE emission. For other bromides [6,7] similar bands have been observed and were ascribed to STE luminescence. The x-ray excited optical luminescence spectra of LuBr₃:Ce³⁺ are dominated by a broad emission band located between 350 nm and 600 nm, due to Ce³⁺ luminescence. Note that when the Ce concentration is increased, the intensity of the Ce³⁺ emission band decreases.

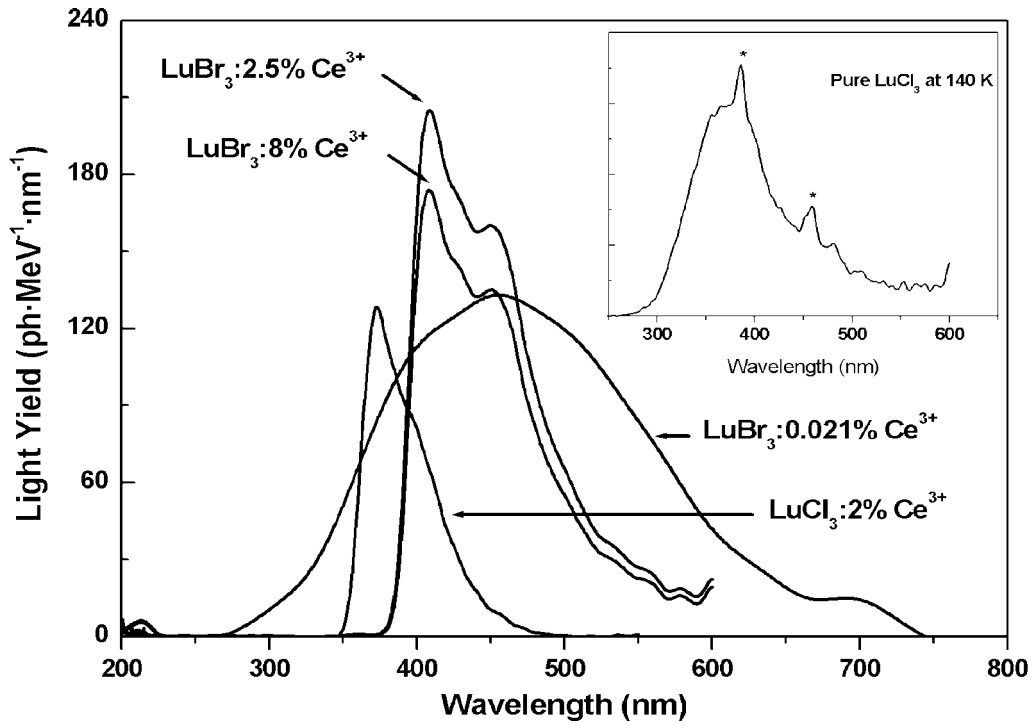


Fig. 1. X-ray excited optical luminescence spectra of LuBr₃:0.021%, 2.5%, 10% Ce³⁺, and LuCl₃:2% Ce³⁺ at room temperature. The y-axis has been calibrated using the light yields derived from pulse height spectra. The inset shows the x-ray excited optical luminescence spectrum of pure LuCl₃ at 140 K. For this spectrum the y-axis has not been calibrated. The asterisks indicate 4*f* – 4*f* transitions of Tb³⁺ impurities.

Figure 2 shows the light yield of pure LuCl₃ as function of 1/*T* (K⁻¹). The dotted curve shows the best fit (*R* = 0.99915) to a model calculation according to

$$I(T) = \frac{I_0}{(1 + \tau_R \nu_0 e^{-E/kT})} \quad (1)$$

where *I*₀ is the intensity in the low temperature limit *T* → 0 K, τ_{*R*} the lifetime of radiative decay, ν₀ the rate of non-radiative decay, *E* the activation energy of non-radiative decay, and *k* the Boltzmann constant. Accordingly, the activation energy of non-radiative decay *E* was determined to be 81 ± 3 meV.

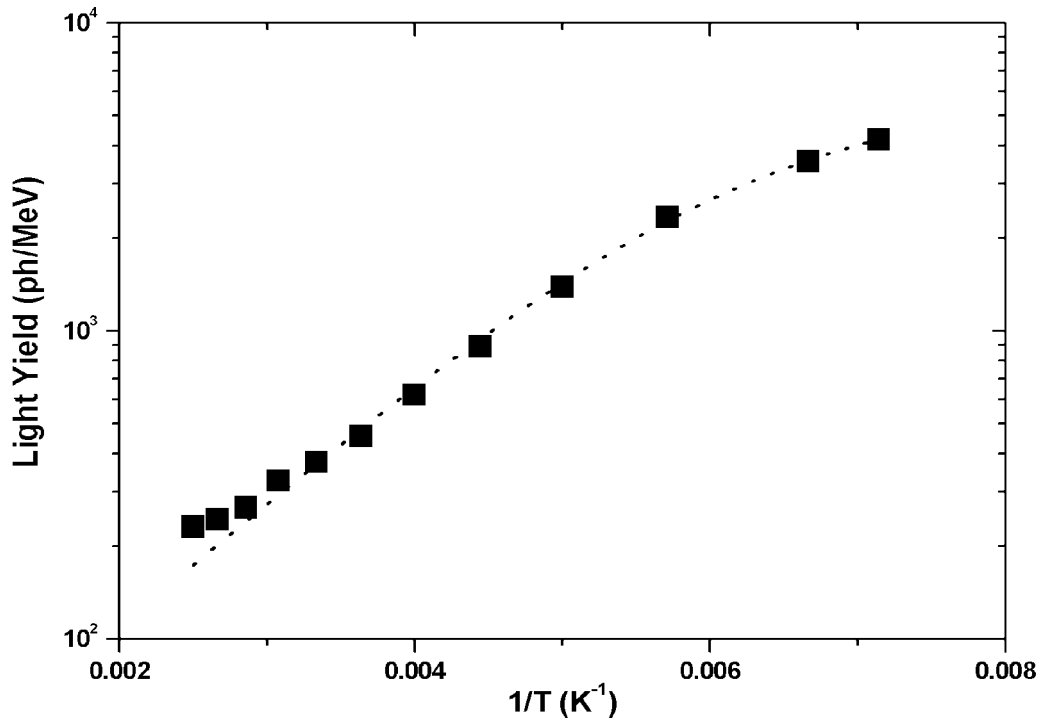


Fig. 2. The light yield of pure LuCl₃ as function of 1/T (K⁻¹).

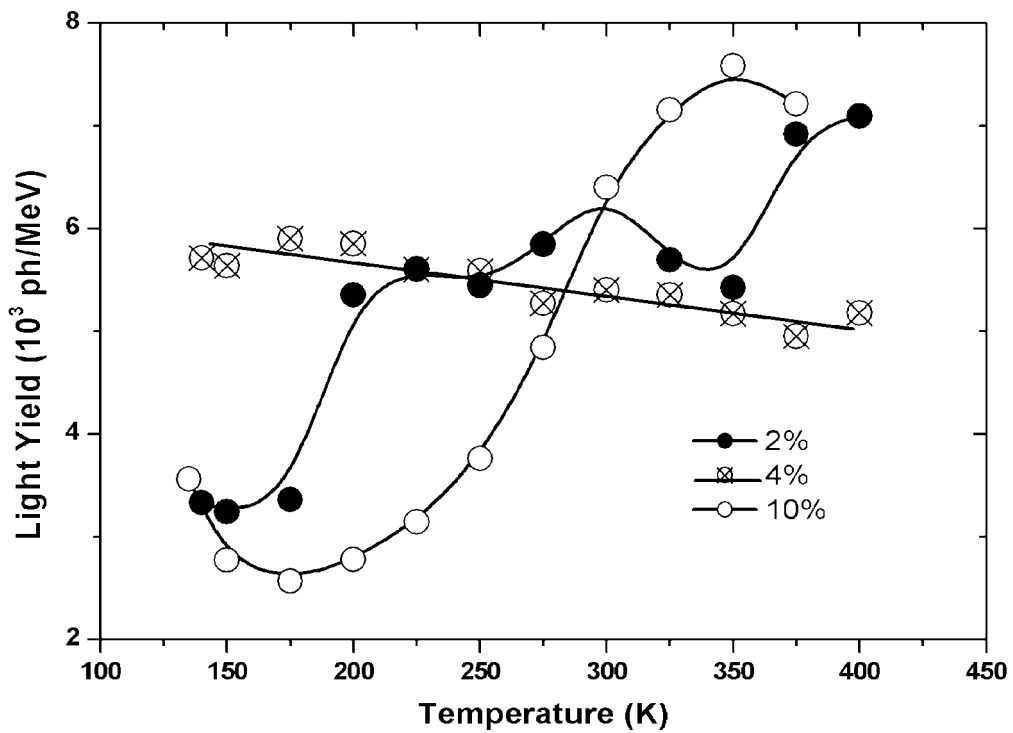


Fig. 3. Temperature dependence of the light yield of LuCl₃:2%, 4%, and 10% Ce³⁺. The lines are drawn to guide the eye.

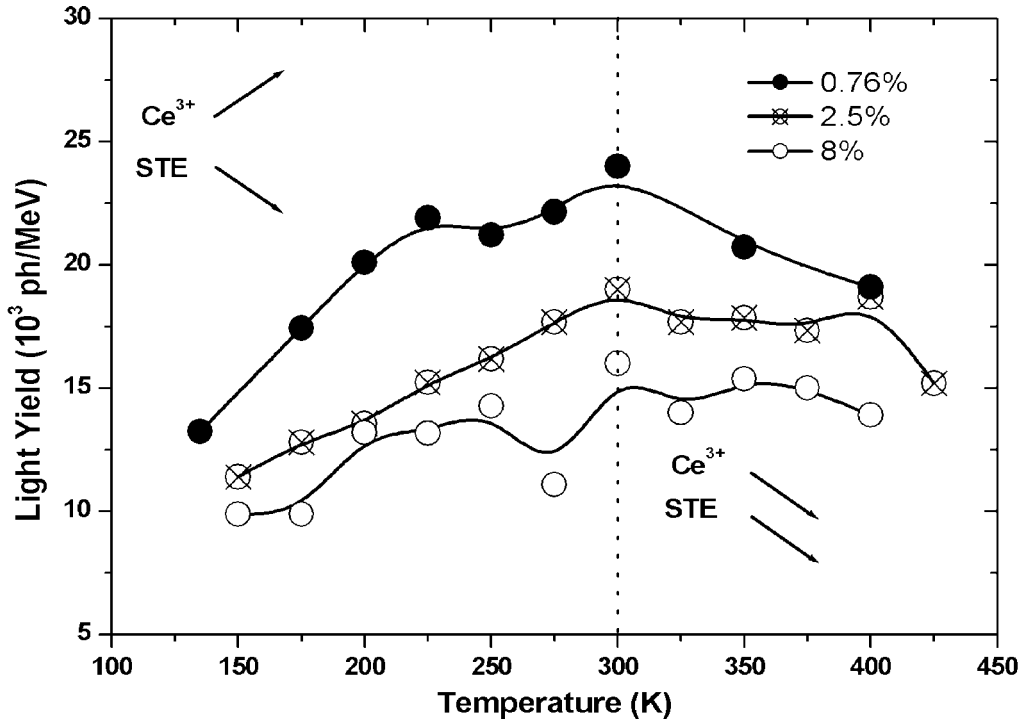


Fig. 4. Temperature dependence of the light yield of $\text{LuBr}_3:0.76\%$, 2.5% , and $8\% \text{Ce}^{3+}$. The lines are drawn to guide the eye. The small upward and downward pointing arrows denote the increase and decreases, respectively, of the intensity of STE and Ce^{3+} luminescence.

In Ref. [1], the temperature dependence of the total light yield of $\text{LuCl}_3:0.45\% \text{Ce}^{3+}$ under X-ray excitation was presented. Here, we show the light yield as function of temperature for pure $\text{LuCl}_3:2\%$, 4% , and $10\% \text{Ce}^{3+}$, see Fig. 3. From 140 to 400 K, the light yield of $\text{LuCl}_3:2\% \text{Ce}^{3+}$, increases by about 110%. The light yield of $\text{LuCl}_3:4\% \text{Ce}^{3+}$ decreases slightly in the same temperature interval. At 400 K, it is about 90% of that at 140 K. The evolution of the light yield as function of temperature of $\text{LuCl}_3:10\% \text{Ce}^{3+}$ is very much identical to that of the elpasolites (see Chapter 6). First, it decreases by about 30% from 135 to 175 K, then increases by 200% up to 375 K, and finally decreases by 5% from 375 to 400 K.

The temperature dependence of the light yield under X-ray excitation of $\text{LuBr}_3:\text{Ce}^{3+}$ is shown in Fig. 4. For $\text{LuBr}_3:0.76\% \text{Ce}^{3+}$, the Ce^{3+} luminescence intensity increases between 135 and 300 K, while the STE emission decreases. This is indicated with small arrows. Between 300 and 425 K, both STE and Ce^{3+} emission intensities decrease. A similar behaviour is observed for $\text{LuBr}_3:2.5\%$ and $8\% \text{Ce}^{3+}$.

8.3.2 Light yield

In Ref. [1], first results on gamma-ray excited scintillation light yields were presented. In Table I, results are presented on absolute light yields derived from pulse height spectra under ^{137}Cs γ -ray excitation for pure LuCl_3 , $\text{LuCl}_3:2\%$, 4% , 10% , Ce^{3+} , $\text{LuBr}_3:0.021\%$, 0.46% , 0.76% , 2.5% , and $8\% \text{Ce}^{3+}$.

In order to determine the position of the photopeak and the energy resolution of the studied compounds, the photopeak was fitted with several Gaussian curves. In addition to scintillation pulses emitted after absorption of ^{137}Cs 662 keV photons, scintillation pulses are generated intrinsically too. The intrinsic activity is due to the presence of the radioactive ^{176}Lu isotope in natural lutetium with an abundance of

2.6%. The background spectrum is due to β -particles with end-point energies of 195 and 596 keV, and to main photons with energies of 202 and 307 keV.

A pulse height spectrum could not be obtained with pure LuCl_3 due to the very low light yield. By comparing the integral of the X-ray excited optical luminescence spectrum of pure LuCl_3 with other samples, the light yield at room temperature was estimated to be 375 ± 50 ph/MeV. For LuCl_3 :2%, 4%, and 10% Ce^{3+} we measured light yields of the order of 4000 – 6000 ph/MeV. LuBr_3 :0.021% Ce^{3+} has the highest light yield at room temperature: 29000 ± 3000 ph/MeV. Fig. 1 shows that it is mainly due to STE luminescence. From 0.5 to 10 μs , an increase of $> 500\%$ is measured, see Table I. This means that the STE luminescence is characterised by a main decay component of the order of a few microseconds. For the LuBr_3 : Ce^{3+} , the light yield decreases as the Ce concentration is increased. For LuBr_3 :0.76%, 2.5%, and 8% Ce^{3+} , the light yield is 26000, 19000, and 16000 ph/MeV, respectively. For LuBr_3 :0.46% Ce^{3+} we obtained a rather low value for the absolute light yield, i.e. 18000 ph/MeV, compared to LuBr_3 :0.021% and 0.76% Ce^{3+} . This sample originates from a different batch than the other bromides and the quality of this crystal could easily be less than the quality of the other samples.

Table I. Light yields derived from pulse height spectra, energy resolution R , photomultiplier resolution R_M and scintillator resolution R_s of pure LuCl_3 , LuCl_3 :0.45%, 2%, 4%, 10% Ce^{3+} , LuBr_3 :0.021%, 0.46%, 0.76%, 2.5% and 8% Ce^{3+} under ^{137}Cs 662 keV γ -ray excitation.

Host	[Ce^{3+}] (%)	Photon yield (10^3 ph/MeV)			Energy resolution R (%)	Photo- multiplier resolution R_m (%)	Scintillator resolution R_s (%)
		0.5 μs	3 μs	10 μs			
LuCl_3	-	-	-	-	-	-	-
LuCl_3	0.45	5.5 ± 0.5	6.3 ± 0.6	6.6 ± 0.6	18.0 ± 0.5	7.8 ± 0.1	16.0 ± 0.5
LuCl_3	2	5.5 ± 0.5	6.3 ± 0.6	6.4 ± 0.6	13.8 ± 0.5	13.6 ± 0.5	2.2 ± 0.1
LuCl_3	4	4.8 ± 0.4	5.2 ± 0.4	5.4 ± 0.5	11.4 ± 0.4	8.5 ± 0.4	7.6 ± 0.3
LuCl_3	10	5.9 ± 0.5	6.7 ± 0.6	6.4 ± 0.6	11.7 ± 0.4	7.3 ± 0.3	9.2 ± 0.4
LuBr_3	0.021	5.4 ± 0.5	18 ± 2	29 ± 3	8.6 ± 0.5	4.5 ± 0.2	7.4 ± 0.4
LuBr_3	0.46	9 ± 1	14 ± 1	18 ± 2	7.8 ± 0.3	4.8 ± 0.1	6.1 ± 0.4
LuBr_3	0.76	11 ± 1	18 ± 2	26 ± 3	6.5 ± 0.5	4.2 ± 0.1	5.0 ± 0.5
LuBr_3	2.5	11 ± 1	16 ± 2	19 ± 2	6.2 ± 0.2	5.2 ± 0.2	3.4 ± 0.1
LuBr_3	8	11 ± 1	14 ± 1	16 ± 1	6.0 ± 0.1	5.4 ± 0.1	2.6 ± 0.1

8.3.3 Scintillation decay

The gamma ray excited scintillation decay time spectra at 300 K of pure LuCl₃, LuCl₃:2% and 4% Ce³⁺ are presented in Fig. 5. At first sight, the decay curves are not simply exponential and have a long decay component extending into the microsecond region. If only the first few microseconds are considered, the decay time decreases when the Ce concentration increases. Scintillation decay time spectra of LuBr₃:0.021%, 0.76%, 2.5%, and 8% Ce³⁺ are shown in Fig. 6. As for the chlorides, a simple exponential decay profile is not observed. Only LuBr₃:0.021% Ce³⁺ can the scintillation decay curve be characterised by a first order exponential decay function. In order to characterise the decay curves more accurately, three decay components were assumed. This assumption has not necessarily a physical meaning but is used to analyse the data. In Table II, the three decay components are presented as well as their relative contribution to the light yield of the crystals. If not denoted otherwise, all decay components are exponential.

Table II. Characteristic components of the scintillation decay curves of pure LuCl₃, LuCl₃:0.45%, 2%, 4%, 10%, Ce³⁺, LuBr₃:0.021%, 0.46%, 0.76%, 2.5%, and 8% Ce³⁺. The components marked with an asterisk are non-exponential and have been approximated by a hyperbolic function.

Host	[Ce ³⁺] (%)	Decay components (relative contribution to the total light yield)		
		Short (ns)	Intermediate (ns)	Long (μ s)
LuCl ₃	–	-	830 ± 90 *	-
LuCl ₃	0.45	-	110 ± 10 (87%) *	> 2 (13%)
LuCl ₃	2	-	85 ± 9 (73%) *	> 6 (27%)
LuCl ₃	4	-	76 ± 8 (91%) *	> 6 (9%)
LuCl ₃	10	-	88 ± 9 (81%) *	> 9 (19%)
LuBr ₃	0.021	-	-	6 ± 1
LuBr ₃	0.46	32 ± 3 (10%)	500 ± 50 (20%)	> 5 (70%)
LuBr ₃	0.76	32 ± 3 (15%)	500 ± 50 (21%)	> 5 (64%)
LuBr ₃	2.5	20 ± 2 (31%)	480 ± 50 (18%)	> 5 (51%)
LuBr ₃	8	19 ± 2 (33%)	370 ± 50 (22%)	> 5 (45%)

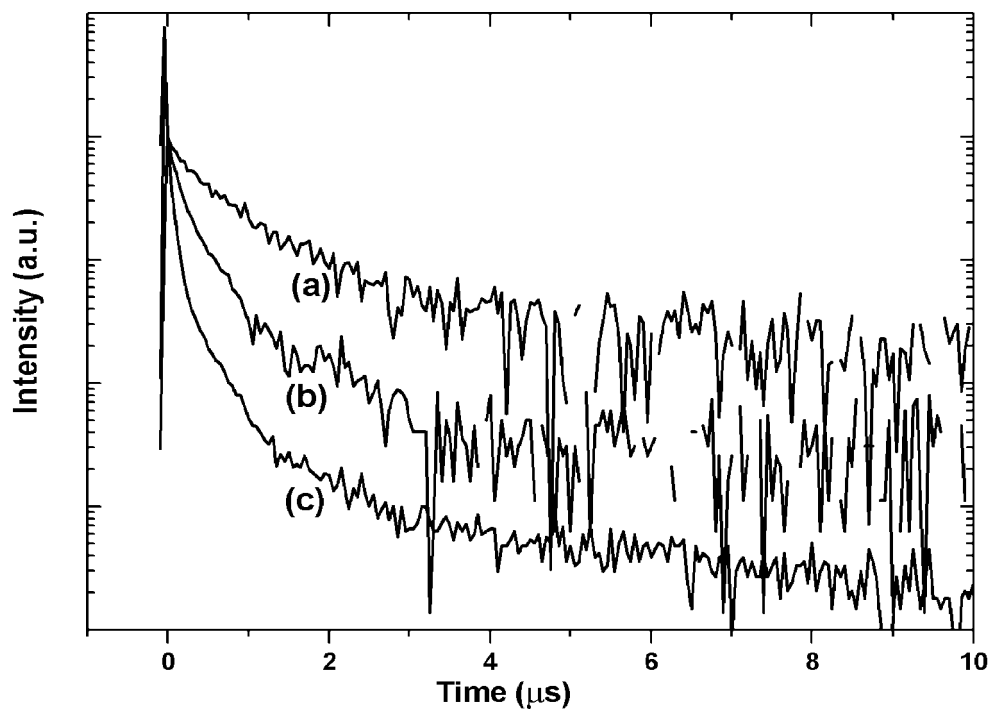


Fig. 5. Scintillation decay time spectra at room temperature of (a) pure LuCl_3 , (b) LuCl_3 :2% Ce^{3+} , and (c) LuCl_3 :4% Ce^{3+} .

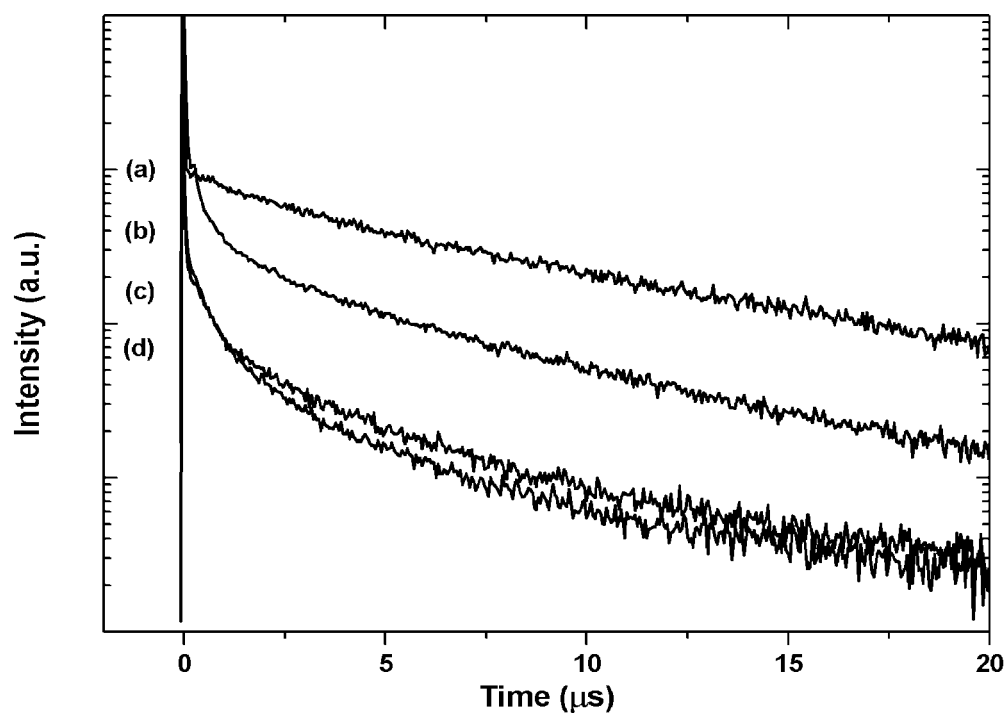


Fig. 6. Scintillation decay time spectra at room temperature of (a) LuBr_3 :0.021% Ce^{3+} , (b) LuBr_3 :0.76% Ce^{3+} , (c) LuBr_3 :2.5% Ce^{3+} , and (d) LuBr_3 :8% Ce^{3+} .

8.4 Discussion

8.4.1. $\text{LuCl}_3:\text{Ce}^{3+}$

Let us consider pure LuCl_3 first. Its very low light yield at room temperature suggests that the non-radiative decay of the STE in LuCl_3 proceeds with a high probability. It might be due to the presence of traps in the lattice, or simply because the STE is strongly coupled to the phonons in the lattice. It has been argued that quenching of STE luminescence must involve activation over a barrier against F – H pair formation [8-10]. Interestingly, the activation energy of non-radiative decay of pure LuCl_3 is of the same order of magnitude as the activation energy needed to overcome this barrier, i.e. ~ 80 meV.

Since the crystal structure of LuCl_3 leaves ample room for the off-centre relaxation of the V_K core of the STE in the $\langle 001 \rangle$ direction, i.e. the relaxation of the chloride ion into the space between the layers, the quenching of STE luminescence in LuCl_3 is probably the result of the nearest neighbour F – H pair formation and their subsequent, non-radiative decay.

In the case of $\text{LuCl}_3:0.45\%$, 2%, 4%, and 10% Ce^{3+} , the behaviour of the electrons, holes and the STE might be completely different. Here, the presence of Ce^{3+} acts as an iso-electronic impurity which does not introduce an electrostatic long-range potential, but may present a short-range potential by the difference of its electronegativity from that of the host atom. Also, the introduction of Ce^{3+} on a smaller cationic site ($r_{\text{Ce}^{3+}}/r_{\text{Lu}^{3+}} \approx 1.15$) results in a relaxation of the immediate environment of Ce^{3+} that can create a potential well for the trapping of electrons or holes. The absence of STE luminescence at room temperature in the samples with a low Ce concentration is an indication that the non-radiative decay of the STE in $\text{LuCl}_3:\text{Ce}^{3+}$ also proceeds with a high probability. However, it is also possible that the apparent presence of a potential well prevents the formation of an STE because of the trapping and stabilisation of electrons or holes near Ce^{3+} .

Since the STE apparently favours the off-centre position in pure LuCl_3 and effectively is a nearest neighbour F – H pair, the H centre may diffuse apart from the trapped electron and be stabilised near a Ce^{3+} . Considering the above and the notion that the major part of the decay curves for $\text{LuCl}_3:2\%$, 4%, and 10% Ce^{3+} are non-exponential, *energy transfer by binary electron-hole diffusion* is proposed to be the dominant scintillation mechanism in these materials.

The temperature dependence of the light yield of $\text{LuCl}_3:2\%$, 4%, and 10% Ce^{3+} can be explained as follows: for temperatures $T < 175$ K, the diffusion rate of the electrons and holes is too slow to reach a Ce^{3+} centre before an intrinsic, localised F – H pair is formed. Most part of the emission is therefore due to the recombination of the nearest neighbour F – H pair (STE). From 175 to 350 K, the mobility of the H centre and the mobility of the F – H pair increases. Recombination on Ce^{3+} partly yields Ce^{3+} emission and the light yield increases with temperature. It is quite possible that the H centre is a nearest neighbour of a Ce^{3+} centre, whereas the lattice traps the electron at an anion vacancy (F centre). If the configuration is stable, neither Ce^{3+} nor STE emission is observed. This would explain the rather low light yield of the samples.

8.4.2 $\text{LuBr}_3:\text{Ce}^{3+}$

For $\text{LuBr}_3:0.76\%$, 2.5% , and 8% Ce^{3+} , the light yield decreases considerably if Ce^{3+} is incorporated into pure LuBr_3 . Similar effects have been observed for BaF_2 doped with different La^{3+} concentration [11]. In this material, the electrons transfer from the interstitial fluorine ions to La^{3+} where they are loosely trapped. The hole remains on the fluorine interstitial ion and is supposed to become self-trapped, forming a H centre with one of the other native fluorine ions [12]. At higher temperatures, another native fluorine ion may move to an off-centre position and form an additional H centre leaving an anion vacancy. Subsequently, the electron trapped in a shallow state of La^{3+} may be trapped at this vacancy and form a F centre.

In the case of $\text{BaF}_2:\text{La}^{3+}$, it is assumed that the electron is trapped in shallow La states. Quantum mechanical calculation show that there are indeed La states below the bottom of the conduction band [13]. In the case of $\text{LuBr}_3:\text{Ce}^{3+}$, it is not feasible that Ce^{3+} traps an electron. So far, it has only been observed in CaF_2 , SrF_2 , and BaF_2 [14].

Additionally, the absence of the interstitial halide ion inhibits the prompt formation of a H centre. However, it is assumed that at $T < 100$ K a hole will readily be trapped in the indigenous lattice to form a V_K or H centre. As for LuCl_3 , the crystal structure of LuBr_3 leaves ample room for the off-centre relaxation of the V_K core of the STE in the $[001]$ direction, i.e. the relaxation of the bromide ion into the space between the layers. Interestingly, the energy of the STE luminescence in LuBr_3 is about 0.6 eV lower than the energy of the STE luminescence in the chloride. Probably, the axial shift of the V_K core towards an off-centre position in LuBr_3 is even larger than that in the chloride. Quenching of STE luminescence by Ce^{3+} is only possible if Ce^{3+} traps the V_K or H centre before it can recombine with the electron, provided that the electron is stabilised elsewhere. In the case of the H centre stabilised near Ce^{3+} , the electron occupies the anion vacancy and forms an F centre. Probably, this process is very efficient and neither radiative energy transfer via the STE to Ce^{3+} nor STE diffusion will play an important role.

We propose *energy transfer by binary electron hole diffusion* as the dominant scintillation mechanism. At $T < 100$ K, the holes are trapped in the lattice and form H centres, whereas the electrons occupy the nearest neighbour anion vacancies and form F centres. If the temperature is raised, the mobility of the H centres increases, whereas the F centre remains on-site. If it is assumed that Ce^{3+} acts as a deep trap for the H centres, the diffusion of the H centres through the lattice will eventually lead to the trapping and stabilisation of the H centres near Ce^{3+} . A small part of the holes may recombine with the F centres leading to STE luminescence. The trapping by Ce^{3+} is very efficient, since the light yield of STE luminescence in $\text{LuBr}_3:\text{Ce}^{3+}$ is negligible compared to $\text{LuBr}_3:0.021\%$ Ce^{3+} . It is not assumed that the F and H centres diffuse in a correlated motion. If this were true, the lifetime of the STE, i.e. the $F - H$ pair, would decrease significantly when the Ce concentration is increased, but this has not been observed.

At higher Ce concentrations, the probability that a H centre is trapped near Ce^{3+} increases and number of traps for both the hole and the electron increases. Thus, the light yield decreases if the Ce concentration is increased. At $T > 350$ K, the light yield of $\text{LuBr}_3:\text{Ce}^{3+}$ decreases because temperature effects quench the Ce^{3+} emission.

8.5 Conclusions

For both $\text{LuCl}_3:\text{Ce}^{3+}$ and $\text{LuBr}_3:\text{Ce}^{3+}$, *binary electron-hole diffusion* is the model that describes the scintillation mechanism best. This model was proposed earlier for $\text{LuPO}_4:\text{Ce}^{3+}$, $\text{LuAlO}_3:\text{Ce}^{3+}$ [15] and NaI:Tl [16] where Ce^{3+} and Tl^+ act as hole and electron trap, respectively, and the elpasolites (see chapter 7).

$\text{LuCl}_3:\text{Ce}^{3+}$ and $\text{LuBr}_3:\text{Ce}^{3+}$ have a low light yield and long decay components are present in the scintillation decay. Increasing the Ce concentration has no significant influence on the scintillation properties of the chloride. For the bromide an anti-correlation was observed between Ce concentration and light yield.

References

- ¹ O. Guillot-Noël, J.T.M. de Haas, P. Dorenbos, C.W.E. van Eijk, K.W. Krämer, H.U. Güdel, *J. Lumin.* 85 (1999) 21.
- ² J.B. Reed, B.S. Hopkins, L.F. Audrieth, *Inorg. Synth.* 1 (1936) 28.
- ³ G. Meyer, *Inorg. Synth.* 25 (1989) 146.
- ⁴ D.H. Templeton, G.F. Carter, *J. Phys. Chem.* 58 (1954) 940.
- ⁵ D. Brown, S. Fletcher, D.G. Hollah, *J. Chem. Soc. A* (1968) 1889.
- ⁶ O. Guillot-Noël, J.C. van't Spijker, J.T.M. de Haas, P. Dorenbos, C.W.E. van Eijk, K.W. Krämer, H.U. Güdel, *IEEE Trans. Nucl. Sci.* 46 (5) (1999) 1274.
- ⁷ E.V.D. van Loef, P. Dorenbos, C.W.E. van Eijk, K.W. Krämer, H.U. Güdel, *Opt. Commun.* 189 (2001) 297.
- ⁸ R.T. Williams, B.B. Craig, W.L. Faust, *Phys. Rev. Lett.* 52 (19) (1984) 1709.
- ⁹ N. Itoh, T. Eshita, R.T. Williams, *Phys. Rev.* B34 (6) (1986) 4230.
- ¹⁰ R.T. Williams, K.S. Song, *J. Phys. Chem. Sol.* 51 (7) (1990) 679.
- ¹¹ P. Dorenbos, R. Visser, R.W. Hollander, C.W.E. van Eijk, H.W. Den Hartog, *Rad. Eff. Def. Sol.* 119 (1991) 87.
- ¹² E. Radzhabov, A. Nepomnyashikh, A. Egranov, *J. Phys.: Condens. Matter* 14 (2002) 7337.
- ¹³ M. Gu, L.Y. Chen, Q. Li, X. Wu, *Commun. Theor. Phys.* 26 (1996) 279.
- ¹⁴ C. Pedrini, P.O. Pagost, C. Madej, D.S. McClure, *J. Physique* 42 (1981) 323.
- ¹⁵ A.J. Wojtowicz, A. Lempicki, D. Wisniewski, M. Balcerzyk, C. Brecher, *IEEE Trans. Nucl. Sci.* 43 (1996) 2168.
- ¹⁶ R.G. Kaufman, W.B. Hadley, H.N. Hersch, *IEEE Trans. Nucl. Sci.* 17 (1970) 82.

9. The ternary halides – $\text{K}_2\text{LaX}_5:\text{Ce}^{3+}$ ($X = \text{Cl}, \text{Br}, \text{I}$)*

9.1 Introduction

In the previous chapters we have introduced several new inorganic scintillators, presented their optical and scintillation properties, and discussed the scintillation mechanisms. In an attempt to investigate the influence of the chemical environment on the optical and scintillation properties of metal-halide scintillators, we decided to work on pure and Ce^{3+} doped K_2LaX_5 ($X = \text{Cl}, \text{Br}, \text{I}$). These systems are isostructural, whereas the environment of the trivalent cation is altered by chemical variation of the halide ion from Cl to Br to I.

It is well known that the physical and chemical properties of the halogens and their anions change considerably along the series from F to Cl to Br to I. The anion has a profound influence on both the energy of the $5d$ levels of Ce^{3+} [1-3], and the luminescence properties of the pure compound. For instance, the emission energies and lifetimes of self-trapped excitons (STEs) in alkali halides strongly depend on the anion [4]. Also the dynamical properties of the STE change because, e.g., the energy barrier for STE migration through the lattice decreases from Cl to Br to I.

In this chapter, we report on the influence of the anion on the spectroscopic and scintillation properties of pure and Ce^{3+} doped K_2LaX_5 . Both static and dynamic aspects are discussed. The spectroscopic properties of $\text{K}_2\text{LaX}_5:\text{Ce}^{3+}$ are compared with those of Ce^{3+} in LaCl_3 and LaBr_3 , and to a lesser extent with LaI_3 , as well as of Eu^{2+} in the potassium halides KX . The emission wavelength and lifetime of the STE, the energy of the $4f/5d$ states of Ce^{3+} , as well as energy transfer from the STE to Ce^{3+} are described and discussed.

9.2 Material

Single crystals of pure and Ce^{3+} doped K_2LaX_5 ($X = \text{Cl}, \text{Br}, \text{I}$) were grown by the vertical Bridgman technique using a static ampoule and a moving furnace. KX (Merck, suprapur), LaX_3 , and CeX_3 were used as starting materials. $\text{LaCl}_3/\text{Br}_3$ and $\text{CeCl}_3/\text{Br}_3$ were prepared from La_2O_3 using the ammonium halide method [5,6]. LaI_3 and CeI_3 were synthesised from the elements [7]. To remove traces of water and oxygen they were purified by sublimation in tantalum or silica ampoules. For the crystal growth stoichiometric amounts of the starting materials were sealed in silica ampoules under vacuum. All material handling was done under strictly dry conditions, e.g. in glove boxes with $\text{H}_2\text{O} < 01$ ppm.

The ternary halides K_2LaX_5 crystallise in the K_2PrX_5 type structure, space group Pnma (no. 62) [8]. The structure can be described as a hexagonal densest arrangement of chains of edge-connected polyhedra $[\text{LaX}_7]$. The polyhedra may be viewed as mono-capped trigonal prisms with the La^{3+} ion in the centre, see Fig. 1. The point symmetry at the La site is C_s . The seven Cl^- , Br^- , or I^- ions are at an average distance of 284 pm, 299 pm, and 323 pm from the central La^{3+} ion, respectively. The

* based on: E.V.D. van Loef, P. Dorenbos, C.W.E. van Eijk, K.W. Krämer, H.U. Güdel, Phys Rev. B, submitted.

calculated density of K_2LaCl_5 , K_2LaBr_5 , and K_2LaI_5 is 2.9 g/cm^3 , 3.9 g/cm^3 , and 4.4 g/cm^3 , respectively.

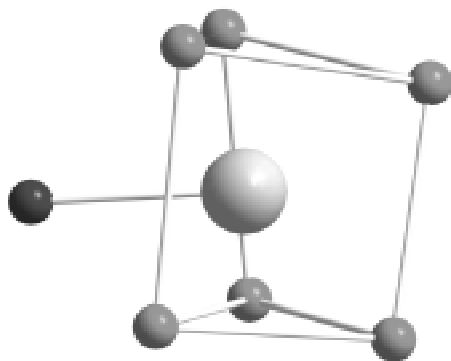


Fig. 1. The distorted mono-capped trigonal prism polyhedron around La^{3+} in K_2LaCl_5 .

9.3 Results

9.3.1 X-ray excited optical luminescence

Figure 2 shows the X-ray excited optical luminescence spectra of K_2LaX_5 ($X = \text{Cl, Br, I}$) at 80 K. The spectra are dominated by a broad emission band located between 300 and 550 nm. The emission band can readily be assigned to self-trapped exciton (STE) luminescence. For the iodide (c), the emission spectrum of the STE is shown as the dotted trace. The sharp line emissions at 600 and 679 nm in the iodide spectrum and to a lesser extent in the bromide spectrum are probably due to not further identified rare earth impurities. The sharp decline of intensity in the K_2LaI_5 spectrum at wavelengths shorter than 400 nm is attributed to absorption of STE emission by the 380 nm $f\bar{d}$ band of Ce^{3+} , present as impurity in the nominally undoped compound. Ce^{3+} is also the origin for the emission bands observed near 400 and 440 nm. Unintended Ce^{3+} impurities are also the reason for some structure on the high energy side of the STE emission in K_2LaCl_5 and K_2LaBr_5 .

X-ray excited optical luminescence spectra of $\text{K}_2\text{LaCl}_5:0.1\% \text{ Ce}^{3+}$ [9], $\text{K}_2\text{LaBr}_5:0.7\% \text{ Ce}^{3+}$, and $\text{K}_2\text{LaI}_5:0.7\% \text{ Ce}^{3+}$ at 80 K are shown Fig. 3 (solid traces). Also depicted are the 300 K spectra of the bromide and the iodide compounds (dotted traces). For all three lattices characteristic $\text{Ce}^{3+} 5d \rightarrow 4f$ emission is observed. The maxima are located at 344 and 372 nm for the chloride, at 359 and 391 nm for the bromide, and at 401 and 439 nm for the iodide, for the $5d \rightarrow {}^2F_{5/2}$ and $5d \rightarrow {}^2F_{7/2}$ transitions, respectively. In addition, a weak emission is present as a broad band or tail on the long wavelength side of the Ce^{3+} doublet. It is attributed to residual STE emission. If the temperature is raised to 300 K the intensity of this band decreases rapidly and only Ce^{3+} emission is observed.

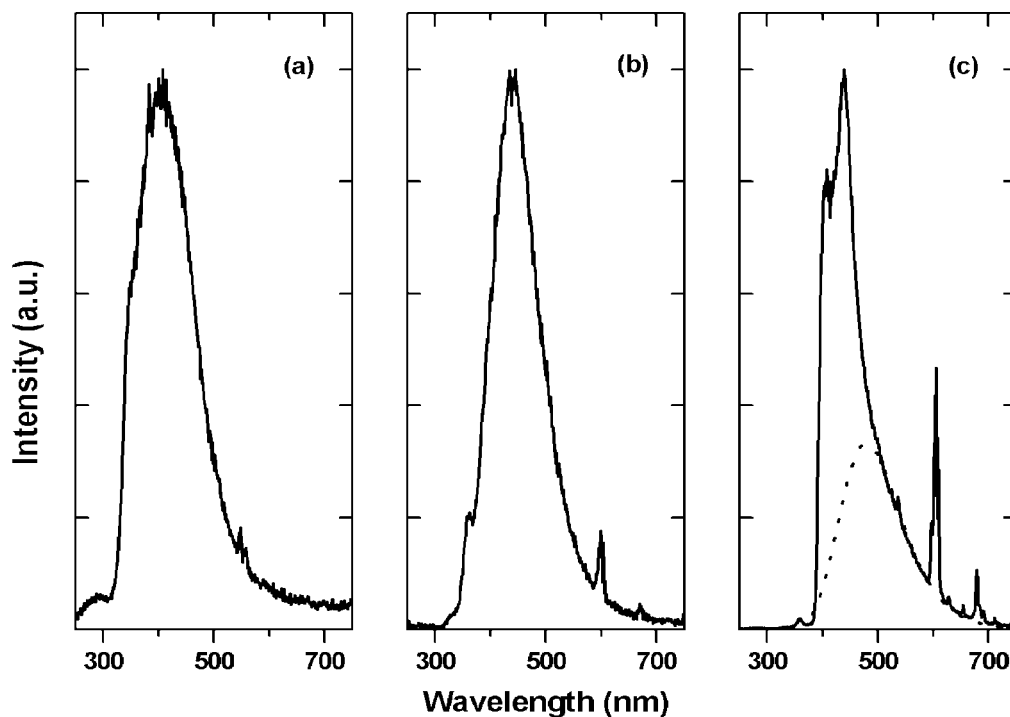


Fig. 2. X-Ray excited optical luminescence spectra of (a) K_2LaCl_5 , (b) K_2LaBr_5 , and (c) K_2LaI_5 at 80 K. The dotted trace in the iodide spectrum (c) represents the contribution of the STE to the emission.

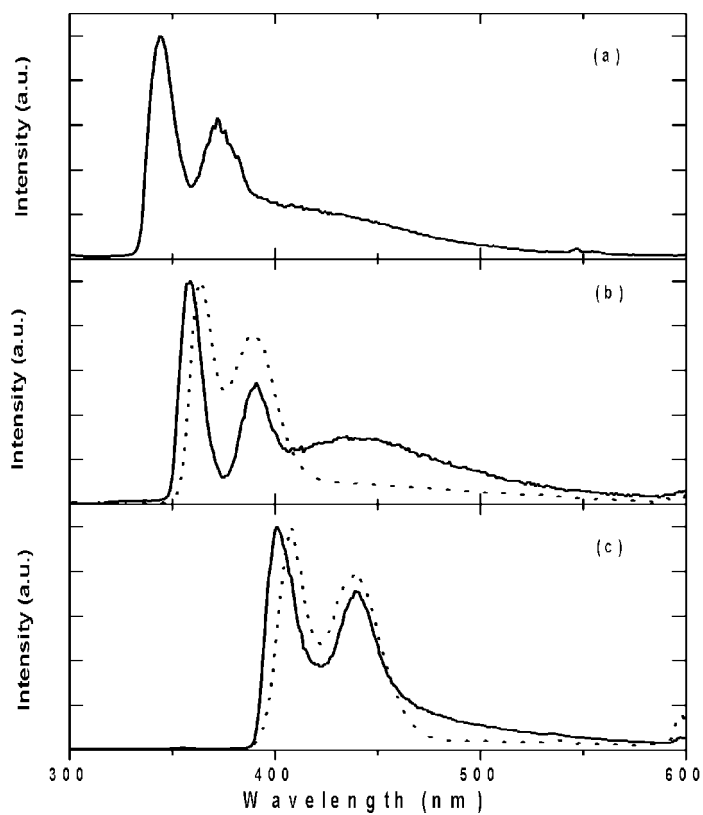


Fig. 3. X-Ray excited optical luminescence spectra of (a) $\text{K}_2\text{LaCl}_5:0.1\% \text{Ce}^{3+}$, (b) $\text{K}_2\text{LaBr}_5:0.7\% \text{Ce}^{3+}$, and (c) $\text{K}_2\text{LaI}_5:0.7\% \text{Ce}^{3+}$. The spectra were measured at 80 K (solid trace) and at 300 K (dotted trace).

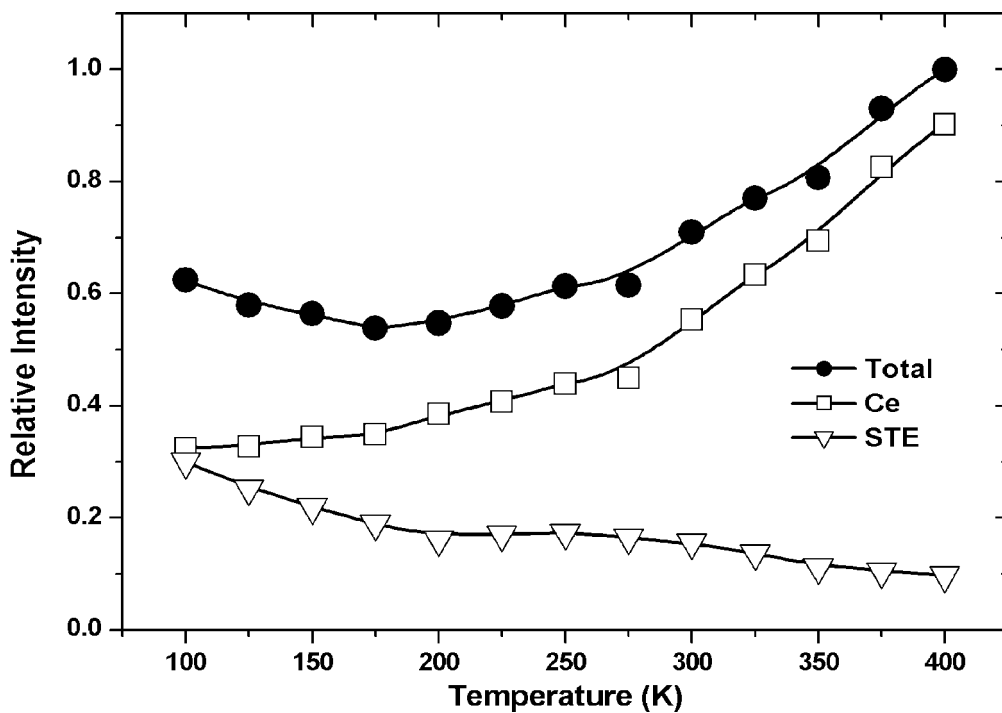


Fig. 4. Temperature dependence of Ce^{3+} , STE and total luminescence intensity of X-ray excited $\text{K}_2\text{LaBr}_5:0.7\% \text{Ce}^{3+}$.

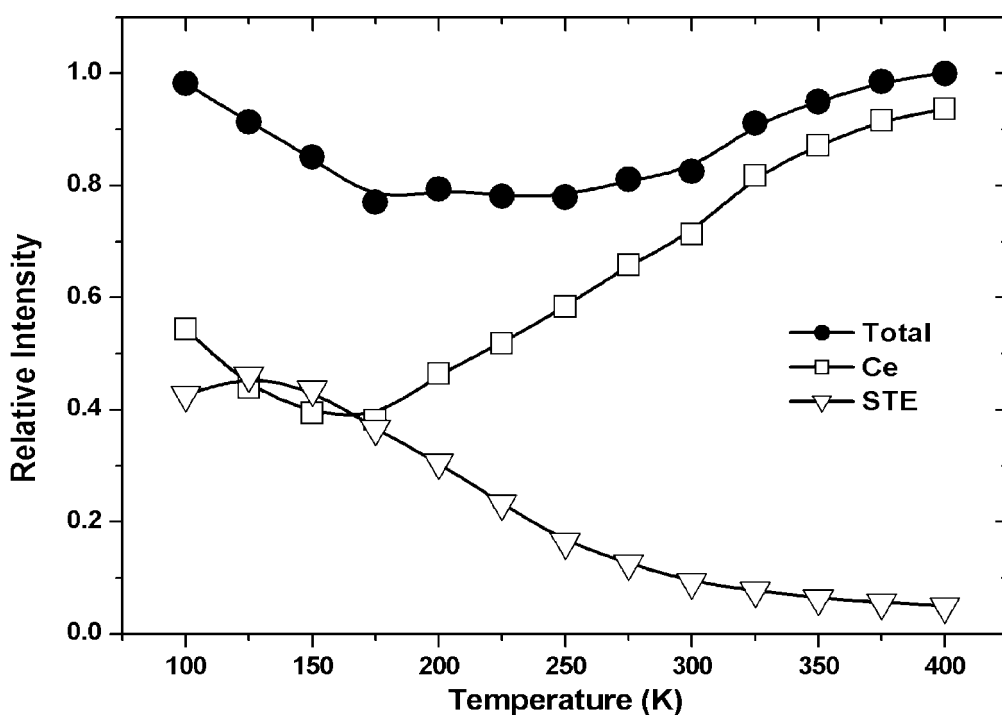


Fig. 5. Temperature dependence of Ce^{3+} , STE and total luminescence intensity of X-ray excited $\text{K}_2\text{LaI}_5:0.7\% \text{Ce}^{3+}$.

The total luminescence intensity under X-ray excitation of $\text{K}_2\text{LaBr}_5:0.7\% \text{Ce}^{3+}$ and $\text{K}_2\text{LaI}_5:0.7\% \text{Ce}^{3+}$ is depicted in Figs. 4 and 5, respectively. From 100 to 175 K, the total luminescence intensity of the bromide and iodide decreases by about 14% and

22%, respectively. As the temperature rises the Ce^{3+} luminescence intensity is enhanced at the expense of STE luminescence intensity (compare with Fig. 3). Also the total luminescence intensity increases. This anti-correlation between Ce^{3+} and STE luminescence has been observed more clearly in $\text{LaCl}_3:0.57\% \text{Ce}^{3+}$ by Guillot-Noël et al. [10] and in $\text{K}_2\text{LaCl}_5:0.23\% \text{Ce}^{3+}$ by van't Spijker et al. [9]. It appears to be a general behaviour in the K_2LaX_5 and LaX_3 systems. Furthermore, at 100 K the ratio of Ce^{3+} to STE emission increases along the series from Cl to I. At 100 K, the contributions of Ce^{3+} and STE luminescence to the total intensity of $\text{K}_2\text{LaCl}_5:0.23\% \text{Ce}^{3+}$ are 15% and 8%, respectively [9]. However, for $\text{K}_2\text{LaBr}_5:0.7\% \text{Ce}^{3+}$ and $\text{K}_2\text{LaI}_5:0.7\% \text{Ce}^{3+}$ the contributions of Ce^{3+} and STE luminescence are almost equal. At 135 K this is also true for $\text{LaCl}_3:0.57\% \text{Ce}^{3+}$. Whereas for $\text{LaBr}_3:\text{Ce}^{3+}$ the contribution of STE luminescence to the total luminescence intensity is negligible (see Chapter 6).

9.3.2. Optical excitation and emission

Figure 6 compares the excitation spectra of STE emission in pure K_2LaCl_5 and K_2LaBr_5 at 10 K. We define three different energy values. The fundamental absorption E_{fa} is the energy of the first sharp onset in the excitation or absorption spectrum of the pure compound. For K_2LaCl_5 this is 202 nm (6.1 eV). The first maximum in the excitation spectrum of STE emission is attributed to the creation of free excitons that can be regarded as bound electron hole pairs. This exciton energy E_{ex} is located at 197 nm (6.3 eV). For K_2LaCl_5 the edge of the conduction band E_{CB} is found at higher energy and corresponds to the creation of free electrons in the conduction band and free holes in the valence band. The second onset at 188 nm (6.6 eV) in the spectrum of K_2LaCl_5 is attributed to these across the bandgap excitations. The data on bandgap and exciton energies are compiled in Table I. Figure 6 also shows some excitations at energies below E_{fa} which are attributed to Ce^{3+} impurities in the nominally pure compounds.

Table I. Properties of undoped LaX_3 , K_2LaX_5 , and KX ($X = \text{Cl}, \text{Br}, \text{I}$).

Compound	E_{fa} (eV)	E_{ex} (eV)	E_{CB} (eV)	λ_{STE} (nm)	Ref.
LaCl_3	6.2	6.5	~7	405	[11]
LaBr_3	5.2	5.4	~6	430	
LaI_3	3.2	-	-	-	
KCl	7.5	7.8	8.7	537 (π)	[12]
KBr	6.4	6.7	7.4	544 (π)	[12]
KI	5.8	5.9	6.3	407 (π)	[12]
K_2LaCl_5	6.1	6.3	6.7	400	
K_2LaBr_5	5.0	-	-	440	
K_2LaI_5	3.9	-	-	480	

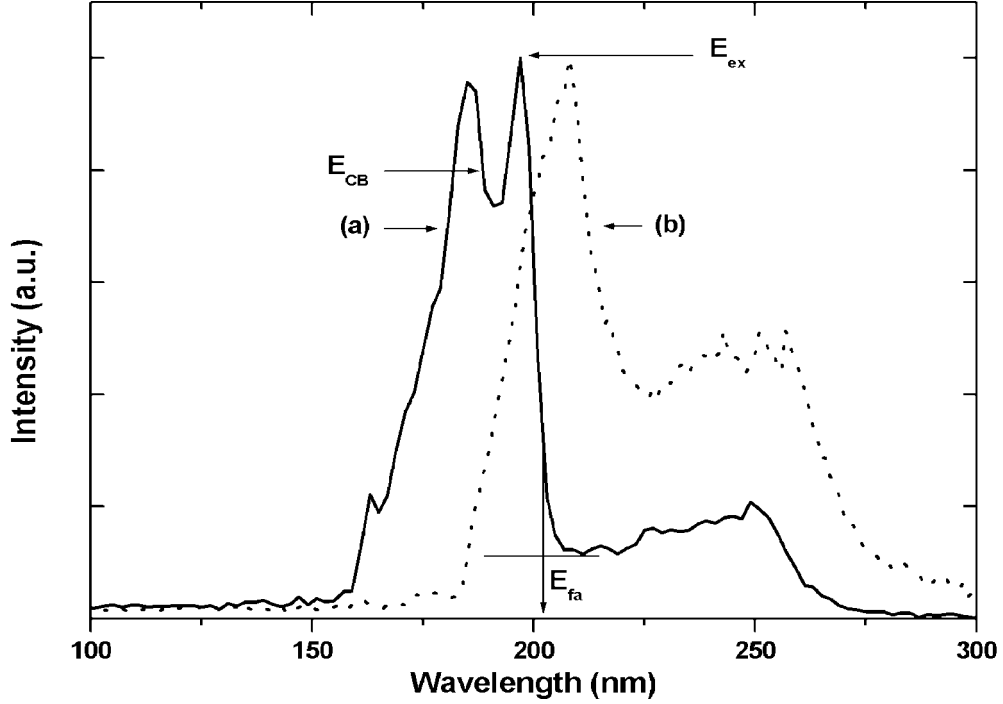


Fig. 6. Excitation spectra of (a) pure K_2LaCl_5 and (b) pure K_2LaBr_5 at 10 K monitoring STE luminescence at 415 and 400 nm, respectively.

Excitation and emission spectra of $\text{K}_2\text{LaCl}_5:0.1\% \text{Ce}^{3+}$ at 10 K are shown in Fig. 7 (solid traces). For comparison, the excitation spectrum of the undoped compound is reported as dotted trace. The emission spectrum shows two maxima located at 344 and 372 nm, due to transitions from the lowest energy level of the Ce^{3+} 5d configuration to the $^2\text{F}_{5/2}$ and $^2\text{F}_{7/2}$ levels, respectively. Accordingly, the ^2F spin-orbit splitting is 2190 cm^{-1} . In contrast to the X-ray excited optical luminescence spectrum shown in Fig. 3 no STE emission is excited at 222 nm.

Table II. Spectroscopic and crystallographic properties of Ce^{3+} doped LaX_3 and K_2LaX_5 , and Eu^{2+} doped KX ($X = \text{Cl, Br, I}$). Values between brackets are estimated values.

Compound	5d excitation bands					ϵ_c (cm^{-1})	ϵ_{cfs} (cm^{-1})	Ref.
	(nm)							
LaCl_3	243	250	263	274	281	13000	5565	[2,11]
LaBr_3	260	270	284	299	308	15906	5994	
LaI_3	-	-	-	-	420	-	-	
KCl:Eu^{2+}	2x(250)		3x(357)			-	12000	[13]
KBr:Eu^{2+}	2x(257)		3x(357)			-	10900	[13,14]
KI:Eu^{2+}	2x(266)		3x(357)			-	9500	[13]
K_2LaCl_5	221	239	256	316	337	13500	15400	
K_2LaBr_5	(235)	257	266	325	345	(15500)	(13600)	
K_2LaI_5	(263)	(280)	(300)	365	380	(19100)	(11700)	

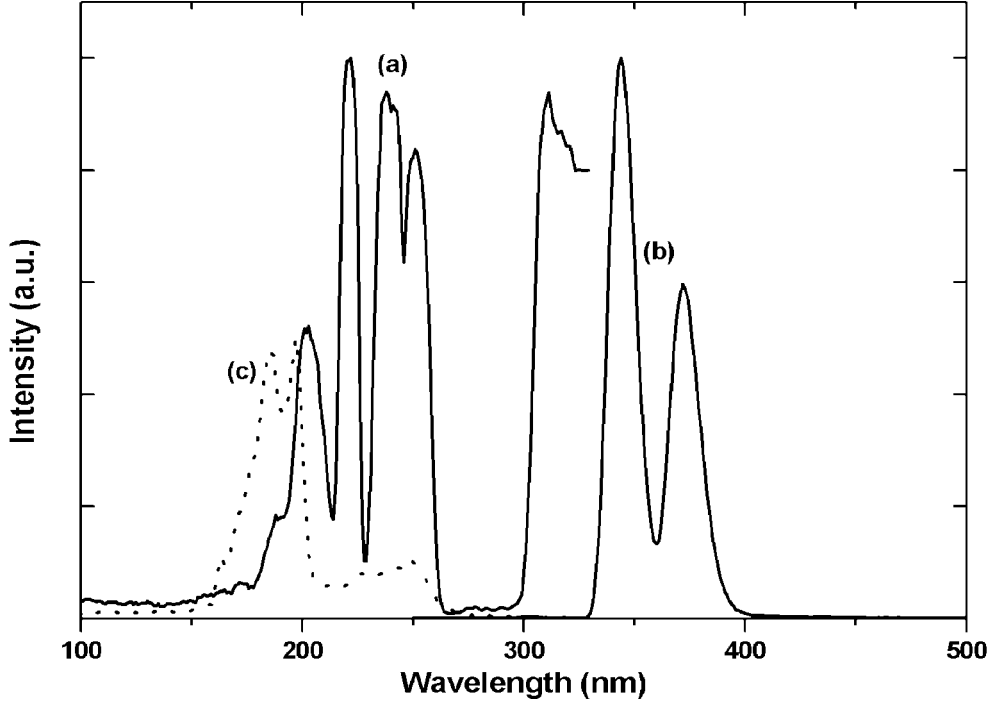


Fig. 7. (a) Excitation and (b) emission spectra of $\text{K}_2\text{LaCl}_5:0.1\% \text{Ce}^{3+}$ at 10 K. The excitation spectrum was measured at $\lambda = 372 \text{ nm}$, the emission spectrum was measured under $\lambda = 222 \text{ nm}$ excitation. The excitation spectrum at $\lambda = 415 \text{ nm}$ of pure K_2LaCl_5 (c) is shown for comparison.

In the excitation spectrum several bands can be distinguished. Four are located at 202, 221, 239, and 252 nm. Another band between 300 and 350 nm is actually composed of two subbands with maxima at 313 and 335 nm [9]. Based on the low symmetry of the La^{3+} site (C_5), we expect a five fold splitting of the Ce^{3+} $5d$ levels. We assign the five lowest bands to the five $5d$ levels of Ce^{3+} . The 2F spin-orbit splitting is 2380 cm^{-1} . The data are compiled in Table II. The band at 202 nm (6.1 eV) is located just at lower energy than the exciton peak in the pure compound at 197 nm. It is attributed to the creation of so-called impurity trapped excitons, i.e. an exciton created in the vicinity of a Ce^{3+} ion.

In Fig. 8 the time integrated and time resolved excitation and emission spectra of $\text{K}_2\text{LaBr}_5:0.7\% \text{Ce}^{3+}$ and of pure K_2LaBr_5 at 10 K are compared. The Ce^{3+} $5d \rightarrow 4f$ emission excited at 270 nm gives rise to two maxima at 357 and 388 nm (spectrum e). Accordingly, the spin-orbit splitting of the 2F ground state of Ce^{3+} is 2240 cm^{-1} . The time integrated excitation spectrum monitoring the $5d \rightarrow 4f$ emission at 100 K is composed of two broad bands (spectrum c). The band between 22320 and 360 nm is composed of two subbands as in K_2LaCl_5 . Spectrum (d) recorded with synchrotron radiation at 10 K shows the first band at 328 nm just before the instrumental limit was reached. The other band is assumed to be located around 345 nm, see Table II. In spectrum (d) we observe further bands between 250 and 280 nm. In the pure compound which contains trace impurities of Ce^{3+} , see spectrum (b), these bands are better resolved and clearly show two maxima at 257 and 266 nm. They are also attributed to fd transitions in Ce^{3+} , see Table II. The excitation peak at 294 nm in spectrum (c) may be related to an unknown impurity or to excitation of Ce^{3+} aggregates. The sharp decrease in excitation efficiency in spectrum (d) below 255 nm (5.0 eV) is attributed to the onset of the fundamental absorption of the host crystal, see Table I. This steep drop in the 10 K spectrum is less pronounced in the 100 K

spectrum because the energy transfer from the host lattice to Ce^{3+} ions becomes more efficient at elevated temperatures. The 5th Ce^{3+} fd excitation peak remains unidentified and is probably located at shorter wavelengths than the onset of the fundamental absorption at 250 nm.

The excitation spectrum of STE emission in pure K_2LaBr_5 , see Fig. 6 (b) and Fig. 8 (a), does not show clear thresholds and peaks which are required to determine E_{fa} , E_{ex} , and E_{CB} . This might be due to a poor efficiency of STE creation under across bandgap excitation, but also, due to the creation of impurity trapped excitons at energies below the fundamental absorption onset, since the nominally pure compounds contain impurities. In this case, the sharp drop in excitation efficiency of the Ce^{3+} doped compound at 255 nm marks E_{fa} .

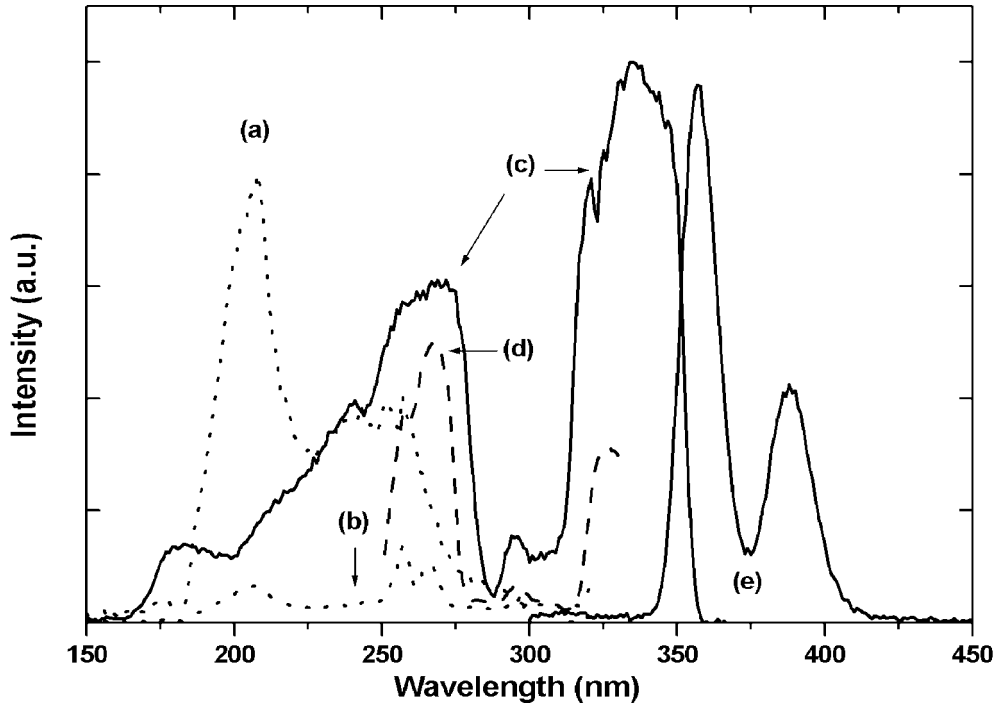


Fig. 8. Excitation and emission spectra of pure K_2LaBr_5 and $\text{K}_2\text{LaBr}_5:0.7\% \text{Ce}^{3+}$. (a) Slow (106 ns time gate) excitation spectrum of the 400 nm emission of undoped K_2LaBr_5 at 10 K. (b) Fast (27 ns time gate) excitation spectrum of the 355 nm emission of undoped K_2LaBr_5 at 10 K. (c) Time integrated excitation spectrum of the Ce^{3+} df emission at 388 nm of $\text{K}_2\text{LaBr}_5:0.7\% \text{Ce}^{3+}$ at 100 K. (d) Fast (27 ns time gate) excitation spectrum of the Ce^{3+} df emission at 388 nm of $\text{K}_2\text{LaBr}_5:0.7\% \text{Ce}^{3+}$ at 10 K. (e) Time integrated emission spectrum of $\text{K}_2\text{LaBr}_5:0.7\% \text{Ce}^{3+}$ upon 270 nm excitation at 100 K.

The excitation and emission spectra of $\text{K}_2\text{LaI}_5:0.7\% \text{Ce}^{3+}$ at 100 K are shown in Fig. 9. The emission spectrum (b) is dominated by the characteristic doublet of Ce^{3+} $5d \rightarrow 4f$ emission with peak positions at 399 and 437 nm. Accordingly, the spin-orbit splitting of the ground state of Ce^{3+} is 2180 cm^{-1} . The excitation spectrum (a) shows a broad band between 350 and 400 nm which resembles similar bands observed for K_2LaCl_5 and K_2LaBr_5 . Following the results for K_2LaCl_5 the broad band is attributed to an unresolved doublet located at approximately 365 and 380 nm, see Table II. The increasing excitation efficiency at wavelengths shorter than 320 nm (3.9 eV) is attributed to host lattice excitation.

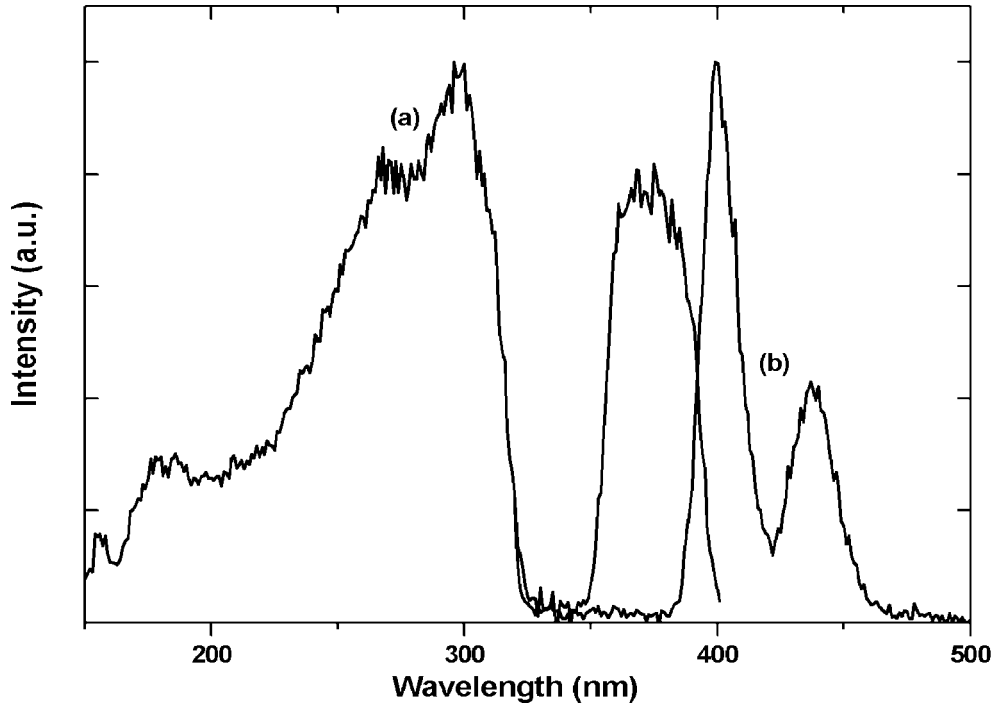


Fig. 9. (a) Excitation spectrum monitoring the Ce^{3+} emission at $\lambda = 440$ nm and (b) emission spectrum excited at $\lambda = 310$ nm of $\text{K}_2\text{LaI}_5:0.7\% \text{Ce}^{3+}$ at 100 K.

The optical properties of $\text{LaCl}_3:\text{Ce}^{3+}$ have already been published and were discussed in Chapter 6 [2,11]. Data are included to Tables I and II. Figure 10 shows the optical excitation (a) and emission (b) spectrum of $\text{LaBr}_3:0.5\% \text{Ce}^{3+}$. The $\text{Ce}^{3+} 5d \rightarrow 4f$ emissions are located at 355 and 390 nm, very similar to $\text{K}_2\text{LaBr}_5:\text{Ce}^{3+}$. The five $\text{Ce}^{3+} 5d$ levels at 260, 270, 284, 299, and 308 nm in the excitation spectrum of $\text{LaBr}_3:\text{Ce}^{3+}$ are nicely resolved, see Table II. Alike $\text{K}_2\text{LaCl}_5:\text{Ce}^{3+}$, just below the onset of the fundamental absorption E_{fa} at 238 nm (5.2 eV) a clear peak is observed at 244 nm which is attributed to impurity-trapped excitons. In the undoped LaBr_3 excitation spectrum (c) both the $\text{Ce}^{3+} fd$ bands and the impurity-trapped excitons are absent. $\text{LaI}_3:\text{Ce}^{3+}$ was studied too, but its spectroscopy is still incomplete. The two $\text{Ce}^{3+} df$ emission bands are located at 450 and 500 nm. The first fd excitation band of Ce^{3+} was detected at 420 nm but the four higher lying ones are above the fundamental absorption edge of LaI_3 at 3.2 eV and thus not accessible.

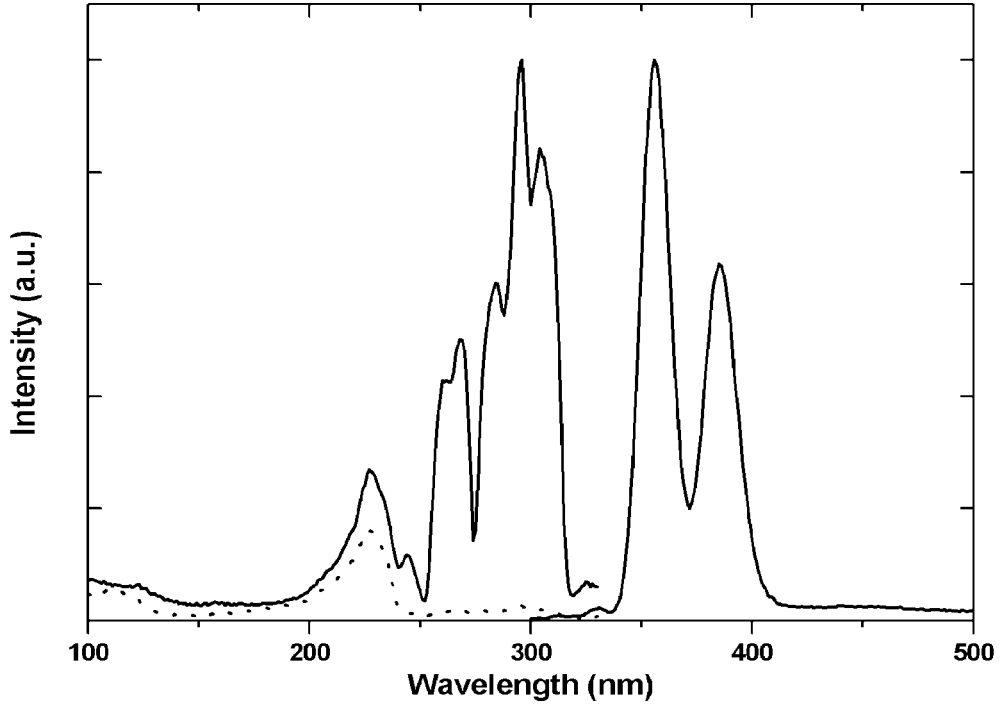


Fig. 10. (a) Excitation spectrum monitoring the Ce^{3+} emission at $\lambda = 360$ nm and (b) emission spectrum excited at $\lambda = 295$ nm of $\text{LaBr}_3:0.5\% \text{Ce}^{3+}$ at 10 K. For comparison the excitation spectrum of the STE emission in pure LaBr_3 is shown as well (c).

9.3.3 Scintillation decay

Scintillation decay spectra of K_2LaX_5 ($X = \text{Cl}, \text{Br}, \text{I}$) at room temperature, excited with gamma rays from a ^{137}Cs source are shown in Fig. 11. The rising slope before $t = 0$ is due to an experimental artifact and has no physical meaning. The spectra represent the luminescence intensity of the STE as function of time that decays exponentially. The lifetime of the STE decreases along the series $\text{Cl} \rightarrow \text{Br} \rightarrow \text{I}$, in accordance with former observation in the alkali halides [15]. It is about $3.7 \mu\text{s}$ in the chloride, $2.2 \mu\text{s}$ in the bromide, and 350 ns in the iodide. These lifetimes do not necessarily represent the intrinsic lifetime of the STE, but are rather the result of the quenching of STE luminescence at room temperature by energy migration to traps.

Figure 12 shows the scintillation decay spectra of (a) $\text{K}_2\text{LaCl}_5:0.1\% \text{Ce}^{3+}$ [8], (b) $\text{K}_2\text{LaBr}_5:0.7\% \text{Ce}^{3+}$, and (c) $\text{K}_2\text{LaI}_5:0.7\% \text{Ce}^{3+}$ at room temperature. In each case, the scintillation emission is a combination of much Ce^{3+} and few STE emission, see e.g. Fig. 3. For $\text{K}_2\text{LaCl}_5:0.1\% \text{Ce}^{3+}$ the scintillation decay profile closely resembles the spectrum of the pure compound. Despite the fact that most part of the emission originates from Ce^{3+} [9], the luminescence intensity decays exponentially with a slow decay time of about $3 \mu\text{s}$. We assume that this represents the lifetime of the STE involved in the energy transfer from the host lattice to Ce^{3+} . In the first 100 ns after the pulse, $\text{K}_2\text{LaCl}_5:0.1\% \text{Ce}^{3+}$ shows an additional decay component. Its contribution to the total luminescence intensity is rather small but it increases for higher Ce concentrations [9]. The scintillation decay of $\text{K}_2\text{LaBr}_5:0.7\% \text{Ce}^{3+}$ also consists of components. The faster one dominates the first μs and the slower one has a lifetime of $1.4 \mu\text{s}$. Again the latter represents the lifetime of the STE. Finally, $\text{K}_2\text{LaI}_5:0.7\% \text{Ce}^{3+}$ mainly shows a single fast exponential decay with a lifetime of $24 \pm 1 \text{ ns}$. It is characteristic for the parity allowed $\text{Ce}^{3+} 5d \rightarrow 4f$ transition. This fast decay

component contains more than 90% of the total luminescence intensity. Apparently, the scintillation decay rates of $\text{K}_2\text{LaX}_5:\text{Ce}^{3+}$ drastically increase along the halide series from Cl to I.

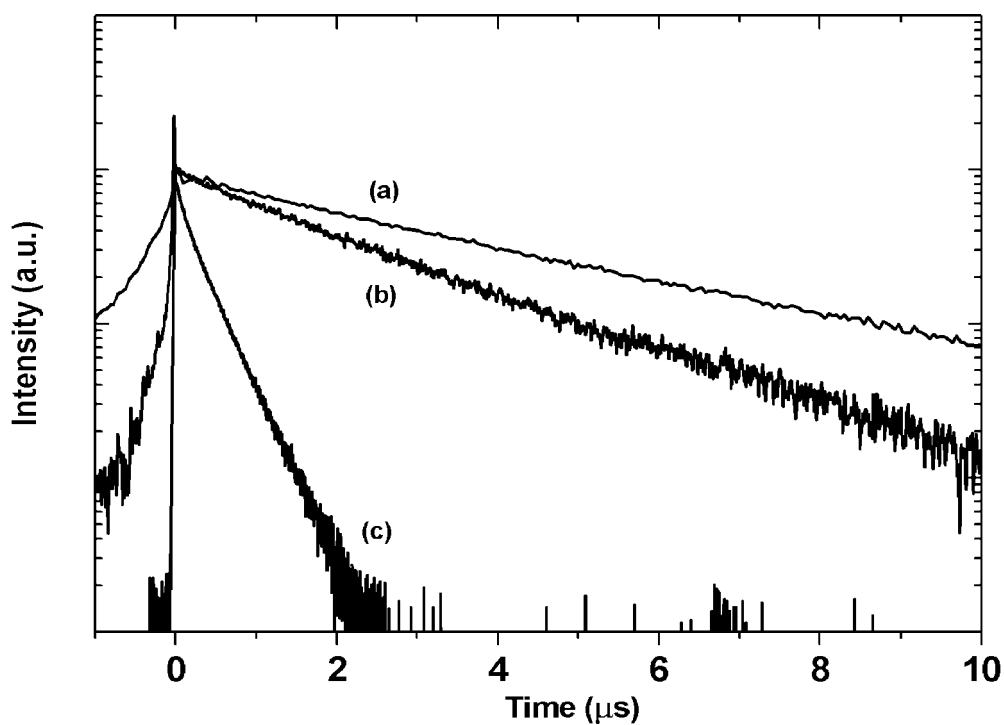


Fig. 11. Scintillation decay time spectra of undoped (a) K_2LaCl_5 , (b) K_2LaBr_5 , and (c) K_2LaI_5 at room temperature.

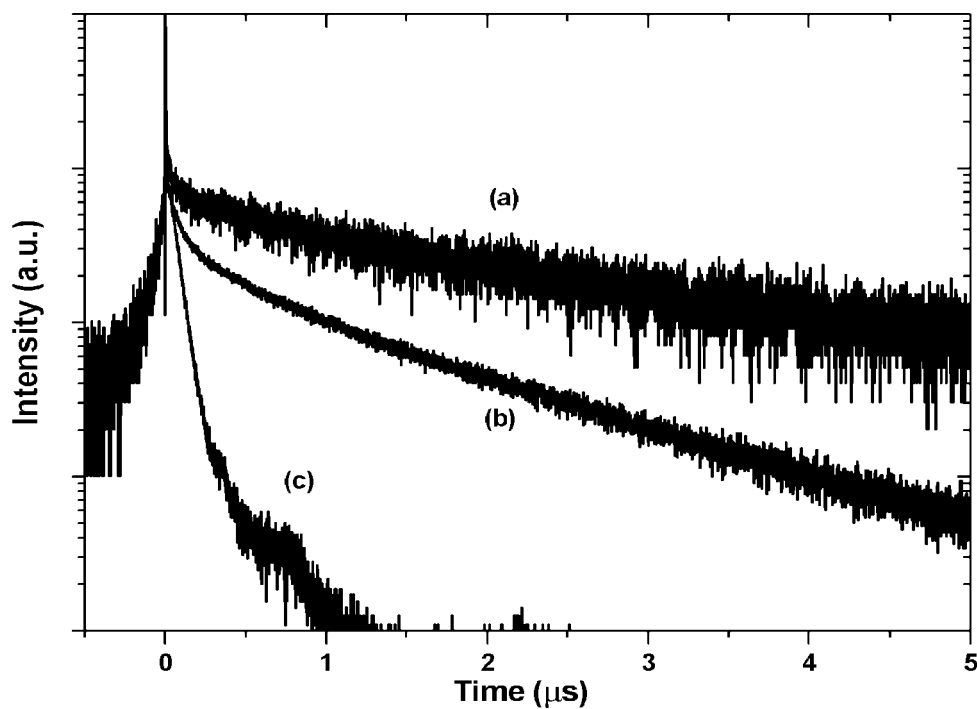


Fig. 12. Scintillation decay time spectra of (a) $\text{K}_2\text{LaCl}_5:0.1\% \text{Ce}^{3+}$, (b) $\text{K}_2\text{LaBr}_5:0.7\% \text{Ce}^{3+}$ and (c) $\text{K}_2\text{LaI}_5:0.7\% \text{Ce}^{3+}$ at room temperature.

9.4 Discussion

We first discuss the spectroscopy of the pure and Ce^{3+} doped compounds with special emphasis to the effects of anion variation. Next the scintillation properties of $\text{K}_2\text{LaX}_5:\text{Ce}^{3+}$ ($X = \text{Cl}, \text{Br}, \text{I}$) are discussed and compared with those of $\text{LaX}_3:\text{Ce}^{3+}$.

9.4.1 Spectroscopy

Table I compiles E_{fa} , E_{ex} , and E_{CB} of the undoped crystals of LaX_3 , KX , and K_2LaX_5 ($X = \text{Cl}, \text{Br}, \text{I}$). In addition the emission wavelength of the self-trapped exciton is given. One may notice the following trends. 1) All three energies decrease in the sequence $\text{Cl} \rightarrow \text{Br} \rightarrow \text{I}$. This is obviously related to the decreasing electron binding energy of the anion which is also expressed by the Pauling electronegativity χ , i.e. 3.16, 2.96, and 2.66 for Cl, Br, and I, respectively. 2) The tabulated energies of the alkali halides are larger than for the lanthanide halides. This must be attributed to the different Madelung potential at the trivalent La^{3+} site as compared to that at the monovalent K^+ site. 3) The energies of the K_2LaX_5 materials resemble those of LaX_3 . This illustrates that the bottom of the conduction band in both type of materials is formed by La^{3+} orbitals. 4) The exciton binding energy $E_{CB} - E_{ex}$ decreases in the sequence $\text{Cl} \rightarrow \text{Br} \rightarrow \text{I}$. This also holds for the alkali halides involving Li, Na, Rb, and Cs [12]. It is caused by the increasingly larger polarizability of the anion leading to a screening of the hole component of the exciton and larger effective mass m^* of the hole. Although it can not be verified from the results in Table I, we expect for LaX_3 and K_2LaX_5 a similar behaviour.

Despite that the exciton peak E_{ex} shifts 2-3 eV with type of anion in each class of compound, the position of the STE emission band does not change more than 0.4 eV in K_2LaX_5 (see Fig. 1) and LaX_3 . Also in the alkali halides the anion does not have a large influence on the STE emission. Change of alkali cation from Na^+ to K^+ or Rb^+ has a much larger influence on the position of the STE emission band [15]. In these systems the energy of the STE emission band tends to decrease in the series Na^+ to K^+ to Rb^+ . On the other hand, it has been observed by Ohno [16] that in the ammonium halides NH_4X the energy of the STE emission band shifts about 1.2 eV towards lower energy in the series $\text{Cl} \rightarrow \text{Br} \rightarrow \text{I}$. The Stokes shift between STE emission and E_{ex} tends to decrease from 2.6 eV in the chloride, 2.1 eV in the bromide and 1.7 eV in the ammonium iodide.

In general, the position of the STE emission band is correlated with the amount of off-centre relaxation of the V_K core of the STE [4,17]. This can be achieved by a lattice distortion which involves the expulsion of the V_K core away from the electron. It results in an axial shift of the STE away from its original, on-centre position. The larger the axial shift, the larger the Stokes shift and the smaller the energy of the STE emission band. See also Chapter 5.

The STE emission bands in the alkali halides have been classified into three categories called I, II, and III, in order of increasing Stokes shift [15]. A more physical basis for the categorisation was given by Song [18] who showed that the amount of off-centre relaxation of the STE in the alkali halides can be correlated with the Rabin-Click parameter S/D , where S is defined as the separation of two adjacent halide ions along a $\langle 110 \rangle$ row minus twice the halide-ion radius, and D the diameter of the halogen atom [19]. Unfortunately, the Rabin-Click parameter only applies to cubic systems and its strict definition prevents the use in crystal systems of lower symmetry like LaX_3 and K_2LaX_5 .

For KCl, KBr, and KI, the Stokes shift of the triplet STE emission band is 5.4, 4.5, and 2.5 eV, respectively [12]. The large Stokes shift in KCl and KBr indicates that substantial lattice relaxation occurs in the creation of the STE. In KCl and KBr, STEs are formed with substantial off-centre relaxation of the STE. In KI the STE is probably situated in an on-centre configuration. In the case of K_2LaCl_5 and K_2LaBr_5 , the Stokes shift of the STE emission band is slightly larger than in the case of KI. It suggests therefore that the STE in K_2LaCl_5 and K_2LaBr_5 experiences only a small degree of off-centre relaxation. In many respects the parameters of the undoped LaX_3 and K_2LaX_5 compounds in Table I are very similar. This applies to the energy of the exciton peaks, the Stokes shift and the wavelength of STE emission. However, the parameters are much different from those in the KX compounds. Apparently the trivalent lanthanide common to LaX_3 and K_2LaX_5 is responsible for this.

For the free Ce^{3+} ion, the $5d$ configuration is located at average energy of 51230 cm^{-1} [1]. Due to the spin-orbit interaction two energy levels, i.e., $^2D_{3/2}$ and $^2D_{5/2}$, are observed. In a crystalline environment, the average energy of the $5d$ configuration is reduced by the centroid shift, ϵ_c . Depending on the site symmetry the degeneracy might be lifted and up to five distinct $5d$ energy levels are obtained. The energy difference between the lowest and highest $5d$ level defines the total crystal field splitting, ϵ_{cfs} . Table II compiles the wavelengths λ_i of the five $4f \rightarrow 5d$ excitation bands of Ce^{3+} in the LaX_3 and K_2LaX_5 compounds.

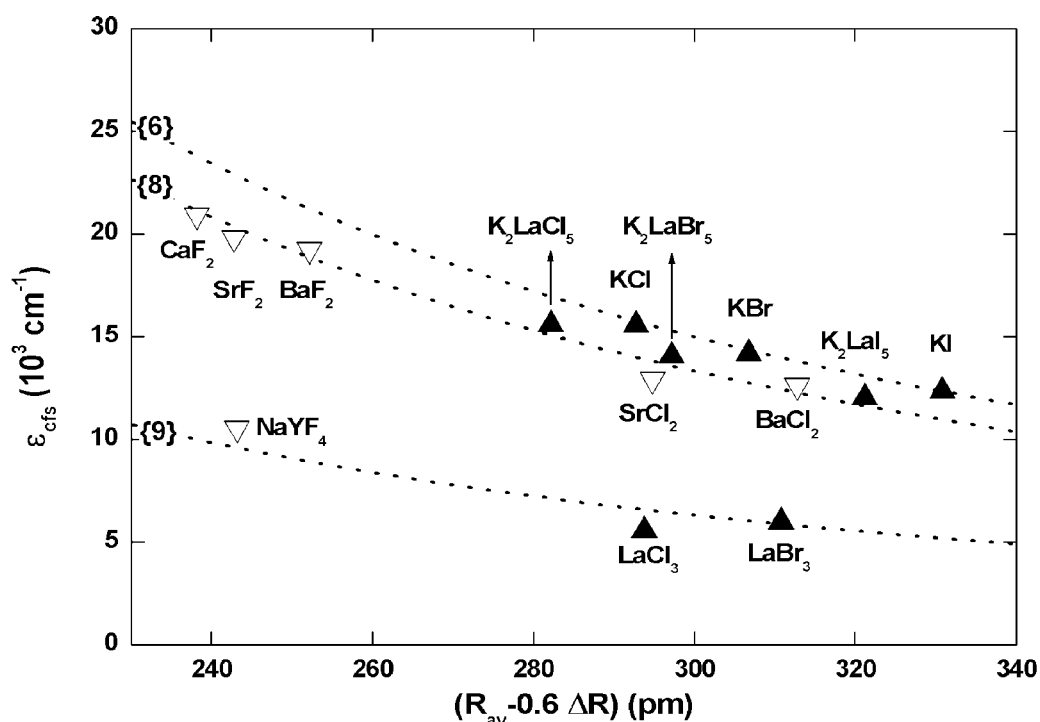


Fig. 13. The crystal field splitting ϵ_{cfs} of the Ce^{3+} $5d$ configuration in halides as function of the average distance to neighbouring anions in the relaxed lattice for octahedral {6}, cubic {8}, and tricapped trigonal prism {9} co-ordination.

Figure 13 illustrates how the $5d$ crystal field splitting in Ce^{3+} varies as function of Ce^{3+} co-ordination. The size of the polyhedron is modelled by the average distance R_{av} of the cation to the N co-ordinating anions. A correction of $0.6\Delta R$ was applied to account for the lattice relaxation. ΔR is defined as the difference in ionic radius

between Ce^{3+} and the cation it substitutes for. It amounts to 2, 3, and 37 pm for LaX_3 , K_2LaX_5 , and KX , respectively. Empirically, ε_c can be modelled by equation (1)

$$\varepsilon_{cfs} = \beta_{poly} R_{av}^{-2} \quad (1)$$

where β_{poly} is a constant depending on the co-ordination polyhedron [3]. The validity of Eq. (1) is demonstrated for KX with octahedral {6} co-ordination as well as for CaF_2 , SrF_2 , BaF_2 , SrCl_2 , and BaCl_2 with cubic {8} co-ordination, and NaYF_4 , LaCl_3 , and LaBr_3 with tricapped trigonal prismatic {9} co-ordination. See dashed lines in Fig. 13.

The total crystal field splitting in K_2LaX_5 is about the same as the value typical for cubic co-ordination, see Fig. 13. Information on K_2LaBr_5 and K_2LaI_5 is still incomplete, but reasonable estimates for the missing $5d$ level energies can be given. The type of co-ordination polyhedron in the K_2LaX_5 compounds are the same, and then an R^{-2} dependence with polyhedral size is expected. Employing Eq. (1) the total crystal field splitting and from that the wavelengths of the missing $5d$ bands were estimated. They are given together with the values for the centroid shift ε_c within brackets in column 4, 5, and 6 of Table II.

Information is not available on the energy of Ce^{3+} $5d$ levels in the KX type of compounds. However, it can be estimated from results available on the energies of the $4f^6 5d$ levels of Eu^{2+} in these compounds. The $5d$ levels of Eu^{2+} at sites of octahedral symmetry are split into a low energy triplet and a high energy doublet state separated by an energy known as the $10Dq$ value which can be set equal to ε_{cfs} . From previous studies it is known that, provided that the polyhedral size and shape around Eu^{2+} and Ce^{3+} are the same, the crystal field splitting in Eu^{2+} is about 0.77 times that in Ce^{3+} . Using this ratio, the data anticipated for Ce^{3+} doped KX compounds is drawn in Fig. 13.

We now observe that the (anticipated) crystal field splitting in the K_2LaX_5 compounds falls between that of octahedral and cubic co-ordination. This agrees with the general trend of decreasing crystal field splitting with larger co-ordination number N around Ce^{3+} . It is largest for octahedral co-ordination with $N = 6$. Provided that the so-called prismatic angle remains the same, the crystal field splitting for a trigonal prism co-ordination is the same as for octahedral co-ordination [3,20]. Adding one capping anion on one of the three side faces of a trigonal prism, as in K_2LaX_5 , leads to a smaller crystal field splitting, but apparently still somewhat larger than that of cubic co-ordination. When all three side-faces of the trigonal prism are capped with an anion one obtains the situation in NYF_4 , LaCl_3 , and LaBr_3 with much reduced crystal field splitting. Note that the changing chemical properties of the anions in the sequence Cl, to Br, to I are not important for the crystal field splitting. Only the change in ionic radius appears via R_{av} in Eq. (1).

On the other hand, for fluorides, chlorides, bromides, and iodides, ε_c is typically 6000 cm^{-1} , 14000 cm^{-1} , 16000 cm^{-1} , and 19000 cm^{-1} , respectively. This is also revealed in Table II.

9.4.2 Scintillation

As can be seen from Fig. 11, the lifetime of the STE tends to become shorter in the series $\text{Cl} \rightarrow \text{Br} \rightarrow \text{I}$. This can be satisfactorily accounted for in terms of the larger spin-orbit interaction in heavier halides [21]. The smaller values for the lifetime of the STE can also be explained by the increasing thermally activated hopping rate of the

STE in the series Cl \rightarrow Br \rightarrow I [22, 23]. It leads to quenching of STE emission and decreasing lifetime due to the energy transfer to Ce³⁺. See also chapter 5, Table II.

In principle, there are several energy transfer mechanisms possible that may account for the observed correlation between the decay time of the scintillation pulse and the type of anion. In the case of *STE diffusion*, the luminescence of K₂LaX₅:Ce³⁺ (X = Cl, Br, I) at low temperatures is largely due to the radiative recombination of the STE, see Fig. 3. However, as the temperature rises the mobility of the STE increases as well and the energy is transferred to a Ce³⁺ centre when the STE encounters a Ce³⁺ ion. Such an energy transfer can explain the observed anti-correlation of Ce³⁺ and STE luminescence intensity in Figs. 4 and 5 between 100 and 400 K. If we consider the migration of a V_K centre through the lattice, the activation energy for V_K diffusion decreases from Cl to Br to I. In the same order the mobility of the STE increases (see chapter 5, section 4). Indeed, the scintillation decay time decreases from K₂LaCl₅:0.1% Ce³⁺ [9] to K₂LaBr₅:0.7% Ce³⁺ to K₂LaI₅:0.7% Ce³⁺ (see Fig. 12).

9.5 Conclusions

In this chapter the spectroscopic and scintillation properties of undoped and Ce³⁺ doped K₂LaX₅, LaX₃, and KX (X = Cl, Br, I) have been determined and compared with each other. The bandgap E_{CB} , the energy of the exciton peak E_{ex} , and the wavelength of STE emission λ_{STE} are very similar for K₂LaX₅ and LaX₃, but much different from KX. The conduction band levels of La³⁺ are at 1-2 eV lower energy than those of K⁺. The decreasing binding strength for electrons along the halide series results in a bandgap reduction of about 2 eV from Cl to I in each series of compounds.

The energy of the five *fd* transitions of Ce³⁺ in LaX₃ and K₂LaX₅ compounds were determined by excitation and emission spectroscopy. The highest energy transitions of K₂LaBr₅ and K₂LaI₅ are observed by the fundamental absorption of the host crystals. For those cases the energies were estimated based on empirical data from other Ce³⁺ doped compounds. Since Ce³⁺ doped KX has not been studied, the energies of the *5d* bands were derived from Eu²⁺ doped compounds. For a given Ce³⁺ co-ordination, the increasing ionic radius of the anions from Cl to I causes a 20% decrease of the crystal field splitting. On the other hand, the centroid shift of the *5d* configuration increases in the sequence Cl to Br to I due to larger covalency between anion and Ce³⁺ and due to higher polarizability of the anion.

Across the bandgap excitations either by X-rays, γ -rays or synchrotron radiation result in a combination of Ce³⁺ *5d* \rightarrow *4f* and STE emission. The ratio of Ce³⁺ against STE emission intensity depends on temperature and Ce concentration. Clear trends are observed. For low concentrations of 0.2-0.5% and increasing temperature from 100 to 400 K, the Ce³⁺ emission gains intensity against the STE emission. This is very clear for LaCl₃ and K₂LaCl₅ where the STE emission dominates at 100 K. The energy of the STE is fully transferred to Ce³⁺ at 400 K and only Ce³⁺ emission is observed [9,10]. At room temperature both emissions are still present. Along the series Cl, Br, I the intensity of the Ce³⁺ emission increases at the expense of STE emission. In LaBr₃ and K₂LaI₅ with 0.2-0.5% Ce³⁺ the STE emission is very weak at room temperature and only fast Ce³⁺ *df* emission is observed. These two compounds provide efficient and fast scintillators already at small Ce concentrations. LaCl₃ and K₂LaCl₅ are fast and efficient scintillators only when the Ce concentration is increased above 10%. The increase of Ce³⁺ scintillation efficiency and scintillation speed along the series

from Cl to I is attributed to 1) an increasing hopping mobility of STEs and 2) the higher trapping rate of free electrons and holes by Ce^{3+} relative to STE creation rate.

References

- ¹ P. Dorenbos, Phys. Rev. B 62 (2000) 15640.
- ² P. Dorenbos, Phys. Rev. B 62 (2000) 15650.
- ³ P. Dorenbos, J. Alloy Comp. 341 (2002) 156.
- ⁴ R.T. Williams, K.S. Song, J. Phys. Chem. Sol. 51 (1990) 679.
- ⁵ J.B. Reed, B.S. Hopkins, L.F. Audrieth, Inorg. Synth. 1 (1936) 28.
- ⁶ G. Meyer, Inorg. Synth. 25 (1989) 146.
- ⁷ G Meyer, "Synthesis of Lanthanide and Actinide Compounds," Eds.: G. Meyer and L. Morss (Kluwer, Dordrecht, 1991), p. 145.
- ⁸ G. Meyer, J. Soose, A. Moritz, V. Vitt, Th. Holljes, Z. anorg. allg. Chem. 521 (1985) 161.
- ⁹ J.C. van't Spijker, P. Dorenbos, C.W.E. van Eijk, K. Krämer, H.U. Güdel, J. Lumin. 85 (1999) 1.
- ¹⁰ O. Guillot-Noël, J.T.M. de Haas, P. Dorenbos, C.W.E. van Eijk, K. Krämer, H.U. Güdel, J. Lumin. 85 (1999) 21.
- ¹¹ J. Andriessen, O.T. Antonyak, P. Dorenbos, P.A. Rodnyi, G.B. Stryganyuk, C.W.E. van Eijk, A.S. Voloshinovskii, Opt. Commun. 178 (2000) 355.
- ¹² K.S. Song, R.T. Williams, "Self-trapped exciton," M. Cardona (Ed.), Springer Series on Solid-State Sciences no. 105, Springer, Heidelberg, 1993.
- ¹³ J.A. Hernandez, F.J. Lopez, H.S. Murrieta, J.O. Rubio, J. Phys. Soc. Jpn. 50 (1981) 225.
- ¹⁴ M.G. Aguilar, J.O. Rubio, F.J. Lopez, J. Garcia-Sole, H. Murrieta, Sol. St. Commun. 44 (1982) 141.
- ¹⁵ K. Kan'no, K. Tanaka, T. Hayashi, Review Sol. St. Sci. 4 (1990) 383.
- ¹⁶ N. Ohno, M. Itoh, S. Hashimoto, J. Lumin. 53 (1992) 121.
- ¹⁷ K.S. Song, C.H. Leung, J. Phys. Condens. Matter 1 (1989) 8425.
- ¹⁸ K.S. Song, C.H. Leung, R.T. Williams, J. Phys. Condens. Matter 1 (1989) 683.
- ¹⁹ H. Rabin, C.C. Klick, Phys. Rev. 117 (1960) 1005.
- ²⁰ C. Görller-Walrand, K. Binnemans, "Handbook on the Physics and Chemistry of Rare Earths," K.A. Gschneidner, Jr. and L. Eyring (Eds.), vol. 23, Elsevier Science B.V., Amsterdam, 1996, chapter 155.
- ²¹ M.N. Kabler, and D.A. Patterson, Phys. Rev. Lett. 19 (1967) 652.
- ²² L.F. Chen, K.S. Song, and C.H. Leung, Nucl. Instr. Meth. Phys. Res. B 46 (1990) 216.
- ²³ K. Tanimura, and N. Itoh, J. Phys. Chem. 42 (1981) 901.

Conclusions

Two major questions are of importance for scintillation. The first question, whether it is possible to predict certain scintillation properties of new inorganic scintillators in advance, by knowing for instance the crystallographic properties of the matrix, may be answered affirmative. Extensive work by P. Dorenbos [1-3] has shown that in principle it is possible to predict the luminescence of Ce^{3+} and other trivalent lanthanides in several hosts. The wavelength of emission, the position of the $5d$ levels and whether it is possible for the trivalent lanthanide to capture an electron or hole has been investigated. Results presented in chapters 6 – 9 of this thesis confirm this phenomenological model.

The emphasis of the second part of this thesis was dedicated to the second question, whether there is a theoretical model that can describe and predict the scintillation mechanism of new inorganic scintillators. Clear trends have been observed which we will discuss briefly below.

At room temperature, the energy transfer mechanisms *direct capture of electron-hole pairs* and *STE diffusion* were held dominant in $\text{LaCl}_3:\text{Ce}^{3+}$, $\text{K}_2\text{LaCl}_5:\text{Ce}^{3+}$ and in $\text{LaBr}_3:\text{Ce}^{3+}$, $\text{K}_2\text{LaBr}_5:\text{Ce}^{3+}$ and $\text{K}_2\text{LaI}_5:\text{Ce}^{3+}$. In these materials, Ce^{3+} substitutes for La^{3+} ($r_{\text{Ce}^{3+}}/r_{\text{La}^{3+}} \approx 1$). From a defect perspective, there is no difference between the undoped and the Ce^{3+} doped compound and the potential well due to strain in the lattice is virtually absent. Thus, it is assumed that the pathways for STE formation are not significantly altered from the undoped to the Ce^{3+} doped materials. If STEs are readily formed and energy transfer is possible between the STE and Ce^{3+} $5d$ levels (located below the conduction band), *STE diffusion* is the most likely scintillation mechanism in addition to *direct capture of electron-hole pairs* by Ce^{3+} .

In contrast, *binary electron-hole diffusion* is the model that describes the scintillation mechanism in $\text{Cs}_2\text{LiYCl}_6:\text{Ce}^{3+}$, $\text{Cs}_2\text{LiYBr}_6:\text{Ce}^{3+}$, $\text{LuCl}_3:\text{Ce}^{3+}$ and $\text{LuBr}_3:\text{Ce}^{3+}$ best. In these systems, the introduction of Ce^{3+} on a smaller cationic site, e.g. $r_{\text{Ce}^{3+}}/r_{\text{Lu}^{3+}} \approx 1.15$, can create a potential well for the trapping of holes or electrons due to strain in the lattice. However, *STE diffusion* may still play a role in the scintillation mechanism provided that the STE can transfer its energy to the Ce^{3+} $5d$ levels (located below the conduction band). This is probably not possible in $\text{LuCl}_3:\text{Ce}^{3+}$ and $\text{LuBr}_3:\text{Ce}^{3+}$. In these compounds, the lattice leaves ample room for the off-centre relaxation of the STE. It results in a large Stokes shift and stabilisation of the STE, leading to diminished Ce^{3+} luminescence and slow STE emission. In the case of $\text{LaCl}_3:\text{Ce}^{3+}$, $\text{LaBr}_3:\text{Ce}^{3+}$ and $\text{K}_2\text{LaX}_5:\text{Ce}^{3+}$ ($X = \text{Cl}, \text{Br}, \text{I}$) the STE is probably in an (nearly) on-centre position.

The influence of the anion on the scintillation properties is substantial. It has been shown for all compounds that in the series Cl to Br to I, the lifetime of the STE decreases due to the larger spin-orbit coupling of the groundstate of the STE in the heavier halides. But also the energy of the Ce^{3+} emission band decreases in the same sequence. The increase of Ce^{3+} scintillation efficiency and scintillation speed when the anion changes from Cl to Br to I, is (a) related with an increasing hopping motion of the STE, (b) related with an increasing rate of V_K diffusion and (c) related with the trapping rate of free electrons and holes by Ce^{3+} becomes increasingly larger relative to the STE creation rate.

In summary:

- (a) The scintillation mechanism is determined by the host. The type of indigenous cation and the amount of relaxation of the V_K centre or/and STE determines the type of scintillation mechanism.
- (b) The diffusion rate of the V_K centre and the STE is determined by the anion. It increases in the sequence Cl to Br to I.
- (c) The wavelength of the Ce^{3+} emission band increases in the sequence Cl to Br to I.
- (d) The probability of hole capture by Ce^{3+} also increases in the sequence Cl to Br to I.
- (e) The presence of afterglow, the trapping of electrons and holes, and the axial shift of the STE all depend on the amount of traps and the possibility of substantial (off-centre) relaxation in the lattice. However, the temperature at which the holes (V_K centres) become mobile again decreases in the series Cl to Br to I.

The points mentioned above may be applied in future research on inorganic scintillators and materials in which Ce^{3+} substitutes for the indigenous cation. Energy transfer by *STE diffusion* may be found dominant in compounds where Ce^{3+} substitutes for La^{3+} , e.g. Rb_2LaBr_5 [4], while energy transfer by *binary electron-hole diffusion* may be found dominant in compound where Ce^{3+} substitutes for Lu^{3+} and Y^{3+} , e.g. YCl_3 [5] and LuI_3 [6]. Experiments like electron-paramagnetic resonance and photo-conductivity measurements can be applied to give a decisive answer about the validity of these predictions.

As for application, it was shown that both $LaCl_3:Ce^{3+}$ and $LaBr_3:Ce^{3+}$ have good scintillation properties. Both combine a high light yield with excellent energy resolution and a fast luminescence decay. But also $K_2LaI_5:Ce^{3+}$ is a promising scintillator. The density and effective Z of K_2LaI_5 are comparable to those of $LaBr_3$, and $K_2LaI_5:Ce^{3+}$ provides efficient and fast scintillation already at small Ce concentrations. However, the energy resolution at 662 keV of $\sim 5\%$ is worse than that of $LaCl_3:Ce^{3+}$ and $LaBr_3:Ce^{3+}$. It is probably related with the quality of the crystal. Additionally, K_2LaI_5 contains the radioactive isotope ^{40}K which makes $K_2LaI_5:Ce^{3+}$ less suitable than, e.g., $LaCl_3:Ce^{3+}$ and $LaBr_3:Ce^{3+}$, for use in gamma cameras and other dedicated applications.

Since it seems that all halide scintillators based on La^{3+} are very good scintillators, it might be worthwhile to investigate the analogues of $LaCl_3:Ce^{3+}$ and $LaBr_3:Ce^{3+}$ as well, i.e. $LaI_3:Ce^{3+}$, $Rb_2LaBr_5:Ce^{3+}$, $CsLa_9I_{28}:Ce^{3+}$, etc.

References

- ¹ P. Dorenbos, Phys. Rev. B 62 (2000) 15640.
- ² P. Dorenbos, Phys. Rev. B 62 (2000) 15650.
- ³ P. Dorenbos, J. Alloy Compounds 341 (2002) 156.
- ⁴ H.J. Seifert, Y. Yuan, J. Less-Com. Met. 170 (1991) 135.
- ⁵ D.H. Templeton, G.F. Carter, J. Phys. Chem. 58 (1954) 940.
- ⁶ A.G. Dudareva, S.B. Nechitailov, T.A. Babushkina, K.Yu. Volgin, A.A. Boguslavskii, Russ. J. Inorg. Chem. 34 (1989) 1809.

Summary

This thesis is dedicated to scintillator research and in particular, to the search for new inorganic scintillators. Two topics are explored: (i) the search for new inorganic scintillators for gamma ray detection and (ii) the systematic research of the scintillation mechanisms in scintillator materials.

Scintillators have been used for decades to make ionising radiation visible. Either by direct observation of the light flash of the material when exposed to radiation, or indirect by use of a photomultiplier tube or photodiode. Despite the enormous amount of commercially available scintillators, the ideal scintillator that combines a high light yield, a high density, a fast decay, and good energy resolution has yet to be found. The subject is introduced in chapter 1. The techniques used to study the scintillating materials are described in chapter 2. In Table I, the scintillation properties of the studied compounds are compiled.

Table I. Scintillation properties of the studied compounds.

Compound	Z_{eff}	ρ (g/cm ³)	[Ce ³⁺] (%)	λ (nm)	Light Yield (10 ³ ph/MeV)	Energy resolution R (%, @ 662 keV)	Principal decay τ (ns)
LaCl ₃	49.5	3.86	0.57	330	40 ± 4	7.0 ± 0.5	20 (8%)
			2		49 ± 1	3.5 ± 0.1	27 (10%)
			4		49 ± 1	3.5 ± 0.1	25 (18%)
			10		49 ± 1	3.3 ± 0.1	25 (41%)
			30		43 ± 1	3.3 ± 0.1	25 (69%)
CeCl ₃	50	3.9	-	335	46 ± 4	4.5 ± 0.5	25 (69%)
LaBr ₃	46.9	5.29	0.5	358	61 ± 5	2.8 ± 0.2	31
			2		48 ± 5	3.8 ± 0.4	31
			4		48 ± 5	3.5 ± 0.4	31
			10		45 ± 5	3.9 ± 0.4	31
Cs ₂ LiYCl ₆		3.31	0.5	376	18 ± 2	7 ± 1	390 + slow
Cs ₂ LiYBr ₆		4.15	1.0	388	25 ± 3	6 ± 1	72 + slow
LuCl ₃	63.1	4.00	0.45	374	6.6 ± 0.6	18.0 ± 0.5	110 (87%)
			2		6.4 ± 0.6	13.8 ± 0.5	85 (73%)
			4		5.4 ± 0.5	11.4 ± 0.4	76 (91%)
			10		6.4 ± 0.6	11.7 ± 0.4	88 (81%)
LuBr ₃	62.6	5.17	0.021	408	29 ± 3	8.6 ± 0.5	~10 ³
			0.46		18 ± 2	7.8 ± 0.3	32 (10%)
			0.76		26 ± 3	6.5 ± 0.5	32 (15%)
			2.5		19 ± 2	6.2 ± 0.2	20 (31%)
			8		16 ± 1	6.0 ± 0.1	19 (33%)
K ₂ LaCl ₅	44.1	2.9	0.7	344	21 ± 3	-	~10 ³
			10		30 ± 5	5.1 ± 0.5	~10 ³
K ₂ LaBr ₅	42.8	3.9	0.7	359	26 ± 3	7.5 ± 0.8	~10 ³
			10		40 ± 4	4.9 ± 0.5	~10 ²
K ₂ LaI ₅	52.4	4.4	0.7	401	52 ± 5	5.0 ± 0.5	24
			10		57 ± 6	4.2 ± 0.4	24

The first topic, the search for new inorganic scintillators and their application is covered in part A. Chapter 3 reviews some medical imaging applications and the most commonly used scintillators in that field. Next, the basic scintillator requirements for some medical imaging applications are reviewed and the properties of some new inorganic scintillator materials are presented. Finally, the choice of the studied compounds is motivated whilst attention is focussed on existing oxide and halide scintillators.

In chapter 4, two new inorganic scintillators, $\text{LaCl}_3:\text{Ce}^{3+}$ and $\text{LaBr}_3:\text{Ce}^{3+}$, are presented. Under optical and gamma ray excitation, Ce^{3+} emission is observed to peak at 330 and 352 nm in the chloride, and at 356 and 387 nm in the bromide. Both combine a high light yield with excellent energy resolution and a fast luminescence decay. The scintillation light yield is 49000 ± 1000 and 61000 ± 5000 photons/MeV for $\text{LaCl}_3:10\% \text{Ce}^{3+}$ and $\text{LaBr}_3:0.5\% \text{Ce}^{3+}$, respectively. In the chloride, 40% is emitted with a decay time of 26 ns, whereas more than 90% is emitted with a decay time of 35 ns in the bromide. Energy resolutions of about 3% (full width half maximum over peak position) were observed for the 662 keV full absorption peak. For applications where a good energy resolution is required in combination with fast scintillation, both $\text{LaCl}_3:\text{Ce}^{3+}$ and $\text{LaBr}_3:\text{Ce}^{3+}$ may be a very good choice.

Part B of this thesis is concerned with the systematic research of the scintillation mechanisms. The scintillation process, the formation of electrons and holes after absorption of radiation, and the energy transfer are introduced and discussed in chapter 5.

The scintillation mechanism of $\text{LaCl}_3:\text{Ce}^{3+}$ and $\text{LaBr}_3:\text{Ce}^{3+}$ is subject of chapter 6. However, a detailed investigation has only been commenced for the chloride. In both materials, self-trapped excitons (STEs) play an important role. In $\text{LaCl}_3:\text{Ce}^{3+}$ STE diffusion is the dominant scintillation mechanism. It explains the observed anti-correlation between Ce^{3+} and STE luminescence under X-ray excitation as function of temperature, the presence of STEs in EPR spectra of $\text{LaCl}_3:\text{Ce}^{3+}$ and the absence of stable V_K centres. For $\text{LaBr}_3:\text{Ce}^{3+}$ it was assumed that the V_K centres immediately recombine with an electron to form an STE. High speed STE diffusion to Ce^{3+} is then the dominant scintillation mechanism. However, Ce^{3+} could also capture a free electron and hole from the conduction and valence band, respectively, leading to fast Ce^{3+} luminescence.

In chapter 7, the influence of the anion on the scintillation properties of the elpasolites, $\text{Cs}_2\text{LiYX}_6:\text{Ce}^{3+}$ ($X = \text{Cl}, \text{Br}$), is discussed. Elpasolites are model systems investigated in numerous optical, scintillation and magnetic studies. They have the advantage over many other crystalline systems that the M^{3+} site, located at the centre of a regular octahedron of halide ions X , offers a natural environment for the incorporation of Ce^{3+} and other trivalent ions. These materials are of particular interest because of the possible presence of core-valence (CV) luminescence. It is shown that only pure $\text{Cs}_2\text{LiYCl}_6$ exhibits CV luminescence, due to the position of the valence band with respect to the 5p core band of Cs. Under X-ray excitation, Ce^{3+} doped elpasolites show intense Ce^{3+} luminescence in addition to residual STE emission. The light yield as a function of temperature is best described as a bell-shaped curve that has a correlation with the production of F centres. In both materials, *binary electron – hole diffusion* is the dominant scintillation mechanism. It appears that the influence of the anion does not effect the scintillation mechanism. However, the lifetime of the STE tends to decrease from Cl to Br.

In chapter 8, the properties and mechanism of scintillation in $\text{LuCl}_3:\text{Ce}^{3+}$ and $\text{LuBr}_3:\text{Ce}^{3+}$ crystals are discussed. It is shown that at room temperature, *energy transfer by binary electron hole diffusion* is the dominant mechanism in these materials. At lower irradiation temperatures, V_K diffusion is probably more important. For both LuCl_3 and LuBr_3 , the crystal structure leaves ample room for the off-centre relaxation of the V_K core of the STE. As a result, a low light yield is observed for the chloride. Doping with Ce decreases the light yield of the bromide considerably.

Chapter 9 is concerned with the influence of the anion on the scintillation and spectroscopy of the pure and Ce^{3+} -doped ternary halides K_2LaX_5 ($X = \text{Cl}, \text{Br}, \text{I}$). The properties are compared with those of LaX_3 and KX . In this system the crystal structure remains essentially unchanged, whereas the chemical environment is altered by means of the variation $X = \text{Cl}$ to Br to I . The bandgap, the energy of the exciton peak and the wavelength of STE emission are very similar when comparing K_2LaX_5 with LaX_3 , but very different when comparing with KX . The chemical properties of the anions have a profound influence on the scintillation and spectroscopy of K_2LaX_5 . In the sequence Cl to Br to I , the centroid shift of the $5d$ configuration increases due to the larger covalency between the anion and Ce^{3+} and due to the larger polarizability of the anion. In K_2LaX_5 , but especially in $\text{K}_2\text{LaCl}_5:\text{Ce}^{3+}$, STEs play an important role. Again, an anti-correlation is observed between Ce^{3+} and STE emission. In the series Cl to Br to I , the intensity of the Ce^{3+} emission increases at the expense of STE emission. Also the efficiency and scintillation decay rate increase from Cl to Br to I . It is related with (a) the increasing hopping motion of the STE and (b) the trapping rate of free electrons and holes by Ce^{3+} .

Samenvatting

Dit proefschrift is gewijd aan scintillatie onderzoek en in het bijzonder aan het onderzoek van nieuwe, anorganische scintillatoren. Er worden twee onderwerpen uit het scintillatie onderzoek belicht: (i) het vinden van nieuwe, anorganische scintillatoren voor gamma detectie en (ii) het onderzoek van het scintillatie-mechanisme in verschillende materialen. Scintillatoren worden al sinds lange tijd gebruikt om de onzichtbare, ioniserende straling zichtbaar te maken (detecteren). Dit kan gebeuren door de observatie van een lichtflitsje (uit het Latijn: “*scintilla*”) dat de scintillator uitzendt tijdens de blootstelling aan straling, of indirect, door de scintillator in combinatie met een photomultiplicatorbuis of diode te gebruiken. Ondanks de enorme keuze uit de commercieel beschikbare scintillatoren blijft er vraag naar nieuwe anorganische scintillatoren die een hoge licht opbrengst combineren met een hoge dichtheid, een snelle luminescentie en een goede energie resolutie. Het onderwerp scintillatie en scintillatoren wordt geïntroduceerd in hoofdstuk 1. De experimentele technieken waarmee de scintillerende materialen werden onderzocht worden beschreven in hoofdstuk 2. In Tabel I worden een aantal scintillatie eigenschappen gegeven van de materialen die bestudeerd zijn.

Het eerste onderwerp, het vinden van nieuwe, anorganische scintillatoren voor gamma detectie, wordt behandeld in de hoofdstukken 3 en 4. In hoofdstuk 3 worden een aantal medische stralingstoepassingen en de meest gebruikte scintillatoren besproken. Vervolgens worden de primaire eisen genoemd waaraan de scintillatoren ten minste zouden moeten voldoen om in aanmerking te komen voor gebruik in de medische stralingstoepassingen. De eigenschappen van een aantal anorganische scintillatoren worden gepresenteerd. Tenslotte wordt de keuze voor de bestudeerde materialen gemotiveerd.

In hoofdstuk 4 worden twee nieuwe anorganische scintillatoren, $\text{LaCl}_3:\text{Ce}^{3+}$ en $\text{LaBr}_3:\text{Ce}^{3+}$, gepresenteerd. Optische en gammaexcitatie leidt tot Ce^{3+} luminescentie met emissie maxima bij 330 en 352 nm in het chloride, en emissie maxima bij 356 en 387 nm in het bromide. Beide materialen combineren een hoge lichtopbrengst met excellente energie resolutie en een snelle luminescentie. De licht opbrengst is respectievelijk 49000 ± 1000 en 61000 ± 5000 fotonen/MeV voor $\text{LaCl}_3:10\% \text{Ce}^{3+}$ en $\text{LaBr}_3:0.5\% \text{Ce}^{3+}$. In het chloride, wordt 40% geëmitteerd met een vervaltijd van 26 ns, terwijl meer dan 90% geëmitteerd wordt met een vervaltijd van 35 ns in het bromide. Energie resoluties van ongeveer 3% (volle breedte op het half maximum van de piek positie) werden waargenomen voor de 662 keV fotopiek. Duidelijk moge zijn dat $\text{LaCl}_3:\text{Ce}^{3+}$ en $\text{LaBr}_3:\text{Ce}^{3+}$ twee eerste keus scintillatoren zijn die gebruikt kunnen worden voor toepassingen waarbij een excellente energie resolutie gewenst is in combinatie met een snelle scintillatie.

Table I. Scintillatie-eigenschappen van de bestudeerde materialen.

Materiaal	Z_{eff}	ρ (g/cm ³)	[Ce ³⁺] (%)	λ (nm)	Licht Opbrengst (10 ³ f/MeV)	Energieresolutie R (%, @ 662 keV)	Vervalconstante τ (ns)
LaCl ₃	49.5	3.86	0.57	330	40 ± 4	7.0 ± 0.5	20 (8%)
			2		49 ± 1	3.5 ± 0.1	27 (10%)
			4		49 ± 1	3.5 ± 0.1	25 (18%)
			10		49 ± 1	3.3 ± 0.1	25 (41%)
			30		43 ± 1	3.3 ± 0.1	25 (69%)
CeCl ₃	50	3.9	-	335	46 ± 4	4.5 ± 0.5	25 (69%)
LaBr ₃	46.9	5.29	0.5	358	61 ± 5	2.8 ± 0.2	31
			2		48 ± 5	3.8 ± 0.4	31
			4		48 ± 5	3.5 ± 0.4	31
			10		45 ± 5	3.9 ± 0.4	31
Cs ₂ LiYCl ₆		3.31	0.5	376	18 ± 2	7 ± 1	390 + slow
Cs ₂ LiYBr ₆		4.15	1.0	388	25 ± 3	6 ± 1	72 + slow
LuCl ₃	63.1	4.00	0.45	374	6.6 ± 0.6	18.0 ± 0.5	110 (87%)
			2		6.4 ± 0.6	13.8 ± 0.5	85 (73%)
			4		5.4 ± 0.5	11.4 ± 0.4	76 (91%)
			10		6.4 ± 0.6	11.7 ± 0.4	88 (81%)
LuBr ₃	62.6	5.17	0.021	408	29 ± 3	8.6 ± 0.5	~10 ³
			0.46		18 ± 2	7.8 ± 0.3	32 (10%)
			0.76		26 ± 3	6.5 ± 0.5	32 (15%)
			2.5		19 ± 2	6.2 ± 0.2	20 (31%)
			8		16 ± 1	6.0 ± 0.1	19 (33%)
K ₂ LaCl ₅	44.1	2.9	0.7	344	21 ± 3	-	~10 ³
			10		30 ± 5	5.1 ± 0.5	~10 ³
K ₂ LaBr ₅	42.8	3.9	0.7	359	26 ± 3	7.5 ± 0.8	~10 ³
			10		40 ± 4	4.9 ± 0.5	~10 ²
K ₂ LaI ₅	52.4	4.4	0.7	401	52 ± 5	5.0 ± 0.5	24
			10		57 ± 6	4.2 ± 0.4	24

Het tweede deel van het proefschrift is volledig gewijd aan het onderzoek van het scintillatiemechanisme in verschillende materialen. Het scintillatie proces, de vorming van elektronen en gaten na absorptie van straling, en energie overdracht worden geïntroduceerd en besproken in hoofdstuk 5. Het scintillatiemechanisme in LaCl₃:Ce³⁺ en LaBr₃:Ce³⁺ is onderwerp van hoofdstuk 6. Echter, een zeer gedetailleerd onderzoek werd alleen voor het chloride uitgevoerd. In beide materialen spelen zogenaamde “self-trapped excitons” (STEs) een belangrijke rol. In LaCl₃:Ce³⁺, is *STE diffusie* het meest belangrijke scintillatie mechanisme. Het kan zowel de waargenomen anti-correlatie tussen Ce³⁺ en STE luminescentie verklaren als de aanwezigheid van STEs in het EPR spectrum van LaCl₃:Ce³⁺ en de afwezigheid van “V_K” centra. In het geval van LaBr₃:Ce³⁺ werd verondersteld dat ofwel de “V_K” centra onmiddellijk met een elektron recombineren en een STE vormen, zodat snelle STE diffusie het dominante scintillatie mechanisme zou zijn, ofwel dat Ce³⁺ direct een vrij elektron invangt van de geleidingsband en een gat invangt van de valentieband. Dit zal ook tot snelle Ce³⁺ luminescentie leiden.

In hoofdstuk 7 wordt de invloed van het anion op de scintillatie-eigenschappen van de elapsoliten, Cs₂LiYX₆:Ce³⁺ (X = Cl, Br, I), besproken. Het is een model

systeem dat wijdverbreid onderzocht wordt met behulp van optische, scintillatie en magnetische studies. Het voordeel ten opzichte van andere materialen ligt hierin dat het driewaardige metaal ion gesitueerd is in het centrum van een regelmatig octaëder, omringt door zes halide ionen X waardoor eenvoudigweg andere driewaardige ionen, waaronder Ce^{3+} , in het rooster ingebracht kunnen worden. Ook zijn deze materialen van speciaal belang door het mogelijk aanwezig zijn van zogenaamde “core-valence” (CV) luminescentie. Van de onderzochte materialen blijkt alleen Cs_2LiYCl_6 dit verschijnsel te vertonen. Dit vanwege de positie van de valentieband ten opzichte van de 5p “core” band van Cs. De Ce^{3+} gedoteerde elpasoliten geven intense Ce^{3+} luminescentie naast wat zwakke STE emissie als zij blootgesteld worden aan röntgenstraling. De lichtopbrengst als functie van de temperatuur kan het best beschreven worden als een belvormige curve welke sterk op de curve voor de productie van “ F ” centra lijkt. Zowel in het chloride als in het bromide is “*binary electron-hole diffusion*” het dominante scintillatiemechanisme. Het blijkt dat het anion weinig tot geen invloed heeft op het type scintillatiemechanisme. Echter, de levensduur van het STE is korter in het bromide dan in het chloride.

In hoofdstuk 8 worden de eigenschappen van en het scintillatiemechanisme in $LuCl_3:Ce^{3+}$ en $LuBr_3:Ce^{3+}$ besproken. Ook nu weer is “*binary electron-hole diffusion*” het dominante scintillatie mechanisme. Echter, bij zeer lage temperaturen is “ V_K ” diffusie waarschijnlijk belangrijker. Voor zowel $LuCl_3:Ce^{3+}$ als $LuBr_3:Ce^{3+}$ is er bijzonder veel ruimte in het rooster voor de “off-centre” relaxatie van de “ V_K core” van het STE. Hierdoor is de lichtopbrengst van het chloride zeer laag. Als de Ce concentratie verhoogt wordt blijkt dat de licht opbrengst in het bromide minder wordt.

Hoofdstuk 9 behandelt de invloed van het anion op de scintillatie en spectroscopie van puur en Ce^{3+} -gedoteerd K_2LaX_5 ($X = Cl, Br, I$). De eigenschappen worden vergeleken met die van LaX_3 en KX . In dit systeem, blijft de kristalstructuur vrijwel ongewijzigd als de chemische omgeving van het driewaardige metaalion veranderd wordt door X te variëren als $X = Cl, Br, I$. De “bandgap,” de energie van de excitonpiek en de golflengte van de STE emissie zijn vrijwel gelijk voor K_2LaX_5 en LaX_3 , maar verschillen ten opzichte van KX . The chemische eigenschappen van de anionen hebben een grote invloed op de scintillatie en spectroscopie van K_2LaX_5 . In de volgorde Cl, Br, I, neemt de “centroid shift” van de 5d configuratie van Ce^{3+} toe vanwege de grotere co-valentie tussen het anion en Ce^{3+} en de grotere polariseerbaarheid van het anion zelf. In K_2LaX_5 , maar vooral in $K_2LaCl_5:0.2-0.5\% Ce^{3+}$, spelen de STEs een grote rol. Ook nu weer wordt er een anti-correlatie waargenomen tussen de Ce^{3+} en STE emissie. In de reeks Cl, Br, I, neemt de intensiteit van de Ce^{3+} emissie toe terwijl de intensiteit van de STE emissie afneemt. Ook neemt de efficiëntie en scintillatie vervalsnelheid toe in de reeks Cl, Br, I. Dit is gerelateerd aan (a) de toename van de beweeglijkheid van het STE en (b) de toename van de kans dat Ce^{3+} direct de vrije elektronen en gaten invangt.

Dankwoord/Acknowledgments

Zoals in de meeste gevallen kan men een werk van grote omvang – zoals een dissertatie wel genoemd mag worden – niet alleen tot stand brengen. Velen hebben dan ook op de een of andere manier hun steentje bijgedragen aan dit proefschrift. En u raad het al, ik kan ze helaas niet allemaal noemen. Toch wil ik de belangrijkste spelers kort bedanken.

Allereerst gaat mijn waardering en erkentelijkheid uit naar mijn dagelijks begeleider en co-promotor, Pieter Dorenbos. Pieter had immer een luisterend oor voor de ideeën en proefballonnetjes van mijn zijde. Met hem heb ik de meeste discussies gevoerd over scintillatie en luminescentie en ben hierdoor vaak tot nieuwe inzichten gekomen. Door zijn kritische houding ben ik zelf wat nauwkeuriger naar de dingen gaan kijken en werd veel van mijn werk zonder al te veel problemen geaccepteerd voor publicatie.

Carel van Eijk, mijn promotor, was diegene die wat meer nadruk legde op de praktische kant van de zaak. Door zijn toedoen zal veel van wat onderzocht werd ook daadwerkelijk toepassing vinden. Zijn enthousiasme werkt zeker aanstekelijk en ik heb mede daardoor met plezier aan het onderwerp scintillatie gewerkt. De consequentie was wel dat ik graag de laatste resultaten per direct aan hem wilde mededelen. Gelukkig kon dit vrijwel altijd, mede door de gemakkelijke communicatie.

Ook Johan de Haas wil ik bedanken voor zijn hulp bij het oplossen van technische problemen. Inmiddels weet ook ik dat als een opstelling het niet doet, dat nog niet betekent dat de opstelling stuk is.

In closing, I am grateful to Dr. Wondwosen Mengesha for the time and effort he spend on measuring the electron response of $\text{LaCl}_3:\text{Ce}^{3+}$ and his patience to teach me the in-and-outs of the Compton Coincidence Technique, and MCNP. Also, I would like to thank Dr. Karl Krämer and Prof. H.U. Güdel for the growth of the high quality crystals. Without their work this thesis could not have existed.

Curriculum Vitae

EDGAR VAN LOEF, the author of this Ph.D. thesis, was born on March 11th 1973 in Tiel, the Netherlands. He finished high school (VWO) at the Stichtse Vrije School, Zeist, in June 1993. In September he started studying Chemistry at Utrecht University. He performed his graduation research at the Condensed Matter group under the supervision of Prof. A. Meijerink.

There he characterised the VUV (4f) energy levels of Ho^{3+} and Er^{3+} in several fluoride hosts, using different spectroscopic techniques. Additionally, a new quantum cutter was proposed based on Er^{3+} and Tb^{3+} . He graduated in May 1998. In January 1999 he started his Ph.D. research at the Radiation Technology Group of the Interfaculty reactor Institute (IRI) of Delft University of Technology. The results of that research are written down in this thesis.

EDGAR VAN LOEF, de auteur van dit proefschrift, is geboren op 11 maart 1973 te Tiel. In juni 1993 behaalde hij zijn VWO examen bij de Stichtse Vrije School te Zeist. In september ging hij Scheikunde studeren aan de Universiteit Utrecht. Een jaar later, in augustus 1994, behaalde hij zijn Propaedeuse diploma. Het afstudeeronderzoek naar de (4f) VUV niveaus van Ho^{3+} en Er^{3+} in verschillende fluoride gastroosters werd verricht bij de vakgroep Gecondenseerde Materie onder supervisie van Prof. A. Meijerink. In Mei 1998 studeerde hij af en werd doctorandus in de Fysische Chemie. In januari van het jaar daaropvolgend begon hij als promovendus in de groep Stralings Technologie van het Interfacultair Reactor Instituut van de Technische Universiteit Delft. De resultaten van zijn onderzoek zijn in dit proefschrift beschreven.

List of publications

Journals

E.V.D. van Loef, P. Dorenbos, C.W.E. van Eijk, K. Krämer, H.U. Güdel, “*High-energy-resolution Scintillator: Ce³⁺ activated LaCl₃*,” Appl. Phys. Lett. 77 (2000) 1467.

E.V.D. van Loef, P. Dorenbos, C.W.E. van Eijk, K.W. Krämer, H.U. Güdel, “*Optical and Scintillation Properties of pure and Ce³⁺ doped GdBr₃*,” Opt. Com. 189 (2001) 297.

E.V.D. van Loef, P. Dorenbos, C.W.E. van Eijk, K. Krämer, H.U. Güdel, “*High-energy resolution Scintillator: Ce³⁺ activated LaBr₃*,” Appl. Phys. Lett. 79 (2001) 1573.

E.V.D. van Loef, P. Dorenbos, C.W.E. van Eijk, K. Krämer, H.U. Güdel, “*Scintillation properties of LaCl₃:Ce³⁺ crystals: Fast, Efficient and High-energy-resolution Scintillators*,” IEEE Trans. Nucl. Sci. 48 (2001) 341.

E.V.D. van Loef, P. Dorenbos, C.W.E. van Eijk, K.W. Krämer, H.U. Güdel, “*Scintillation properties of LaBr₃:Ce³⁺ crystals: fast, efficient and high-energy-resolution scintillators*,” Nucl. Instr. Meth. Phys. Res. A 486 (2002) 254.

E.V.D. van Loef, P. Dorenbos, C.W.E. van Eijk, K.W. Krämer, H.U. Güdel, “*Scintillation and spectroscopy of the pure and Ce³⁺-doped elpasolites: Cs₂LiYX₆ (X = Cl, Br)*,” J. Phys. Condens. Mat. 14 (2002) 8481.

E.V.D. van Loef, P. Dorenbos, C.W.E. van Eijk, K.W. Krämer, H.U. Güdel, “*Properties and mechanism of scintillation in LuCl₃:Ce³⁺ and LuBr₃:Ce³⁺ crystals*,” Nucl. Instr. Meth. Phys. Res. A 496 (2003) 138.

E.V.D. van Loef, W. Mengesha, J.D. Valentine, P. Dorenbos, C.W.E. van Eijk, “*Non-proportionality and Energy Resolution of a LaCl₃:Ce³⁺ Scintillation Crystal*,” IEEE Trans. Nucl. Sci. 50 (2003) 155.

E.V.D. van Loef, P. Dorenbos, C.W.E. van Eijk, “*The scintillation mechanism in LaCl₃:Ce³⁺*,” J. Phys.: Condens. Mat. 15 (2003) 1367.

E.V.D. van Loef, P. Dorenbos, C.W.E. van Eijk, “*Influence of the anion on the spectroscopy and scintillation mechanism of pure and Ce³⁺ doped K₂LaX₅ and LaX₃ (X = Cl, Br, I)*,” Phys Rev. B., accepted.

Patents

P. Dorenbos, C.W.E. van Eijk, H.U. Güdel, K.W. Krämer, E.V.D. van Loef, “*Ceriumhoudend anoganisch scintillatormateriaal*,” Dutch Patent Application NL1014401, publication date 11 January 2001.

P. Dorenbos, C.W.E. van Eijk, H.U. Güdel, K.W. Krämer, E.V.D. van Loef, “*Scintillator crystals, method for making same, use thereof*,” International Patent Application WO 01/60944, publication date August 23 2001.

P. Dorenbos, C.W.E. van Eijk, H.U. Güdel, K.W. Krämer, E.V.D. van Loef, “*Scintillator crystals, method for making same, use thereof*,” International Patent Application WO 01/60945, publication date August 23 2001.

Other publications to which was contributed

P. Dorenbos, C.W.E. van Eijk, E. van Loef, M. Globus, B. Grinyov, M. Ratner, V. Tarasov, Yu. Zorenko, “*Heavy Oxide Scintillators: Bulk Crystals and Thin Films for Radiation Monitoring of Environment and Biological Objects*,” SCINT99 Conference Proceedings, Moscow, August 1999, p. 577.

D. Pauwels, N. Lemasson, B. Viana, A. Kahn-Harari, E.V.D. van Loef, P. Dorenbos, C.W.E. van Eijk, “*Scintillation Properties of $\text{Lu}_2\text{Si}_2\text{O}_7:\text{Ce}^{3+}$ (LPS) Crystals*,” SCINT99 Conference Proceedings, Moscow, August 1999, p. 511.

Yu. Zorenko, V. Gorbenko, I. Konstankevych, M. Pashkovsky, M. Globus, B. Grinyov, V. Tarasov, P. Dorenbos, C.W.E. van Eijk, Edgar van Loef, “*Scintillators on the base of single crystalline films of $\text{Al}_2\text{O}_3 - \text{Y}_2\text{O}_3$ system oxides*,” SCINT99 Conference Proceedings, Moscow, August 1999, p. 476.

O. Guillot-Noël, E.V.D. van Loef, P. Dorenbos, C.W.E. van Eijk, K.W. Krämer, H.U. Güdel, “*Luminescence and scintillation properties in Ce^{3+} activated trihalide compounds*,” SCINT99 Conference Proceedings, Moscow, August 1999, p. 282.

K.D. Oskam, R.T. Wegh, H. Donker, E.V.D. van Loef, A. Meijerink, “*Downconversion: a new route to visible quantum cutting*,” J. Alloy Comp. 300 (2000) 421.

R.T. Wegh, H. Donker, E.V.D. van Loef, K.D. Oskam, A. Meijerink, “*Quantum cutting through downconversion in rare-earth compounds*,” J. Lumin. 87-89 (2000) 1017.

R.T. Wegh, E.V.D. van Loef, A. Meijerink, “*Visible quantum cutting via downconversion in $\text{LiGdF}_4:\text{Er}^{3+}$, Tb^{3+} upon Er^{3+} $4f(11) \rightarrow 4f(10)5d$ excitation*,” J. Lumin. 90 (2000) 111.

D. Pauwels, N. Le Masson, B. Viana, A. Kahn-Harari, E.V.D. van Loef, P. Dorenbos, C.W.E. van Eijk, “*A novel inorganic scintillator: Lu₂Si₂O₇:Ce³⁺ (LPS)*,” IEEE Trans. Nucl. Sci 47 (2000) 1787.

C.W.E. van Eijk, P. Dorenbos, E.V.D van Loef, “*Energy resolution of some new inorganic-scintillator gamma-ray detectors*,” Rad. Meas. 33 (2001) 521.

C.P. Allier, E.V.D. van Loef, P. Dorenbos, R. W. Hollander, C.W.E. van Eijk, K.W. Krämer, H.U. Güdel, “*Readout of a LaCl₃(Ce³⁺) Scintillation Crystal with a Large Area Avalanche Photodiode*,” Nucl. Instr. Meth. Phys. Res. A 485 (2002) 547.

D. Wisniewski, S. Tavernier, A.J. Wojtowicz, M. Wisniewska, P. Bruyndonckx, P. Dorenbos, E. van Loef, C.W.E. van Eijk, L.A. Boatner, “*LuPO₄:Nd and YPO₄:Nd, new promising VUV scintillation materials*,” Nucl. Instr. Meth. Phys. Res. A 486 (2002) 239.

U. Rogulis, S. Schweizer, J.-M. Spaeth, E. V. D. van Loef, P. Dorenbos, C. W. E. van Eijk, K. Krämer, H. U. Güdel, “*Magnetic resonance investigations of LaCl₃:Ce³⁺ scintillators*,” Rad. Eff. Def. Sol. 157 (2002) 951.

P. Dorenbos, E.V.D. van Loef, C. W. E. van Eijk, K. Krämer, H. U. Güdel, “*Anomalous 10 ns emission in Ce³⁺ doped Cs₃LuCl₆*,” Phys. Rev. B., submitted.